Microcavity-enhanced light-matter interaction in van der Waals heterostructures

Stefan Schwarz

A thesis submitted for the degree of
Doctor of Philosophy

Sheffield, *October 2015*

This work is dedicated to my son David.

Abstract

The recently emerging layered two-dimensional materials provide a new material class for novel opto-electronic devices. These materials have a unique crystal structure with strong intra-layer bonding and weak van der Waals inter-layer bonding. This allows to thin down the crystal to single atomic layer thickness using an adhesive tape. With the discovery of this method to produce stable monolayer sheets of graphene and the observation of its remarkable properties, a new research area started to develop. Besides graphene there is a whole class of two-dimensional materials with similar crystal structure. One of the most prominent are transition-metal dichalcogenides, molybdenum and tungsten selenide and sulphide. They are semiconducting materials that experience an indirect-to-direct bandgap transition when the material is thinned down to monolayer thickness. This change of the bandstructure leads to a remarkable increase in the emission efficiency of those materials in monolayer form. Strong spin-orbit coupling, inversion symmetry breaking, large exciton binding energy and large oscillator strength means that this class of materials are very promising for future room temperature opto-electronic devices. In this work monolayer sheets of transition-metal dichalcogenides, as well as vertically stacked heterostructure of two-dimensional materials, are coupled to microcavity structures in order to study light-matter interaction of these materials. A tunable open-acces microcavity structure has been developed to have full control of the light-matter interaction. In this system monolayer sheets of molybdenum disulphide have been studied, where the weak coupling regime with a Purcell enhancement of a factor of 10 has been observed. Monolayer sheets of molybdenum diselenide have been investigated where the first conclusive demonstration of strong exciton-photon coupling is demonstrated. Finally, a light emitting diode, produced by a heterostructure consisting of graphene, boron nitride and tungsten diselenide has been embedded in a microcavity structure where a significant change in the emission pattern of photo- and electroluminescence has been demonstrated.

List of Publications

Journal Publications

D. Sercombe, **S. Schwarz**, O. Del Pozo-Zamudio, F. Liu, B. J. Robinson, E. A. Chekhovich, I. I. Tartakovskii, O. Kolosov, A. I. Tartakovskii, *"Optical investigation of the natural electron doping in thin MoS2 films deposited on dielectric substrates"*, Scientific Reports **3**, 3489 (2013)

S. Schwarz, S. Dufferwiel, P. M. Walker, F. Withers, A. A. P. Trichet, M. Sich, F. Li, E. A. Chekhovich, D. N. Borisenko, N. N. Kolesnikov, K. S. Novoselov, M. S. Skolnick, J. M Smith, D. N. Krizhanovskii, A. I. Tartakovskii, *"Two-dimensional metal-chalcogenide films in tunable optical microcavities"*, Nano Lett. **14**(12), 7003 (2014)

O. Del Pozo-Zamudio, **S. Schwarz**, M. Sich, I. A. Akimov, M. Bayer, R. C. Schofield, E. A. Chekhovich, B. J. Robinson, N. D. Kay, O. V. Kolosov, A. I. Dmitriev, G. V. Lashkarev, D. N. Borisenko, N. N. Kolesnikov, A. I. Tartakovskii, *"Photoluminescence of two-dimensional GaTe and GaSe films"*, 2D Mat. **2**, 035010 (2015)

S. Dufferwiel, **S. Schwarz**, F. Withers, A. A. P. Trichet, F. Li, M. Sich, O. Del Pozo-Zamudio, C. Clark, A. Nalitov, D. D. Solnyshkov, G. Malpuech, K. S. Novoselov, J. M. Smith, M. S. Skolnick, D. N. Krizhanovskii, A. I. Tartakovskii, *"Exciton-polaritons in van der Waals heterostructures embedded in tunable microcavities"*, Nature Comm. **6**, 8579 (2015)

O. Del Pozo-Zamudio, **S. Schwarz**, J. Klein, R. C. Schofield, E. A. Chekhovich, O. Ceylan, E. Margapoti, A. I. Dmitriev, G. V. Lashkarev, D. N. Borisenko, N. N. Kolesnikov, J. J. Finley, A. I. Tartakovskii, *"Photoluminescence and Raman investigation of stability of InSe and GaSe thin films"*, *submitted to Appl. Phys. Lett.*, arXiv:1506.05619 (2015)

S. Schwarz, S. Dufferwiel, F. Withers, A. A. P. Trichet, F. Li, C. Clark, K. S. Novoselov, J. M. Smith, M. S. Skolnick, D. N. Krizhanovskii, A. I. Tartakovskii, *"Strong exciton-photon coupling in monolayer heterostructures in tunable microcavities"*, Conference proceeding in CLEO: 2015, OSA Technical Digest (online) (Optical Society of America, 2015), paper STh3M.8. (2015)

F. Withers, O. Del Pozo-Zamudio, **S. Schwarz**, S. Dufferwiel, P. M. Walker, T. Godde, A. P. Rooney, A. Gholinia, K. Watanabe, T. Taniguchi, S. J. Haigh, A. K. Geim, V. I. Falko, A. I. Tartakovskii, K. S. Novoselov, *"WSe2 light-emitting tunneling transistors with enhanced brightness at room temperature"*, Nano Lett. **15**(12), 8223 (2015)

S. Schwarz, O. Del Pozo-Zamudio, F. Withers, P. M. Walker, T. Godde, R. C. Schofield, A. P. Rooney, A. Gholinia, K. Watanabe, T. Taniguchi, C. Clark, S. J. Haigh, K. S. Novoselov, and A. I. Tartakovskii, *"Atomically Thin WSe_2 Electroluminescence Devices Embedded in Monolithic Microcavities"*, *in preparation*

S. Schwarz, S. Dufferwiel, F. Withers, K. Watanabe, T. Taniguchi, C. Clark, K. S. Novoselov, and A. I. Tartakovskii, *"Experimental determination of the inter-valley exchange energy through valley Zeemann splitting"*, *in preparation*

Conference Contributions

S. Schwarz, D. Sercombe, O. Del Pozo-Zamudio, F. Liu, B. J. Robinson, E. A. Chekhovich, O. Kolosov, A. I. Tartakovskii, *"Optical properties of MoS2 and other chalcogenides"*, Poster presentation, Winter School on *"Few Spin Solid State Nano-Systems"* (2013)

S. Schwarz, O. Del Pozo-Zamudio, D. Sercombe, B. J. Robinson, S. Poltavtsev, I. A. Akimov, D. N. Borisenko, N. N. Kolesnikov, E. A. Chekhovich, M. Bayer, O. Kolosov, A. I. Tartakovskii, *"Photoluminescence of Gallium Selenide thing layers"*, Poster presentation, Graphene Week (2013)

S. Schwarz, O. Del Pozo-Zamudio, B. J. Robinson, M. Sich, J. K. Chana, D. N. Borisenko, N. N. Kolesnikov, E. A. Chekhovich, O. Kolosov, D. N. Krizhanovskii, A. I. Tartakovskii, *"Photoluminescence of Gallium Selenide thing layers"*, Poster presentation, Conference on Electronic Properties of Two-Dimesional Systems (2013)

S. Schwarz, S. Dufferwiel, F. Withers, A. A. P. Trichet, J. M. Smith, D. N. Borisenko, N. N. Kolesnikov, E. A. Chekhovich, M. S. Skolnick, D. N. Krizhanovskii, A. I. Tartakovskii, *"Optics of two-dimensional semiconducting films in tunable photonic microcavities"*, Poster presentation, International Winterschool on Electronic Properties of Novel Materials (2014)

S. Schwarz, S. Dufferwiel, F. Withers, A. A. P. Trichet, M. Sich, J. M. Smith, D. N. Borisenko, N. N. Kolesnikov, E. A. Chekhovich, M. S. Skolnick, D. N. Krizhanovskii, A. I. Tartakovskii, *"Optics of two-dimensional semiconducting films in tunable photonic microcavities"*, Oral presentation, UK Semiconductors (2014)

S. Schwarz, S. Dufferwiel, F. Withers, M. Sich, A. A. P. Trichet, J. M. Smith, P. M. Walker, F. Li, E. A. Chekhovich, D. N. Borisenko, N. N. Kolesnikov, K. S. Novoselov, M. S. Skolnick, D. N. Krizhanovskii, A. I. Tartakovskii, *"Optics of two-dimensional metal-chalcogenides in tunable photonic microcavities"*, Poster presentation, Graphene Week (2014)

S. Schwarz, S. Dufferwiel, F. Withers, A. A. P. Trichet, J. M. Smith, D. N. Borisenko, N. N. Kolesnikov, E. A. Chekhovich, M. S. Skolnick, D. N. Krizhanovskii, A. I. Tartakovskii, *"Optics of two-dimensional semiconducting films in tunable photonic microcavities"*, Oral presentation, International Conference on the Physics of Semiconductors (2014)

S. Schwarz, S. Dufferwiel, P. M. Walker, F. Withers, A. A. P. Trichet, M. Sich, F. Li, E. A. Chekhovich, D. N. Borisenko, N. N. Kolesnikov, K. S. Novoselov, M. S. Skolnick, J. M Smith, D. N. Krizhanovskii, A. I. Tartakovskii, *"Two-dimensional metal-chalcogenide films in microcavity structures"*, Invited Junior Speaker, Symposium on 2D Materials for Optoelectronics, Plasmonics and Photonics (2014)

S. Schwarz, S. Dufferwiel, P. M. Walker, F. Withers, A. A. P. Trichet, M. Sich, F. Li, E. A. Chekhovich, D. N. Borisenko, N. N. Kolesnikov, K. S. Novoselov, M. S. Skolnick, J. M Smith, D. N. Krizhanovskii, A. I. Tartakovskii, *"Two-dimensional metal-chalcogenide films in tunable optical microcavities"*, Oral Presentation, NPL Graphene & 2D Materials Conference (2014)

S. Schwarz, S. Dufferwiel, F. Withers, A. A. P. Trichet, F. Li, M. Sich, O. Del Pozo-Zamudio, C. Clark, K. S. Novoselov, J. M. Smith, G. Malpuech, M. S. Skolnick, D. N. Krizhanovskii, A. I. Tartakovskii, *"Strong exciton-photon coupling in van der Waals heterostructures"*, Poster presentation, International Winterschool on Electronic Properties of Novel Materials (2015)

S. Schwarz, S. Dufferwiel, F. Withers, A. A. P. Trichet, F. Li, C. Clark, K. S. Novoselov, J. M. Smith, M. S. Skolnick, D. N. Krizhanovskii, A. I. Tartakovskii, *"Strong exciton-photon coupling in monolayer heterostructures in tunable microcavities"*, Oral presentation, Conference on Lasers and Electro-Optics (2015)

S. Schwarz, S. Dufferwiel, F. Withers, A. A. P. Trichet, F. Li, M. Sich, O. Del Pozo-Zamudio, C. Clark, K. S. Novoselov, J. M. Smith, M. S. Skolnick, D. N. Krizhanovskii, A. I. Tartakovskii, *"Strong exciton-photon coupling in van der Waals heterostructures"*, Oral presentation, UK Semiconductors (2015)

S. Schwarz, S. Dufferwiel, F. Withers, A. A. P. Trichet, F. Li, M. Sich, O. Del Pozo-Zamudio, C. Clark, K. S. Novoselov, J. M. Smith, M. S. Skolnick, D. N. Krizhanovskii, A. I. Tartakovskii, *"Strong exciton-photon coupling in van der Waals heterostructures"*, Oral presentation, Graphene Week (2015)

Acknowledgements

I want to thank my supervisor, Sasha Tartakovskii, not only for giving me the opportunity to receive my scholarship within the FP7 ITN S3NANO, which allowed me to work towards my PhD degree as part of the LDSD group in Sheffield, but also for his valuable guidance and support throughout the last three years. I also would like to thank Maurice Skolnick, who is an excellent leader of the group and supported me with valuable advice and feedback of my work. I had the pleasure to work in an excellent group which helped me to achieve my goals during my PhD, for which I am very thankful. I want to thank Evgeny Chekhovich for teaching me in my first months of my PhD, Max Sich for his advice and help to perform time-resolved measurements and Paul Walker for assisting me with numerical simulations, supporting my experimental results. In particular I want to thank Scott Dufferwiel with whom I spent hours and hours in the lab allowing me to achieve great results for my PhD, as well as the skill to understand Geordie-English. I am thankful to my (former and current) colleagues in the 2D Materials group, Danny Sercombe, Osvaldo Del Pozo-Zamudio, Robbie Schofield, Sasha Skrypka and Tillmann Godde for their support. Especially Danny and Osvaldo have been great friends to me who helped me from my very first day in the group.

I also want to thank Mark Fox for his advice as post-graduate tutor, Dima Krizhanovskii for his advice and input in the polariton work and Feng Li for many fruitful discussions about instabilities and drift of the open cavity setup; the staff of the EPSRC National Centre for III-V Technologies, in particular Ken Kennedy, Saurabh Kumar and Jon Milner; people from the AFM group teaching me how to use the AFM, Jake, Ross, Nic and Rebecca; the staff responsible for cryogenics, Chris Vickers, Pete Robinson and Phil Mydewer; and the workshop staff who did excellent work producing parts for our open cavity setup, Paul Kemp-Russell and Simon Dixon. I want to show my gratitude to my colleagues and friends that I was privileged to meet during my time in Sheffield, within and outside the LDSD

group. You all helped making my time in Sheffield so much more enjoyable. Thank you all!

Within this PhD I had the opportunity to collaborate with several groups. I want to thank Freddie Withers from the group of Kostya Novoselov, University of Manchester, for producing the best possible samples which was a massive help for achieving the results in this work. I want to thank Ben Robinson and Oleg Kolosov, University of Lancaster, for sharing their expertise in AFM and UFM measurements; Ilya Akimov from group of Manfred Bayer, TU Dortmund, for hosting me for a week to do time-resolved measurements; Guillaume Malpuech for his theory support in the polariton work; and especially I want to thank Jon Finley for allowing me to work in his group for two months, together with Emanuela Margapoti, Julian Klein and Oezlem Ceylan on Raman measurements.

I want to thank the European Union for providing me with the funding for my PhD within the FP7 ITN S3NANO and thanks to Sasha and Sally for organizing this network consisting of world leading groups in academia and industry. Thanks to all the fellows in this network who I got to know and become friends with in these three years, Andreas Waeber, Benjamin Pingault, Per-Lennart Ardelt, Marko Rancic, David-Domink Jarausch, Anastasia Varlet, Timo Kaldewey, Viktoriia Kornich, Stefan Bogdanovic, Jakob Kammhuber, Maja Cassidy, Christian Hepp, Chris Lawson, Elena Kammann and Aymeric Del Teil.

Finally I want to thank my parents for their endless support, my mother Monika, with Helli; my father Rainer, with Andrea; my brother Markus, my sister Carina; my grandparents, especially my late grandfather Raimund who was an inspiration to me; and my parents-in-law Otto and Sonja. Thanks to my sisters-in-law Simone and Higgi, with Martin and my nieces and nephews, Johanna, Patrick and Anna.

Special thanks go to my wife, Maria, who supports me and I can say without a doubt that without her I would not be where I am now.

Contents

1 Introduction

Van der Waals crystals are layered materials that have gained significant attention in recent years. The crystals of those materials have a layered structure with strong intra-layer bonding and weak inter-layer bonding stemming from van der Waals forces. The most famous material that falls into this group is graphite where the layered structure is well known and widely used. A schematic of the crystal structure of graphite is shown in Figure 1.1 where the layered nature of the crystal is highlighted. The interest in van der Waals crystals sparked in mid 2000s when the research group in Manchester developed a technique to isolate a stable, single atomic layer of graphite, called graphene, and managed to place this single layer of carbon atoms on a target substrate [1]. This relatively recent development was the beginning of a new research area on layered two-dimensional (2D) materials with thicknesses down to a single atomic layer [2]. Although the physical properties of graphene were already predicted in 1947, it took more than 50 years before the isolation of a single graphene layer was successful [3]. This development attracted a lot of attention, especially after the demonstration of room temperature quantum Hall effect only a few months after the first graphene layer was isolated [4, 5]. These achievements were awarded with the Nobel prize in physics in 2010 for the two leading researchers. One of the most striking properties is the band structure of graphene. It displays a Dirac cone with zero bandgap [6]. This allows ballistic transport with high charge carrier mobility of up to 10^5 $\text{cm}^2\text{V}^{-1}\text{s}^{-1}$ enabling a new approach for future electronic devices [7]. This is around two orders of magnitude higher than in conventional electronic devices produced by current technologies [8]. The downside of graphene, however, is that due to the lack of an optical bandgap the On/Off-ratio of such electronic devices is too low for practical technological implementations [9].

Not only the unique properties of graphene caused this research area to boom, but also the simplicity of the technique [10]. Due to the layered structure of the crystals it is

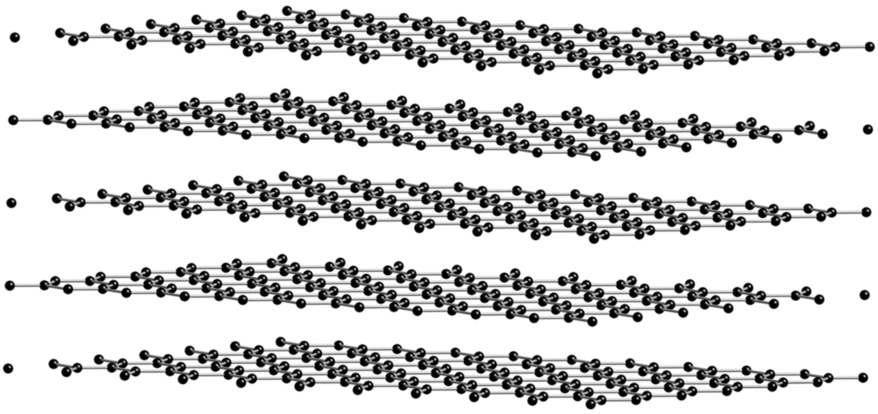

Figure 1.1: Crystal structure of graphite. The crystal structure highlights the layered nature of graphite. Weak van der Waals forces result into weak inter-layer bonding which allows to peel off layer by layer in order to produce a single atomic layer called graphene.

possible to peel off some layers of this material with an adhesive tape. By applying another adhesive tape this layer can be thinned down to few layers. Eventually the tape can be applied onto a substrate where the layered material will stick due to van der Waals forces. A more detailed description of this fabrication technique is given in chapter 4 where also different methods to transfer these monolayer sheets on arbitrary substrates are introduced.

1.1 Two-dimensional materials

The same technique can be adapted for various van der Waals crystals to obtain thin films down to single atomic layers. In fact, there is a huge selection of materials that can be thinned down to monolayer sheets. Table 1.2 displays a list of van der Waals crystals with a wide range of properties [11]. Apart from graphene, which has already been discussed briefly, another widely used layered material is hexagonal boron nitride (hBN) [12–14]. This is a semiconducting material with a wide bandgap of around 6 eV. Boron nitride is often used as substrate for other two-dimensional materials due to its high quality and stability [15]. It is used especially in combination with graphene where it serves as ideal substrate for defect free tunnelling barriers, for example [16, 17]. Due to their similar crystal lattice constant Moiré patterns are observed in heterostructures consisting of hBN and graphene if the crystal axes are aligned to each other [18, 19]. Recently hBN has also been

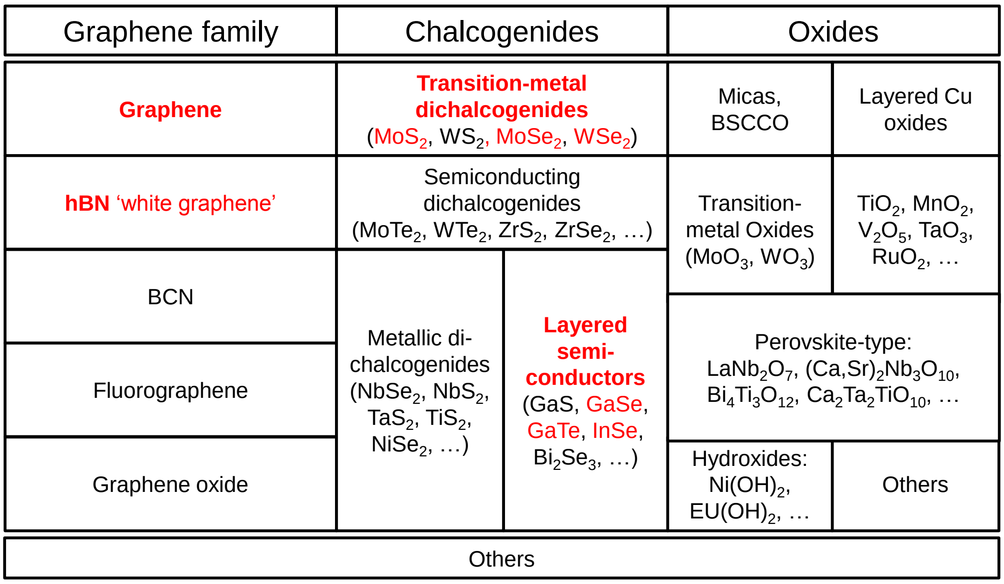

<table>
<tr><th>Graphene family</th><th colspan="2">Chalcogenides</th><th colspan="2">Oxides</th></tr>
<tr><td>Graphene</td><td colspan="2">Transition-metal dichalcogenides
(MoS_2, WS_2, $MoSe_2$, WSe_2)</td><td>Micas, BSCCO</td><td>Layered Cu oxides</td></tr>
<tr><td>hBN ‘white graphene’</td><td colspan="2">Semiconducting dichalcogenides
($MoTe_2$, WTe_2, ZrS_2, $ZrSe_2$, …)</td><td>Transition-metal Oxides
(MoO_3, WO_3)</td><td>TiO_2, MnO_2, V_2O_5, TaO_3, RuO_2, …</td></tr>
<tr><td>BCN</td><td rowspan="3">Metallic dichalcogenides
($NbSe_2$, NbS_2, TaS_2, TiS_2, $NiSe_2$, …)</td><td rowspan="3">Layered semiconductors
(GaS, GaSe, GaTe, InSe, Bi_2Se_3, …)</td><td colspan="2" rowspan="2">Perovskite-type:
$LaNb_2O_7$, $(Ca,Sr)_2Nb_3O_{10}$, $Bi_4Ti_3O_{12}$, $Ca_2Ta_2TiO_{10}$, …</td></tr>
<tr><td>Fluorographene</td></tr>
<tr><td>Graphene oxide</td><td>Hydroxides:
$Ni(OH)_2$, $EU(OH)_2$, …</td><td>Others</td></tr>
<tr><td colspan="5">Others</td></tr>
</table>

Figure 1.2: Overview of the large selection of materials with a layered crystal structure. Physical properties allow to group different materials. In this work graphene and hBN as well as a selection of 2D chalcogenides are discussed. The table is taken and altered from [11].

used as spacing layer to form multiple quantum well structures of another class of materials, called transition-metal dichalcogenides, which are discussed in the following [55]. Some layered materials are found to be unstable in ambient conditions, where oxidation and degradation of a monolayer sheet can occur within seconds after being exposed to air [20]. A way to overcome this problem is to perform the mechanical exfoliation in a oxygen and water-free atmosphere where hBN is used to encapsulate the material in order to protect it from the environment [21, 22].

Transition-metal dichalcogenides (TMDCs) are semiconducting materials with an optical bandgap in the visible light range. Because of the layered crystal structure TMDCs have been used as lubricants for many years in the past but had no real use in opto-electronics [23]. This changed drastically when TMDCs were thinned down to monolayer sheets and unexpected alterations of their physical properties were observed. The remarkable feature of these materials is an indirect-to-direct bandgap transition as the material is thinned down towards a single monolayer [24]. Due to the direct bandgap a monolayer sheet has an emission efficiency several orders of magnitude higher than few-layer sheets or bulk. This has been demonstrated for the first time with molybdenum disulphide (MoS_2) [25] and has been observed for molybdenum diselenide ($MoSe_2$) [26], tungsten disulphide (WS_2)

[27] and tungsten diselenide (WSe_2) [28] consequently. The carrier mobility observed in TMDCs is several thousand $cm^2V^{-1}s^{-1}$, which is comparable to the values achieved in conventional electronic devices. With the presence of an optical bandgap, the On/Off-ratio, exceeding a value of 10^8, is significantly improved compared to graphene devices [29, 30]. Properties such as large spin-orbit coupling [31], inversion symmetry breaking [32], large exciton binding energy [33–35] and large oscillator strength mean that this class of materials are very promising for future room temperature opto-electronic devices and therefore TMDCs with be the main focus of this work [36–39]. In general out-perform selenides their sulfide counter-parts in terms of emission efficiency, emission linewidth and material stability. Although a larger oscillator strength has been predicted for sulfides, novel effects are easier observed in selenides due to the relative narrow linewidth. Recently, in addition to pronounced excitonic features in TDMCs, quantum dot-like features have been observed in WSe_2 [40–43], demonstrating single photon emission.

Other semiconducting layered crystals, such as gallium and indium chalcogenides or black phosphorous [48], have a similar crystal structure to TMDCs but exhibit different optical properties as they are already direct bandgap semiconductors in bulk leading to a typical optical response when reducing the layer thickness. Examples of this material class are indium selenide (InSe) [44], gallium selenide (GaSe) [45], gallium telluride (GaTe) [46], gallium sulphide (GaS) [47]. While gallium chalcogenides have a significant lower coupling strength, GaSe and GaTe found its applications as non-linear crystals and have been used for second harmonic generation experiments and stimulated emission has been demonstrated in the past [49, 50]. The emission wavelength of these materials covers a wide range from 550 nm to 1.3 μm. Additionally the change of the band structure as a function of the sheet thickness allows control of the emission wavelength throughout this range. This offers a reliable light source from the visible to telecommunication wavelengths. Finally, other classes of layered materials listed in the table are superconducting chalcogenides such as niobium selenide, where recently the presence of charge density waves are demonstrated [51], or topological insulator such as bismuth telluride, for example [52].

The isolation of single and few-layer sheets of these layered materials shows promising properties for different opto-electronic applications and allows the investigation of novel physical effects that may be unachievable with other material systems. The fabrication of mono- and few-layer sheets allows the use of a wide range of substrates including substrates suitable for flexible opto-electronic devices [53]. New functionality can be achieved by stacking individual thin films on top of each other to create heterostructures combining the unique, individual properties of each layer. Such heterostructures have been produced to form multiple quantum wells using hBN and TMDCs [54]. Furthermore, electrically pumped devices have been realized with vertically stacked heterostructures, where large emission efficiencies have been demonstrated [55].

1.2 Incorporation of two-dimensional materials in photonic structures

In order to control and enhance the light-matter interaction of TMDCs, monolayer sheets are coupled to microcavity structures. A microcavity is an optical resonator that confines the optical emission of an active material placed inside this resonator. In general this modifies the photonic density of states (DoS) which leads to significant alteration of the spectral and temporal emission pattern of the active material. This allows the study of novel physics and leads to various applications depending on the coupling rate and the dissipation rates of the cavity and emitter. Historically, microcavities have been used in many systems, such as conventional III-V semiconductors for example. The emission efficiency of gallium arsenide based quantum dots, for example, has been increased by several orders of magnitude by embedding the dots in microcavity structures [56].

In the so-called strong coupling regime a new quasi-particle called exciton-polariton is formed [57]. This offers a potential new approach for opto-electronic applications. For example, the coherence of Bose-Einstein condensates in polariton systems can be exploited to realize ultra-low threshold lasing devices [58–61]. Other novel properties observed in polariton systems are the propagation of soliton wave packets [62], superfluid-like behavior [63] or exciton-polariton spin switches [64].

Coupling layered materials to photonic structures has been demonstrated recently, where for example, a significant enhancement of the detected photocurrent is observed in a photodetector based on graphene, embedded in microcavity structures [65]. Emission efficiency of TMDCs has been enhanced with photonic crystal cavities, where also photonic lasing devices have been realized [66, 67]. Photonic lasing has also been observed in micropillar cavities based on whispering gallery modes [68, 69]. The claim of strong exciton-photon coupling of MoS_2 in planar microcavities has been made showing the great potential for the observation of the strong coupling regime [70]. Here, the first unambiguous demonstration of the strong coupling regime in TDMCs is demonstrated in chapter 6.

This work consists of a theoretical description of optical properties of TMDCs and microcavity systems in general, where the difference of the so-called weak and strong coupling is explained in chapter 2 and 3. Experimental methods are described in chapter 4 where the fabrication method to produce monolayer sheets and the optical setups used in this work are explained. The last part of chapter 4 describes the properties and features of the developed tunable open-access microcavity system. Light-matter interaction is studied in a tunable microcavity system where the weak coupling regime with an increase of the emission efficiency in TMDCs and GaSe is demonstrated in chapter 5. Chapter 6 shows the first conclusive strong exciton-photon coupling of TMDCs using the tunable microcavity system where exciton polariton states are introduced and potential approaches towards room temperature polariton systems are discussed. Finally, chapter 7 shows the first demonstration of light emitting tunneling transistors, formed by vertically stacked heterostructures, embedded in microcavity structures.

MoS_2 samples and van der Waals heterostructure samples used in this work were provided by F. Withers, University of Manchester, the concave shape substrates for the top DBRs in the tunable open access microcavity have been milled by A. Trichet, University of Oxford and the DBRs were acquired commercially. GaSe samples were fabricated by myself. FDTD simulations were performed together with P. Walker. The measurements, data analysis and the preparation of the paper has been done by myself under guidance of S. Dufferwiel.

2 Optical properties of chalcogenide thin films

In semiconductor materials, such as transition-metal dichalcogenides or gallium chalcogenides, the absorption of photons via interband transitions lead to electron-hole pairs. The electron in the conduction band and the hole in the valence band are bound to each other via Coulomb interaction, forming an *exciton*. In III-V semiconductors excitons are in general free excitons, called Wannier-Mott excitons.

2.1 Optics in semiconductors

Wannier-Mott excitons are delocalized states with a Bohr radius larger than the lattice constant and are, therefore, not bound to specific atoms. In order to form excitons the attractive potential is required to be large enough so that collisions with phonons do not destroy the exciton. In other words, the exciton binding energy E_B has to be larger than the energy of thermally excited phonons k_BT with the Boltzmann's constant $k_B \approx 1.38 \times 10^{-23}$ $\mathrm{J \cdot K^{-1}}$ and temperature T:

$$E_B > k_BT. \tag{2.1}$$

For Wannier-Mott excitons the effective mass approximation is used to describe the exciton. The binding energy of the exciton in an environment with a dielectric constant ε_r is given by:

$$E(n) = -\frac{\mu}{m_0}\frac{1}{\varepsilon_r^2}\frac{R_H}{n^2} = -\frac{R_X}{n^2}, \tag{2.2}$$

where n is the principle quantum number, R_H is the Rydberg energy, $m = m_e^* + m_h^*$ is the exciton mass and μ is the reduced mass with $\frac{1}{\mu} = \frac{1}{m_e^*} + \frac{1}{m_h^*}$ in which $m_{e,h}^*$ is the effective mass of electron and hole respectively. To simplify this expression, the exciton Rydberg energy R_X is used to describe the binding energy. The separation of the electron and the hole r_n is given by the Bohr model:

$$r_n = \frac{m_0}{\mu}\varepsilon_r n^2 a_H = n^2 a_X. \tag{2.3}$$

Here, $a_H \approx 5.292^{-11}$m is the Bohr radius of the hydrogen atom and $a_X = \left(\frac{m_0\varepsilon_r}{\mu}\right) a_H$ the exciton Bohr radius. The energy of an exciton at a direct bandgap transition at $k = 0$, where k is the wave vector, is the energy of the bandgap E_g minus the energy from the Coulomb interaction:

$$E_X = E_g - \frac{R_X}{n^2} \tag{2.4}$$

2.1.1 Photoluminescence

Photoluminescence (PL) is a photon emission process due to recombination of an optically created electron-hole pair. The incident photon is absorbed when its energy is larger than the optical bandgap of the material. Through scattering processes, much faster than the interband recombination time, the electron decays to the minimum of the conduction band. Figure 2.1 shows a schematic of a (a) direct bandgap and (b) indirect bandgap. Due to negligible momentum of photons, a radiative recombination is only possible for $\Delta k \approx 0$, hence only in direct bandgap materials. In case of an indirect bandgap, non-radiative recombination occurs via phonons. Radiative recombination is only possible in multiple particle transitions, where the phonon contributes to the change in k. These processes are far less efficient so that the emission efficiency of an indirect bandgap material is significantly reduced.

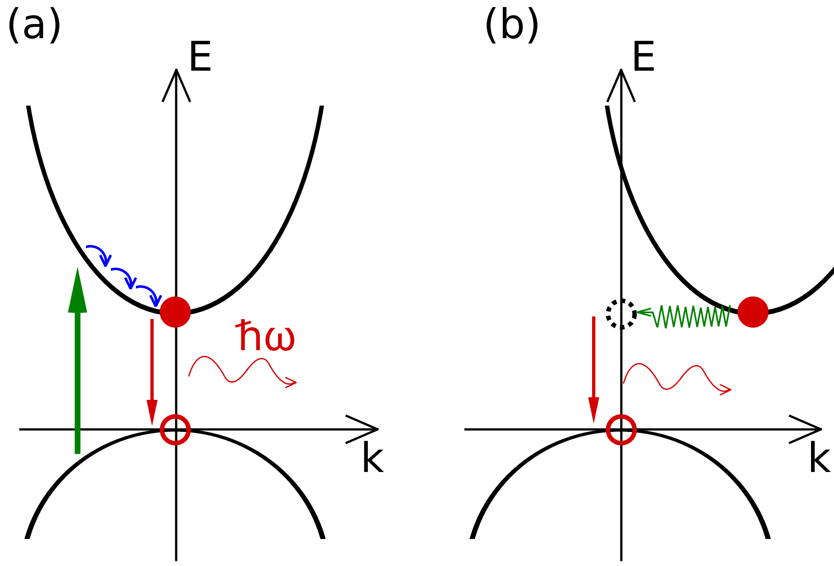

Figure 2.1: Schematic of a semiconductor bandstructure. The bandstructure is showing (a) a direct bandgap and (b) an indirect bandgap. A radiative recombination can only occur in a direct transition ($k \approx 0$). In case of the indirect bandgap a phonon can serve as the source of the momentum required for the transition.

Electrons in atoms sit in discrete energy levels leading to discrete emission spectra where the linewidth is limited by the uncertainty principle $\Delta E \Delta t > \hbar/2$. In semiconductors, however, the electrons and holes form a thermal distribution before recombination from the conduction band to the valence bad. The homogeneous linewidth of the emission depends the thermal distribution $k_B T$ as well as the density of states and carrier density. Structural disorder in the material leads to a disordered bandstructure. Radiative recombination of electron-hole pairs have slightly different energies resulting in an inhomogeneous broadening in the observed PL spectrum. In 2D materials this inhomogeneous broadening is the dominating factor and, therefore, the radiative lifetime is not linked to the observed linewidth via the uncertainty principle as given above.

2.1.2 Electroluminescence

In electroluminescence devices the emission is caused by electric carrier injection. In order to allow an electron to recombine, it requires a hole in the conduction band obeying Pauli blockade. Two different approaches are used for electroluminescence devices. The first approach relies on the principle of a *p*-*n* or *p*-*i*-*n* diode, shown in Figure 2.2, where a

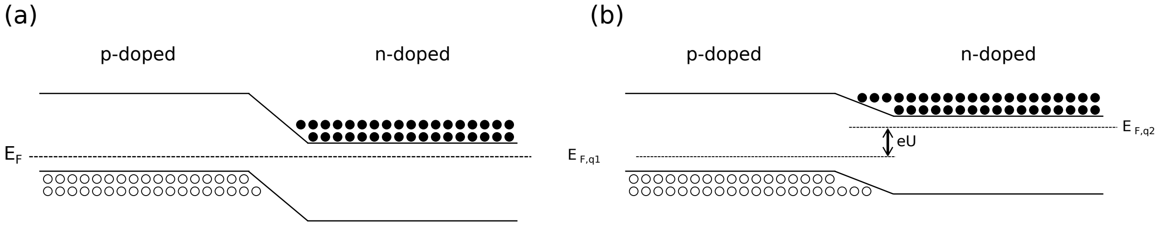

Figure 2.2: Band diagram of a *p*-*n* diode. The *p*-*n* transition shows the excess of electrons in the n-doped area and excess of holes in the p-doped area at (a) no applied voltage and (b) forward bias. When applying a voltage, the Fermi level shifts and a depletion region forms where electrons can recombine to holes. This carrier injection is the fundamental principle of a LED device.

depletion region is formed at the interface of a *p*-doped and *n*-doped semiconductor. Applying a voltage injects electrons from the *n*-doped area into the *p*-doped area and holes the other way around. The spontaneous emission of these carriers is the basic principle of a light emitting diode (LED).

The second approach relies on carrier injection through tunneling barriers. When two conductors are separated by a thin insulator, carriers can tunnel through this barrier according to the tunnel effect. The probability for a tunneling event, T, is derived from the Schrödinger equation and reads:

$$T = \frac{16E\left(U_0 - E\right)}{U_0^2} \mathrm{e}^{-2\alpha L}, \tag{2.5}$$

where E is the energy of the carrier, U_0 is the height of the barrier, L is the thickness of the barrier and α is a constant given by:

$$\alpha = \sqrt{\frac{2m\left(U_0 - E\right)}{\hbar^2}}, \tag{2.6}$$

where m is the mass of the carrier. In 2D heterostructures hexagonal boron nitride (hBN) is often used as a substrate for other layered materials due to its high quality and cleanliness. For vertically stacked electroluminescence devices it is possible to use a few atomic layer thick hBN layers as tunnel barriers.

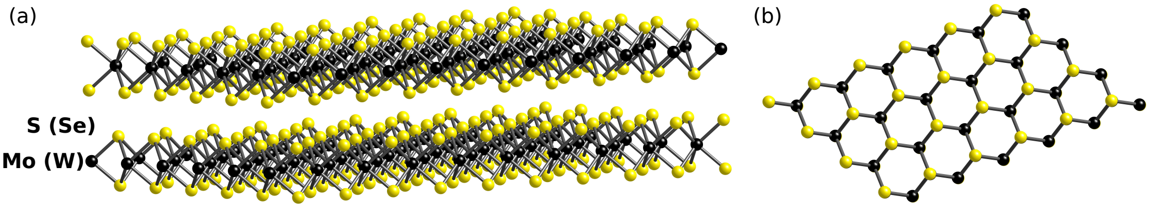

Figure 2.3: Crystal structure of transition-metal dichalcogenides. The transition-metal is located between two covalently bonded chalcogenides. (a) Subsequent layers are bonded via weak van der Waals forces. (b) The crystal structure forms a hexagonal crystal structure.

2.2 Transition-metal dichalcogenides

With respect to optical properties and opto-electronic applications TMDCs (in particular MoS_2, $MoSe_2$, WS_2 and WSe_2) appear to be the most promising out of all 2D materials that were studied so far [29] due to strong excitonic effects leading to simple spectral response. The crystal structure of TMDCs is shown in Figure 2.3 showing the layered nature of the material as well as the hexagonal crystal structure. Within one atomic layer the Mo (W) atoms are covalently bonded to S (Se) atoms where the transition-metal atom is located between the chalcogenide atoms. Each subsequent layer is bonded by electrostatic dipole forces known as Van der Waals forces. Due to its layered structure these materials have been used for various applications such as lubricants, catalysts or nanotubes, but only after the isolation of a single atomic layer and the resulting indirect-to-direct bandgap transition the way for TMDCs use in opto-electronics was opened.

2.2.1 Bandstructure of TMDCs

The calculated bandstructure of MoS_2 is shown in Figure 2.4 for (a) bulk, (b) quadrilayer, (c) bilayer and (d) monolayer sheets highlighting the transition from an indirect to a direct bandgap as the material is thinned down. It shows that MoS_2 in bulk has an indirect bandgap of 1.3 eV, located at the Γ-point in the valence band and halfway between the Γ- and K-point in the conduction band [25, 71, 72]. This fundamental bandgap increases for decreasing layers while the local minimum in the K-point is nearly independent to the thickness of the material and eventually results in a direct bandgap of 1.8 eV at the K-point for single layer sheets. This observation is a result of the quantum confinement effects.

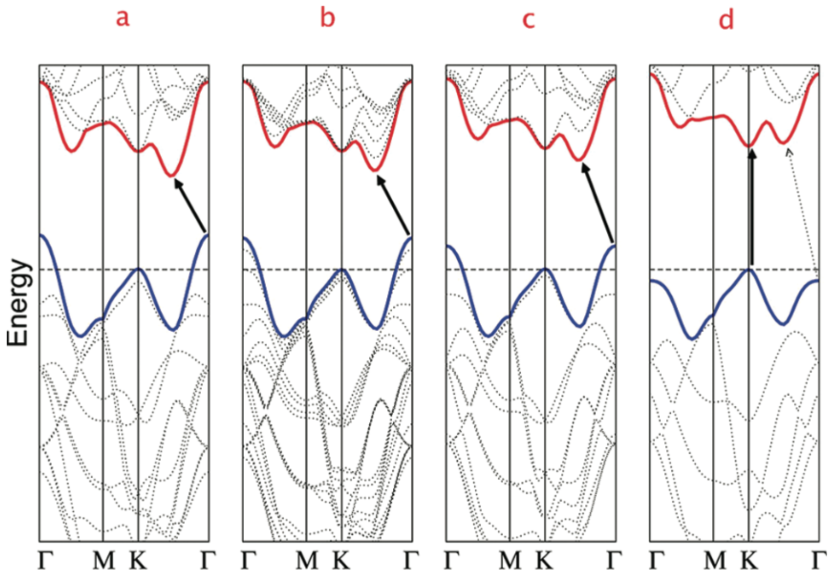

Figure 2.4: Calculated bandstructure of MoS_2. The bandstructure is calculated for (a) bulk, (b) quadrilayer, (c) bilayer and (d) monolayer sheets. The solid arrow indicates the fundamental bandgap transition and highlights the indirect-to-direct bandgap transition. Figure is taken from [25].

Density function theory (DFT) calculations show that the conduction band states at the K-point are given by localized d-orbitals on the Mo atoms and are quantitatively unaffected by interlayer coupling. The states near the Γ-point are given by combinations of the anti-bonding p_z-orbitals on the S atoms and the d-orbitals on the Mo atoms. Changing the number of layers results in a change of these states and a shift of the bandstructure in the Γ-point while change of the bandstructure at the K-point is negligible. This results in the transition to the direct bandgap at the K-point.

The change in the bandstructure in TDMCs leads to fundamental difference in their physical properties such as photoconductivity, absorption or most prominently the PL response. The PL quantum yield is increased by several orders of magnitude in monolayer sheets with respect to the bulk material [24]. The PL of monolayer sheets has been demonstrated for the first time for MoS_2 in 2010 where the significant increase of PL is shown as the material is thinned towards monolayer thickness. Furthermore, a monolayer sheet is a quasi-two-dimensional system. Due to the reduced dimension, dielectric screening is greatly reduced leading to an increase of the exciton binding energy. The exciton binding energy in monolayer sheets of TMDCs is several 100 meV, which is 10 times larger than in GaAs QWs [33].

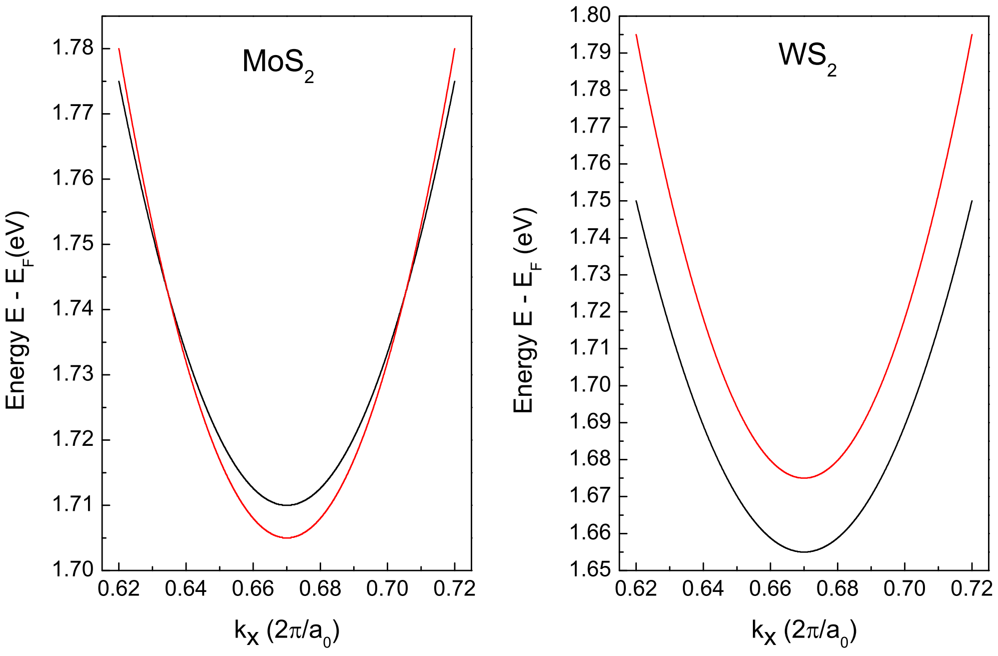

Figure 2.5: **Spin-split conduction band of MoS_2 and WS_2.** The conduction band is split into spin-up and spin-down, shown in the black and red line respectively, leading to bright and dark exciton transition where a fundamental difference between MoS_2 and WS_2 is observed. The same result is obtained for $MoSe_2$ and WSe_2 where, due to the larger spin splitting, the band crossing is farther away from the K point. Figure motivated from [31].

Large spin-orbit coupling in TMDCs results in a large valence band splitting in the K- and K'-points of the Brillouin zone, of approximately 160 meV in MoS_2 for example. This has been observed optically where two excitonic bands, called A and B band, are observed in absorption and in PL. In the minima of the conduction band spin-orbit interaction introduces a smaller splitting of a few tens of meV [31]. Due to the absence of a center of inversion and strong spin-orbit coupling the conduction band is split at the K-points, whereas at the high-symmetry points Γ and M the bands remain degenerate. Density functional theory (DFT) calculations show an interesting difference between tungsten and molybdenum dichalcogenides, labelled as MoX_2 and WX_2, respectively, in the following to indicate that the effect occurs for selenides and sulphides. In case of MoX_2 materials a band crossing between the spin-split conduction band is observed because the heavy band has a higher energy than the light band, as shown in Figure 2.5. This crossing is absent in WX_2 materials, which shows the difference in the optical properties of MoX_2 and WX_2 materials.

The difference of the spin-split conduction band is observed when an exciton is formed. In general an exciton is an electron-hole pair with parallel spin, referred to as *bright* exciton. In case of WX_2 materials, however, the transition from the conduction band minimum to the valence band occurs from an electron-hole pair with anti-parallel spin forming an optically inactive, so-called, *dark* exciton. This means that the lowest energy exciton band is dark and at cryogenic temperatures excitons accumulate in that band, leading to the predominantly formation of dark exciton in WSe_2. With increasing the temperature, bright exciton states are filled which optically recombine more efficiently and, therefore, lead to an increase of PL intensity [73].

2.2.2 Valley-polarization effects

A key parameter of a crystal lattice is its symmetry, which can be described with the magnetic moment $m(k)$ and the Berry curvature $\Omega(k)$ [74, 78]. The Berry curvature is used to describe the geometric properties of the wavefunctions in the parameter space [75, 76]. The symmetry distinguishes between time-reversal symmetry, which is fulfilled when $\Omega(k) = -\Omega(-k)$ and $m(k) = -m(-k)$ or space-inversion symmetry, for which $\Omega(k) = \Omega(-k)$ and $m(k) = m(-k)$. From this concludes that both symmetries are achieved at the same time for $\Omega(k) = 0$ and $m(k) = 0$ [77]. An example where time-reversal is observed is spin where spin-up is the time-reversal of spin-down. Inversion symmetry is given when the crystal lattice can be mirrored and remain unchanged, which is the case for graphene, for example. From the crystal structure of TMDCs, shown again in Figure 2.6(a) it is obvious that the spacial inversion symmetry is broken because the two sublattices are occupied by one transition-metal and two chalcogenide atoms. This crystal structure leads to a spin projection in the K- and K'-points which is, in combination with time-reversal symmetry, coupled to the valleys. Consequently, interband transitions at the two valleys are allowed for opposite helicity and are addressed optically with left circularly polarized (σ_-) and right circularly polarized (σ_+) excitation at K and K' valley, respectively as indicated in Figure 2.6(b).

Large polarization degrees of the PL emission of up to 100% at resonant and quasi-resonant excitation have been demonstrated following this principle for MoS_2 [37, 38] and WSe_2 [79, 80]. This opens the way for a novel concept of data storage and manipulation. While

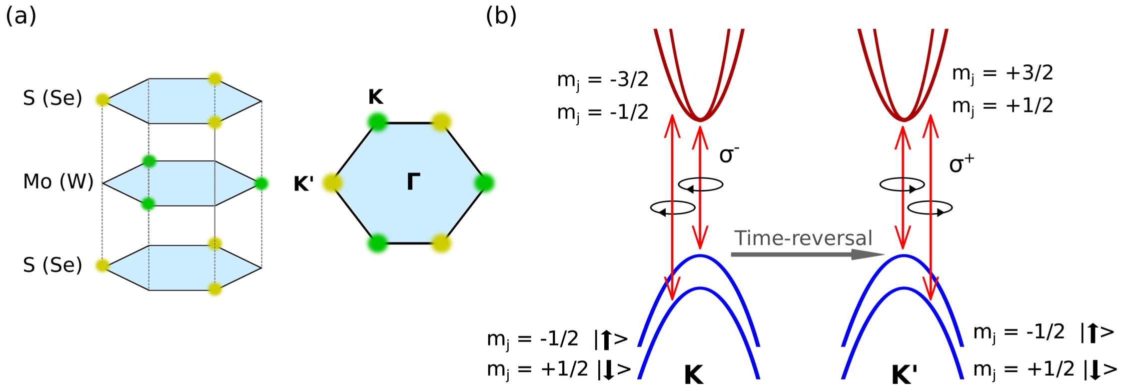

Figure 2.6: Valley-polarization in monolayer sheets of TMDCs. (a) The crystal structure of monolayer TMDCs show that the inversion symmetry is broken. (b) Interband transitions at the two valleys are allowed for opposite helicity, σ^+ and σ^-. Figure motivated from [38].

the electronic charge is used in electronic devices to carry a signal, or spins in spintronic devices, the valley index can be exploited in the so-called *valleytronics*. Interestingly, this polarization effect is not observed in $MoSe_2$ [81, 82]. To this point it is unclear whether this unexpected result stems from the fact that no polarization degree is injected or whether it is lost at a time-scale much faster than observable. Furthermore, this effect is only observed in monolayers because in bilayer TMDCs the inversion symmetry is restored and for every subsequent uneven number of layers the bandstructure already has changed into an indirect bandgap.

2.2.3 Defects in TMDC

In a real semiconductor there are invariably some defects in the crystalline structure. They are introduced due to thermodynamic considerations or impurities during the crystal growth, or in our case during the mechanical exfoliation of the TMDC. In monolayer TMDC those defects are either point defects or line defects in the crystal. A point defect is a highly localized defect, where either a vacancy or substitutional atom is built in the crystal lattice or atoms or impurities are placed between the crystal lattice. A line defect on the other hand involves a large number of atomic sited, connected by a line [83]. In general defects are divided in radiative and non-radiative defects. A quantum dot is a designed defect in the crystal lattice causing a local potential and a confinement in three dimensions [85]. The emission from these localized defects can be single photon emitters and used for quantum computation approaches, for example [86]. If these radiative defects are caused randomly, the defects will have slightly different energy levels and the individual emission emerges to a broad defect band in PL experiments. A doped semiconductor has impurities implanted intentionally. These impurities will result in states inside the optical bandgap which can be occupied and recombine radiatively or non-radiatively. Non-radiative processes are important in TMDCs because they result in a low quantum yield of the materials and short carrier lifetime. In non-radiative processes phonons are produced instead of photons. Chemical impurities or vacancies result in energy levels inside the bandgap and are localized to the space near the defect. Another process that is important is the Auger process which is a three-particle process where an electron and hole recombine and the excess energy is transferred to an additional electron or hole [87–89]. Finally, surface effects are very important in monolayer TMDC. It has been found that TMDCs are hydrophil materials which adsorb hydrogen atoms in the surface. This leads to a change in the exciton formation and generally results in inhomogeneous broadening.

2.2.4 Phonons in TMDC

When a crystal is formed, there is an interplay between attractive and repulsive interactions. Due to these opposite interactions there exists an energy minimum at which the atoms are placed. If the atoms move outside this energy minium, a restoring force pulls the atom back, leading to a vibration of the atoms in the crystal which is described by phonons. It can be shown that there are two branches of vibrations, called acoustic and optical phonons, which describe the vibrations where neighbouring atoms vibrate along the same direction or opposite direction, respectively. Acoustic phonons generally have zero frequency at vanishing k-vector, increasing linearly low k-vectors [83]. In monolayer TMDCs, however, a quadratic phonon mode is observed (ZA), which describes a out-of-plane vibration [84, 90]. It is found that the phonon energy for the out-of-plane vibrations shifts as the number of layers are decreased because the effect of the subsequent layers become less and less pronounced. The phonon dispersion, however, is remarkably similar for bulk and monolayers, apart from an observed splitting of the acoustic phonon modes around the Γ points in bulk. They are not observed in monolayers due to the reduced crystal symmetry [91].

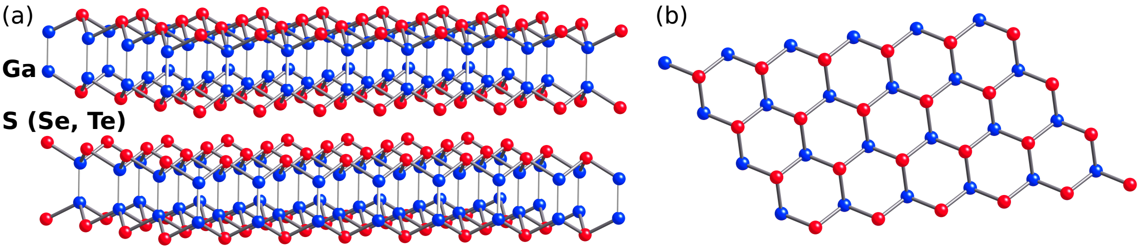

Figure 2.7: Crystal structure of gallium dichalcogenides. Two gallium atoms are covalently bonded to the chalcogenides forming a hexagonal crystal structure. Subsequent layers are bonded via weak van der Waals forces.

2.3 Gallium chalcogenides

The crystal structure of gallium chalcogenides such as gallium selenide (GaSe), for example, is shown in Figure 2.7. A monolayer consists of two covalently bonded gallium atoms sandwiched between covalently bonded chalcogenide atoms. It remains in its typical hexagonal crystal structure where each layer is weakly bonded via van der Waals forces [92]. Gallium chalcogenides, however, have fundamentally different optical properties than TMDCs. Calculations of the bandstructure of GaSe reveal a direct bandgap at the Γ-point where the valence band shows a saddle-like feature leading to an indirect interband transition very close to the bandgap [94]. In the following the discussion will be focused on GaSe [93], as this will be the material studied in chapter 5.

GaSe has been studied in bulk due to its non-linear properties where optically pumped stimulated emission has been observed [95]. Recently, GaSe and other gallium chalcogenides also received some attention where thin films were used to produce photonic devices [96]. One of the biggest drawbacks, however, is stability of GaSe in ambient conditions. It is found that thin films of GaSe degrade within several days when being exposed to air, where the first monolayer is possibly degraded within a few seconds after being produced by mechanical exfoliation. A way to overcome this issue is to perform the fabrication of thin films inside a glovebox system as demonstrated for several different layered materials [21]. In this thesis GaSe sheets of several tens of nanometers are studied, which show stability over a few days and do not degrade once placed in the cryostat for cryogenic measurements.

3 Fundamentals of light-matter interaction in microcavity structures

To enhance light-matter interaction an emitter is embedded in a photonic structure which confines light in at least one dimension. A common approach is using two mirrors that allow confinement of light in a formed cavity. This can be realized with simple metal mirrors or reflections at the boundary of a dielectric material. Alternatively periodic nanostructures such as distributed Bragg reflectors (DBR) or photonic crystals can be used. To achieve confinement in all three dimensions a combination of these approaches are used. Besides the planar and (hemi-)spherical cavities, which will be discussed in this chapter, other designs based on different geometries or physical effects have been studied. For example micro-pillar cavities are used to achieve very small cavity mode volumes. Whispering gallery mode cavities are used frequently, where recently even photonic lasing with two-dimensional materials has been demonstrated [67]. In this chapter the principles of microcavities are described followed by the differentiation of the weak and strong exciton-photon coupling between an emitter and a microcavity.

3.1 Characterization of microcavities

A schematic of a microcavity is shown in Figure 3.1 with the reflectivity of the mirrors, R, separated by length L. Resonant modes of the cavity are essentially solutions of the wave equation that fulfil the boundary conditions of the cavity. These cavity modes are described by the lineshape, mode spacing and other characteristics addressed to the specific mode. The longitudinal mode, for example, has an integer number of the half-wavelengths

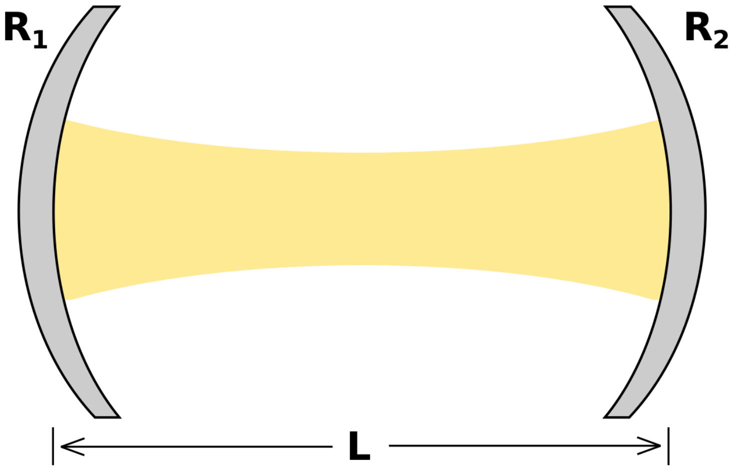

Figure 3.1: Schematic of a microcavity. The cavity consists of two mirrors with a reflectivity $R = R_1 + R_2$, separated by the cavity length L. This schematic is used to describe the parameters of a cavity.

that fit into the cavity. To characterize a microcavity several parameters and concepts are introduced.

3.1.1 Distributed Bragg reflectors

A DBR is an alternation of two materials with different refractive indices $n_{H,L}$. At the interface between the low index material (with $n = n_L$) and the high index material ($n = n_H$) the reflectivity is given by:

$$r = \frac{n_L - n_H}{n_L + n_H} = \frac{n_L/n_H - 1}{n_L/n_H + 1}. \tag{3.1}$$

By increasing the number of dielectric layers in alternating sequence the total reflection is increased significantly when the layer thicknesses are designed in a way that reflections between adjacent layers introduce a phase shift of $\Delta\phi = \pi$, leading to constructive interference of the reflections. The phase shift $\Delta\phi$ at the interface depends on the wave vector $k = 2\pi/\lambda$:

$$\Delta\phi = 2kd_{L,H}n_{L,H} = 2\frac{2\pi}{\lambda}d_{L,H}n_{L,H} \overset{!}{=} \pi. \tag{3.2}$$

This condition is fulfilled for thicknesses of $d_{L,H} = \frac{\lambda}{4n_{L,H}}$, where d_L and d_H are the thicknesses of the low and high refractive index material, respectively. With increasing number of pairs high reflectivity values are obtained over a certain wavelength band, called *stopband*. The total reflectivity of a DBR depends on the total number of pairs of the alternating layers N and is calculated as:

$$R = \left(\frac{1 - \frac{n_1}{n_2}\left(\frac{n_L}{n_H}\right)^{2N}}{1 + \frac{n_1}{n_2}\left(\frac{n_L}{n_H}\right)^{2N}} \right)^2, \tag{3.3}$$

with $n_{1,2}$ as the refractive indices of the surrounding media. The refractive index contrast $\Delta n = n_H - n_L$ of the low and high index material determines the spectral width of the stopband Δ_{sb}:

$$\Delta_{sb} = \frac{2\lambda_c \Delta n}{\pi n_{eff}}. \tag{3.4}$$

Here λ_c is the central wavelength of the stopband and $n_{eff} = 2\left(\frac{1}{n_L} + \frac{1}{n_H}\right)^{-1}$ the effective refractive index of the DBR.

3.1.2 Fabry-Perot microcavities

A Fabry-Perot cavity is based on the principle of a Fabry-Perot interferometer and consists of two parallel mirrors. An incident wave U_0 is first reflected by mirror 1 as shown in the schematic in Figure 3.2. Subsequently, the transmitted wave tU_0 is reflected by mirror 2, and so on. Assuming a coherent, monochromatic wave and two identical mirrors with a reflectivity coefficient of $r = |r|\,e^{i\Delta\phi}$ and a transmission coefficient of $t = 1 - r$. The phase shift caused by each reflection as well as the transmission between the

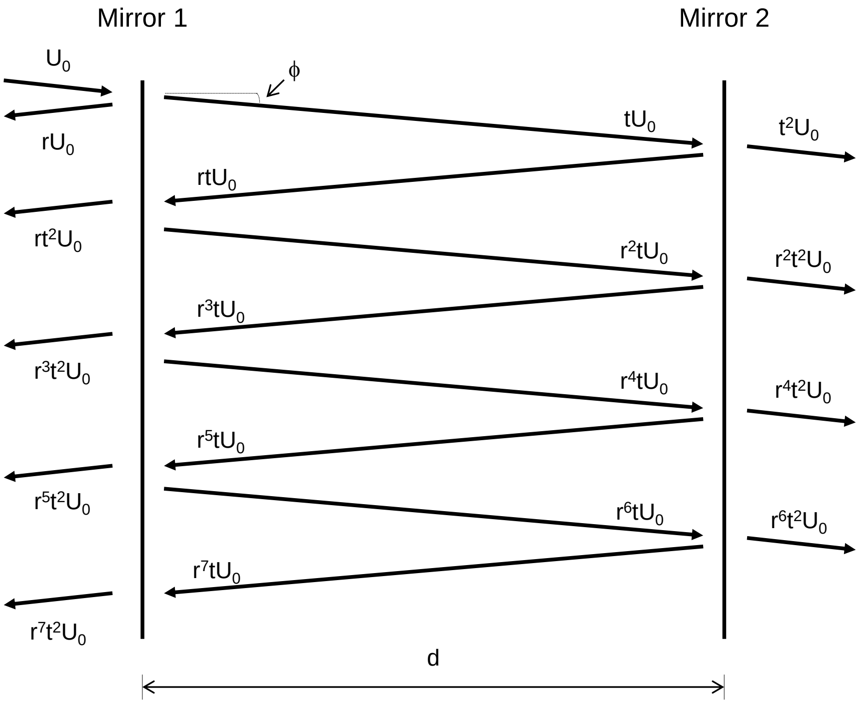

Figure 3.2: Principle of a Fabry-Perot interometer. The transmitted wave is a sum of each transmitted part, where the phase shift at each reflection and the phase shift caused by the propagation between the mirrors has to be taken into account.

mirrors, separated by the distance d, results in a total phase shift $\Delta\phi$ after each round-trip:

$$\Delta\phi = 2\Delta\phi_s - 2k_0 nd\cos(\phi) \tag{3.5}$$

The transmitted wave U_T is a sum of each transmitted part after each round-trip:

$$U_T = U_0 t^2 \left(1 + |r|^2 e^{i\Delta\phi} + |r|^4 e^{i2\Delta\phi} + ...\right). \tag{3.6}$$

Using the solution for the infinite geometric series:

$$\sum_{n=1}^{\infty} q^{n-1} = \frac{1}{1-q} \tag{3.7}$$

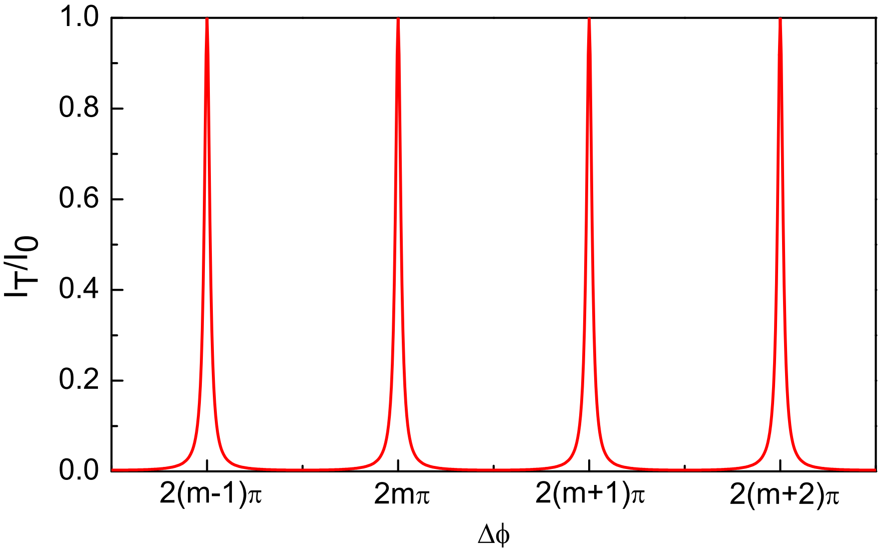

Figure 3.3: Transmission of a Fabry-Perot interferometer. The periodic transmission spectrum is shown for mirrors with 90% reflectivity each. The resonant condition is fulfilled when the total phase shift is $\Delta\phi = 2m\pi$.

with $q = |r|^2 e^{i\Delta\phi}$ the transmission is simplified to:

$$U_T = U_0 t^2 \frac{1}{1 - |r|^2 e^{i\Delta\phi}}. \tag{3.8}$$

The transmitted intensity I_T is calculated using $|r|^2 = R$ and $|t|^2 = T$ and normalized to the incident intensity $I_0 = |U_0|^2$:

$$\frac{I_T}{I_0} = \frac{T^2}{1 - R^2 e^{i\Delta\phi}} = \frac{T^2}{1 - 2R\cos(\Delta\phi) + R^2}. \tag{3.9}$$

The periodic transmission of a Fabry-Perot interferometer is shown in Figure 3.3. It shows that the transmission has a maximum when the total phase shift meets the condition $\Delta\phi = 2m\pi, m \in \mathbb{N}$.

3.1.3 Finesse and Q-factor

The *finesse* describes the ratio between wavelength spacing of two longitudinal modes $\Delta\lambda$, called free spectral range, and the linewidth of a cavity mode $\delta\lambda$:

$$F = \frac{\Delta\lambda}{\delta\lambda} = \frac{\pi\sqrt{R}}{1-R}. \tag{3.10}$$

A different way to express this is using the *Q-factor*, or quality-factor, of the cavity which is the ratio of the energy U stored within the cavity to the energy dissipated at each round-trip $\mathrm{d}U/\mathrm{d}t$ and can also be expressed as:

$$Q = \left|\lambda_c \frac{U}{\mathrm{d}U/\mathrm{d}t}\right|, \tag{3.11}$$

with λ_c as the wavelength of the cavity mode. The time dependence of the stored energy follows from solving equation 3.11:

$$U(t) = U_0 \mathrm{e}^{-\lambda_c t/Q} = U_0 \mathrm{e}^{-t/\tau}, \tag{3.12}$$

with U_0 the initial energy stored in the cavity, or rewritten for the electric field in the cavity, using $U(t) \propto |E(t)|^2$:

$$E(t) = E_0 \mathrm{e}^{-\lambda_c t/2Q} \mathrm{e}^{-\mathrm{i}\lambda_c t}, \tag{3.13}$$

with E_0 as the initial electric field in the cavity. The parameter $\tau = Q/\lambda_c$ in equation 3.12 and 3.13 is the average lifetime of a photon in the cavity. The Fourier transform of equation 3.12 leads to a Lorentzian distribution of the stored energy:

$$U(\lambda) = |E(\lambda)|^2 \propto \frac{1}{(\lambda-\lambda_c)^2 + (\lambda_c/2Q)^2}. \tag{3.14}$$

From equation 3.14 the full-width half-maximum (FWHM), or the linewidth, of the cavity mode is extracted as $\delta\lambda = \lambda_c/Q$, which allows to write the Q-factor as:

$$Q = \frac{\lambda_c}{\delta\lambda}. \tag{3.15}$$

Comparing equation 3.10 and 3.15 allows to compare the finesse and the Q-factor. While the finesse is a measure of how many round-trips the photon performs before exiting the cavity, the Q-factor is a measure of how long a photon is confined within the cavity before escaping. Since the mode spacing $\Delta\lambda$ is connected to the cavity length L with:

$$\Delta\lambda = \frac{2\pi c}{L}, \tag{3.16}$$

the finesse and the Q-factor are comparable for cavity lengths around the wavelength scale. For increasing cavity length, however, the Q-factor will increase because of the longer propagation time per round-trip.

3.2 Light-matter interaction

The general schematic of a microcavity in Figure 3.4 shows the main parameters that need to be considered to study light-matter interaction of an emitter in a cavity. These are the cavity-emitter coupling rate, g, decay rates of the cavity mode, κ, and the emitter, γ. In this system two fundamental regimes exist depending on the relative magnitude of these parameters. For the so-called weak coupling regime the dissipation rates exceed the coupling rate $(\kappa, \gamma >> g)$, where the Purcell effect is observed as discussed in section 3.2.1. For the other case, when the coupling rate is larger than the decay rates $(g >> \kappa, \gamma)$, the system is in the strong coupling regime. In this regime a photon emitted by the active material is re-absorbed and re-emitted many times before it escapes the cavity and the energy is transferred back and forth between emitter and cavity. This cyclic transfer is known as Rabi oscillation and leads to the formation of part-light, part-matter quasi-particles called

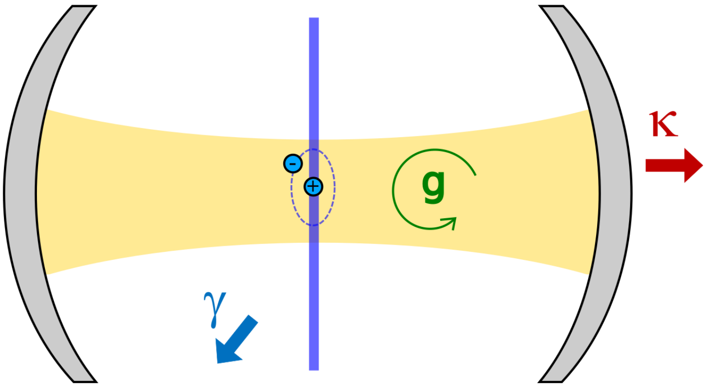

Figure 3.4: Schematic of a microcavity with an active material placed inside the structure. A quantum well-like active material is placed in the center of cavity, highlighted with the blue region. The three parameters used to describe the light-matter interaction of an emitter in a cavity are the emitter and cavity dissipation rates, γ and κ, and the cavity-emitter coupling rate, g.

polaritons. Exciton-polaritons and their physical properties are discussed in detail in 3.2.2. The cavity decay rate κ is defined as:

$$\kappa = \frac{1}{\tau_{cav}}, \tag{3.17}$$

where τ_{cav} is the photon lifetime. Assuming an ideal cavity $(R \approx 1)$ and an emitter that emits a short pulse containing N photons at time $t = 0$. After the time $t = nL_{cav}/c$ the pulse has travelled half a round-trip and is reflected by the mirror where $(1-R)N$ photons escape the cavity, leaving RN photons confined in the cavity. At each half round-trip $\Delta N = (1-R)N$ photons are lost, which allows to write a photon rate equation:

$$\frac{\mathrm{d}N}{\mathrm{d}t} = -\frac{\Delta N}{nL_{cav}/c} = -\frac{c(1-R)}{nL_{cav}}N. \tag{3.18}$$

Solving equation 3.18 results in $N = N_0 e^{-t/\tau_{cav}}$, where N_0 is the number of photons at $t = 0$, and with the photon lifetime τ_{cav}:

$$\tau_{cav} = \frac{nL_{cav}}{c(1-R)}. \tag{3.19}$$

Following from equation 3.17 and $\delta\omega = \frac{1}{\tau_{cav}} = \kappa$, the cavity decay is related to the Q-factor, $Q = \frac{\omega}{\delta\omega}$, of the cavity:

$$\kappa = \frac{\omega}{Q}. \tag{3.20}$$

The dissipation rate γ is influenced by several factors. It is enhanced when the emitter is not in resonance with the cavity mode or when the photon decays to other levels allowing transitions which are not in resonance with the cavity mode or through non-radiative decay. The emitter decay rate depends, therefore, on the internal dynamics of the active material and scattering processes that cause dephasing of the individual material. The cavity-emitter coupling rate is influenced by the interaction between the atom and the vacuum field in the cavity. The interaction energy ΔE between the emitter and the cavity field is determined by the electric dipole interaction:

$$\Delta E = \left|\mu_{if} E_{vac}\right|, \tag{3.21}$$

with $\mu_{if} = -e\langle i|x|f\rangle$ as the electric dipole matrix element of the transition between the initial state $|i\rangle$ and the final state $|f\rangle$, and E_{vac} the magnitude of the vacuum field. To calculate the coupling rate the energy of the Rabi oscillation is equal to the interaction energy, $\Delta E = \hbar g$, which leads to:

$$g = \left(\frac{\mu_{if}^2 \omega_c}{2\varepsilon_0 \hbar V_{eff}}\right)^{1/2}. \tag{3.22}$$

Here, ω_c is again the angular frequency and V_{eff} is the effective mode volume.

3.2.1 Weak coupling regime

The weak coupling regime addresses the change of the dynamics of the spontaneous emission of the cavity system in its excited state. Considering an active material, represented by a dipole, the spontaneous emission from an excited state depends on the vacuum field. By bringing the dipole in resonance with the cavity mode, the optical density of state can increase the radiative recombination rate, and therefore the spontaneous emission rate. However, if the dipole is out of spectral and spatial resonance, called photonic gap, the photon density of states is smaller than in vacuum resulting in a reduction of the spontaneous emission rate. The Purcell effect describes the local modification of the density of state.

Spontaneous emission rate

The spontaneous emission rate for an emitter with energy $\hbar\omega_e$ is given by Fermi's golden rule. In general the Fermi's golden rule states the probability of a transition from an initial state $|i\rangle$ to a final state $|f\rangle$, assuming that $|i\rangle$ and $|f\rangle$ are eigenstates of a Hamiltonian H_0 subject to a pertubation $H(t)$, and is given by:

$$\frac{1}{\tau} = \frac{2\pi}{\hbar^2} \left|\langle f \left| H' \right| i \rangle\right|^2 \rho_f, \tag{3.23}$$

with ρ_f as the density of final states and $H' = H_0 + H(t)$. Assuming an electric dipole $\mathbf{d}$ which is interacting with the light field $E(\mathbf{r},t)$ at point $\mathbf{r}$ and time t equation 3.23 can be rewritten as:

$$\frac{1}{\tau} = \frac{2\pi}{\hbar^2} |\mathbf{d} \cdot \mathbf{E}(\mathbf{r},t)|^2 \rho(\omega_e), \tag{3.24}$$

with $\rho(\omega_e)$ the photon density of states at energy $\hbar\omega_e$, which, in vacuum, is calculated by:

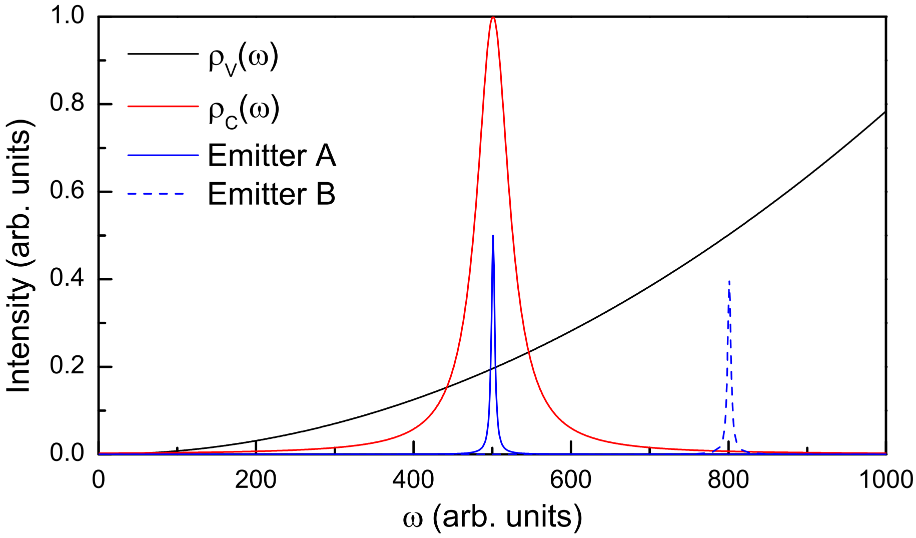

Figure 3.5: Density of states in vacuum and a cavity. The microcavity leads to a significant change in the density of states. When an emitter is placed in resonance (Emitter A), the spontaneous emission rate is enhanced but if the emitter is detuned to the cavity resonance, the spontaneous emission rate is suppressed (Emitter B) by the cavity.

$$\rho_V(\omega) = \frac{\omega^2 V n^3}{\pi^2 c^3}, \tag{3.25}$$

where V is the mode volume, ω is the angular frequency and n is the refractive index. Embedding the dipole in a microcavity structure, however, significantly alters the density of states. In a single-mode cavity with energy $\hbar\omega_c$ and a Q-factor Q the density of states is a Lorentzian function and writes as:

$$\rho_C(\omega_e) = \frac{2}{\pi} \frac{\delta\omega_c}{4(\omega-\omega_c)^2 + \delta\omega_c^2}. \tag{3.26}$$

Figure 3.5 shows a schematic of the different density of states, ρ_V and ρ_C. It can be seen that the microcavity allows an enhancement and inhibition of the spontaneous emission rate if the emitter is tuned (Emitter A) or detuned (Emitter B) to the resonance of the cavity mode, respectively. This is the so-called Purcell enhancement and is calculated as the ratio of the emission time of the emitter in the cavity Γ_C to the emission time of the emitter in vacuum Γ_V:

$$\frac{\Gamma_C}{\Gamma_V} = \frac{3Q\left(\lambda_c/n\right)^3}{4\pi^2 V_{eff}} \frac{\delta\omega_c^2}{4\left(\omega-\omega_c\right)^2+\delta\omega_c^2} \frac{|\mathbf{E}(\mathbf{r})|^2}{|\mathbf{E}_{max}|^2} \left(\frac{\mathbf{d}\cdot\mathbf{E}(\mathbf{r})}{\mathrm{d}E}\right)^2. \tag{3.27}$$

Equation 3.27 calculates the enhancement of the spontaneous emission rate and is therefore the fundamental equation to describe the Purcell effect. This equation consists of four parts, highlighted by separating them in four fractions, which are addressed independently from each other. The first term describes the Purcell factor F_P, which only depends on parameters of the cavity:

$$F_P = \frac{3Q\left(\lambda_c/n\right)^3}{4\pi^2 V_{eff}} = \frac{3\lambda_c^3}{4n^3\pi^2} \frac{Q}{V_{eff}}. \tag{3.28}$$

Here, Q is the Q-factor of the cavity, λ_c is the wavelength, n is the refractive index of the cavity and V_{eff} is the effective mode volume. It quantifies the efficiency of the Purcell enhancement. The second term describes the density of states from equation 3.26 and highlights the effect of spectrally detuning the emitter and the cavity mode. The third term underlines the spatial detuning of the emitter to the cavity mode. The maximum Purcell enhancement is only achieved when the emitter is brought to the maximum of the electric field $\mathbf{E}_{max}$. Naturally, an emitter placed outside of the cavity mode will be unaffected and no Purcell enhancement is observed. The last term addresses a similar problem stemming from fluctuations in the cavity mode and incorporates the orientation of the dipole relative to the cavity field. In a perfect emitter where the emitter is spectrally and spatially in resonance with the cavity mode the Purcell enhancement is purely described by the first term (equation 3.28).

3.2.2 Exciton-polaritons in the strong coupling regime

As mentioned above, in the strong coupling regime a cyclic process of re-absorption and re-emission of cavity photons occurs. This coherent reversible transfer of energy leads to an energy splitting, called vacuum Rabi splitting, when the resonance condition is met. The two branches are described as quasi-particles called exciton-polaritons which is essentially a new eigenstate that arises from coupling two oscillators, in this case the photon and the exciton. The polariton describes the process where the exciton is annihilated when a photon is emitted with the same energy E and momentum k, which is again reabsorbed to create a new exciton with the same E,k and so on. The Hamiltonian of a semiconductor at fermionic level is given by the Schrödinger equation:

$$\begin{aligned} H = &\int \Psi(\mathbf{r})^{\dagger}\left(-\frac{\hbar^2}{2m}\nabla^2 + V(\mathbf{r})\right)\Psi(\mathbf{r})\,\mathrm{d}\mathbf{r} \\ &+\frac{1}{2}\int\int \Psi(\mathbf{r})^{\dagger}\Psi(\mathbf{r'})^{\dagger}\frac{e^2}{|\mathbf{r}-\mathbf{r'}|}\Psi(\mathbf{r'})\Psi(\mathbf{r})\,\mathrm{d}\mathbf{r}\mathrm{d}\mathbf{r'}. \end{aligned} \tag{3.29}$$

Here $\Psi(\mathbf{r})$ is the electron annihilation field operator and V the Coulomb potential. Neglecting spins and states other than $1s$ for the exciton, the dipole moment of the exciton, $e\mathbf{r}$, that couples to the light field $\mathbf{E}$ leads to the following coupling Hamiltonian:

$$H_{CX} = \int \Psi(\mathbf{r})^{\dagger}\left[-e\mathbf{r}\cdot\mathbf{E}(\mathbf{r})\right]\Psi(\mathbf{r})\,\mathrm{d}\mathbf{r}. \tag{3.30}$$

By adding this Hamiltonian to equation 3.29 and solving the nonlinear Schrödinger equation leads to the exciton-photon coupling Hamiltonian:

$$H = \sum_{k}\left[E_C(\mathbf{k})\,a_{\mathbf{k}}^{\dagger}a_{\mathbf{k}} + E_X(\mathbf{k})\,b_{\mathbf{k}}^{\dagger}b_{\mathbf{k}} + \hbar g(\mathbf{k})\left(a_{\mathbf{k}}^{\dagger}b_{\mathbf{k}} + b_{\mathbf{k}}a_{\mathbf{k}}^{\dagger}\right)\right]. \tag{3.31}$$

Here E_C and E_X are the energies of the cavity photon and the exciton, respectively. $a_{\mathbf{k}}^{\dagger}$ and $a_{\mathbf{k}}$ are creation and annihilation operators for the photon, $b_{\mathbf{k}}^{\dagger}$ and $b_{\mathbf{k}}$ are creation and annihilation operators for the exciton with the in-plane wavevector k. The Rabi splitting between upper and lower polariton branches is given by $\Omega_{Rabi} = 2g$ and, provided that the active material is placed at the maximum of the electric field in the cavity, is written as:

$$\hbar\Omega_{Rabi} = \sqrt{\frac{N_{QW}(\hbar e)^2}{2\varepsilon m_0 L_{eff}}f_{osc}}. \tag{3.32}$$

In equation 3.32 the assumption is made that the active material is a quantum well-like emitter which is larger than the spot probed in the experiment which is in general the case for monolayer sheets of 2D materials. N_{QW} is the number of such quantum wells, L_{eff} is the effective cavity length and f_{osc} is the oscillator strength of the transition. The Hamiltonian in equation 3.31 is diagonalized using the so-called Hopfield transformation using the following Hopfield coefficients:

$$L_{\mathbf{k}} = X_{\mathbf{k}} b_{\mathbf{k}} - C_{\mathbf{k}} a_{\mathbf{k}} \tag{3.33}$$

$$U_{\mathbf{k}} = C_{\mathbf{k}} b_{\mathbf{k}} + X_{\mathbf{k}} a_{\mathbf{k}} \tag{3.34}$$

The Hopfield coefficients C_k and X_k reveal the excitonic and photonic contribution to form the polariton state and $C_k^2 + X_k^2 = 1$. The diagonalized Hamiltonian is then written as:

$$H = \sum_k \left[E_U(\mathbf{k}) U_{\mathbf{k}}^\dagger U_{\mathbf{k}} + E_L(\mathbf{k}) L_{\mathbf{k}}^\dagger L_{\mathbf{k}} \right], \tag{3.35}$$

for quantized annihilation operators for upper ($U_{\mathbf{k}}$) and lower ($L_{\mathbf{k}}$) polariton branches (UPB and LPB respectively). This allows to extract the dispersion relation $E_{U,L}$ for UPB and LPB:

$$E_U(\mathbf{k}) = \frac{1}{2}\left[E_X(\mathbf{k}) + E_C(\mathbf{k})\right] + \frac{1}{2}\sqrt{\Delta_{\mathbf{k}}^2 + \hbar^2 \Omega_{Rabi}(\mathbf{k})^2} \tag{3.36}$$

$$E_L(\mathbf{k}) = \frac{1}{2}\left[E_X(\mathbf{k}) + E_C(\mathbf{k})\right] - \frac{1}{2}\sqrt{\Delta_{\mathbf{k}}^2 + \hbar^2 \Omega_{Rabi}(\mathbf{k})^2} \tag{3.37}$$

Here E_X and E_C are the excitonic and photonic dispersions respectively, and $\Delta_{\mathbf{k}} = E_C(\mathbf{k}) - E_X(\mathbf{k})$ describes the detuning of the exciton energy and the cavity mode. When the cavity mode and the exciton are in resonance ($\Delta_{\mathbf{k}} = 0$), the energy separation of LPB and UPB $[E_U(\mathbf{k}) - E_L(\mathbf{k})]$ is given by the vacuum Rabi splitting $\hbar\Omega_{Rabi}$. The anti-crossing for a strongly coupled system is shown in Figure 3.6(a).

For different detuning the polariton state consists of different photonic and exciton fractions, which means different probability that the polariton is in either one of these states.

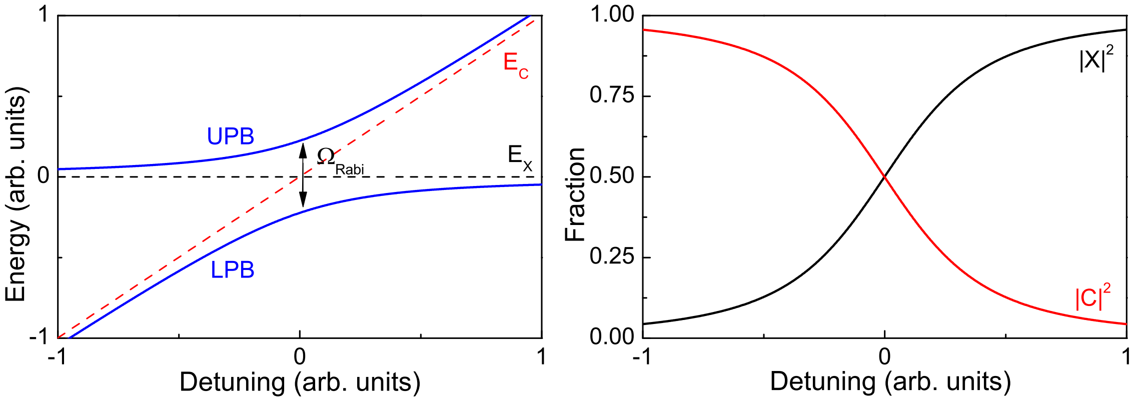

Figure 3.6: Anti-crossing and Hopfield coefficients in a strongly coupled system. The exciton energy is taken as constant around the exciton energy, while the cavity mode is tuned through the resonance condition. (a) The characteristic anti-crossing between the cavity and the emitter is shown with a Rabi splitting Ω_{Rabi}. (b) The Hopfield coefficients of the LPB show the excitonic (black line) and photonic (red line) fraction of the polariton as a function of detuning.

The fractions are given by the squared of the Hopfield coefficients and can be written as a function of the dispersion relations:

$$|C_{\mathbf{k}}|^2 = \frac{E_U(\mathbf{k})\,E_X(\mathbf{k}) - E_L(\mathbf{k})\,E_C(\mathbf{k})}{\left[E_C(\mathbf{k}) + E_X(\mathbf{k})\right]\sqrt{\Delta_{\mathbf{k}}^2 + \hbar^2\Omega_{Rabi}(\mathbf{k})^2}} \tag{3.38}$$

$$|X_{\mathbf{k}}|^2 = \frac{E_U(\mathbf{k})\,E_C(\mathbf{k}) - E_L(\mathbf{k})\,E_X(\mathbf{k})}{\left[E_C(\mathbf{k}) + E_X(\mathbf{k})\right]\sqrt{\Delta_{\mathbf{k}}^2 + \hbar^2\Omega_{Rabi}(\mathbf{k})^2}} \tag{3.39}$$

The two coefficients are shown for the LPB as a function of detuning in Figure 3.6(b). At large negative detuning the polariton is mostly of photonic character and possesses mostly photonic properties but becomes more and more excitonic when the cavity mode is tuned towards the resonance. For zero detuning the polariton consists of 50% excitonic and 50% photonic fraction and is therefore a half-light half-matter quasiparticle. When the cavity mode is tuned beyond resonance, the lower polariton state is mostly of excitonic nature. In the previous derivations the linewidth of excitons and photons have been neglected. Including finite linewidths, γ_X and γ_C for the exciton and photon linewidth respectively, to the model leads to imaginary components added to the Hamiltonians. In the case for exciton and photon energies the imaginary Hamiltonian writes as:

$$E'_X(\mathbf{k}) = E_X(\mathbf{k}) - \mathrm{i}\gamma_X \tag{3.40}$$

$$E'_C(\mathbf{k}) = E_C(\mathbf{k}) - \mathrm{i}\gamma_C \tag{3.41}$$

This allows to include the linewidth in the dispersion relation for the polariton branches and leads to:

$$E_U(\mathbf{k}) = \frac{E_X(\mathbf{k}) + E_C(\mathbf{k})}{2} - \mathrm{i}\frac{\gamma_X + \gamma_C}{2} + \frac{1}{2}\sqrt{\left[\Delta_{\mathbf{k}} - \mathrm{i}\left(\gamma_X - \gamma_C\right)\right]^2 + \hbar^2\Omega_{Rabi}(\mathbf{k})^2} \tag{3.42}$$

$$E_L(\mathbf{k}) = \frac{E_X(\mathbf{k}) + E_C(\mathbf{k})}{2} - \mathrm{i}\frac{\gamma_X + \gamma_C}{2} - \frac{1}{2}\sqrt{\left[\Delta_{\mathbf{k}} - \mathrm{i}\left(\gamma_X - \gamma_C\right)\right]^2 + \hbar^2\Omega_{Rabi}(\mathbf{k})^2} \tag{3.43}$$

Therefore, the Rabi splitting has to exceed the difference of the linewidth in order to resolve the two polariton branches and observe the strong coupling regime:

$$\left[\hbar\Omega_{Rabi}(\mathbf{k})\right]^2 > \left(\gamma_X - \gamma_C\right)^2. \tag{3.44}$$

If this is not the case and $\left[\hbar\Omega_{Rabi}(\mathbf{k})\right]^2 < \left(\gamma_X - \gamma_C\right)^2$, the energy splitting is imaginary and the system is therefore in the weak coupling regime. When the Rabi splitting becomes comparable to the linewidth of the exciton, which is the case for 2D materials, the experimentally observed Rabi splitting $\hbar\Omega'_{Rabi}$ is [98]:

$$\hbar\Omega'_{Rabi}(\mathbf{k}) > \sqrt{\left[\hbar\Omega_{Rabi}(\mathbf{k})\right]^2 - 2\left(\gamma_X^2 + \gamma_C^2\right)}. \tag{3.45}$$

Following this expression strong coupling is observed when $\left[\hbar\Omega_{Rabi}(\mathbf{k})\right]^2 > \gamma_X^2 + \gamma_C^2$. Otherwise the two polariton branches are not resolved at resonance and the system is not in the strong coupling regime. For Rabi splittings that are large enough to not result in an imaginary energy splitting but too small to resolve the polariton branches, the system is in the so-called intermediate coupling regime. In this case, however, a characteristic anti-crossing may still be observed in reflectivity measurements as shown in chapter 6.

4 Experimental methods

This chapter covers the experimental methods used in this work. At first the fabrication of mono- and few-layer sheets of 2D materials is discussed as well as the method to vertically stack thin films in order to produce heterostructure devices. Afterwards the experimental setups are explained used to obtain the results shown in chapter 5, 6 and 7. The final part of this chapter covers the design and principle of a tunable open-access microcavity setup.

4.1 Fabrication of monolayer sheets

In the introduction (chapter 1) the layered nature of graphite, boron nitride and chalcogenide crystals has been discussed. As mentioned above this allows to extract single atomic layers from the bulk crystals. Within recent years the technique to produce monolayer structures has developed rapidly and it is now possible to produce high-quality monolayer sheets using the so-called mechanical exfoliation technique as a top-down method. A different approach is the use of chemical vapor deposition (CVD) techniques [99] or molecular beam expitaxy (MBE) growth [100], as a bottom-up method with the aim towards scalability and reproducibility.

4.1.1 Mechanical exfoliation

Mechanical exfoliation or mechanical cleaving describes the process where an adhesive tape is applied onto a bulk crystal in order to peel off several layers of the material. The standard exfoliation technique is performed with an adhesive tape similar to wafer dicing

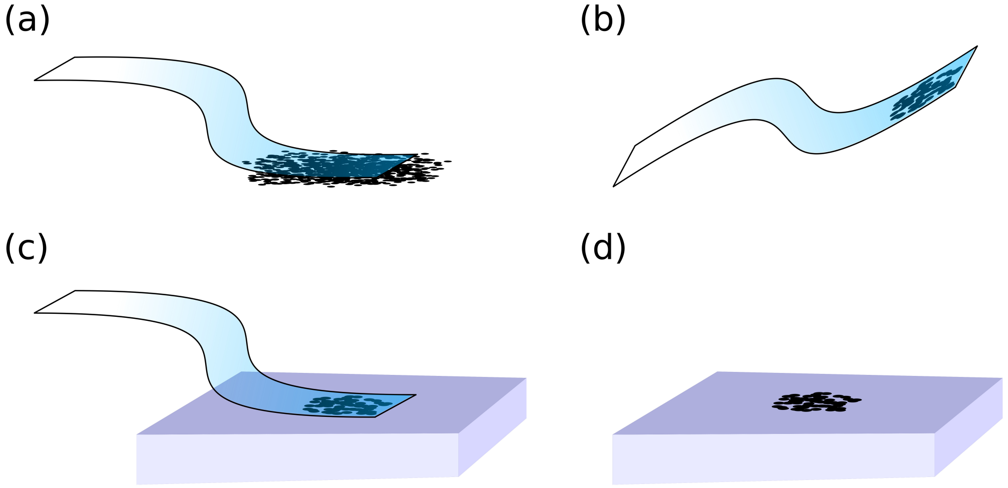

Figure 4.1: Mechanical exfoliation process. An adhesive tape is used to thin down layered materials towards monolayer thickness. (a) The tape is applied onto the bulk crystal, which (b) breaks and a piece of the material sticks on the tape. If required, another end of the adhesive tape is applied on the material, thinning down the material further after peeling off the tape. (c) The tape with the material is applied on the target substrate and (d) peeled off again. A thin film of the material remains on the target substrate because van der Waals forces on the surface are larger than the inter-layer bonding of the layered materials.

tapes used for protecting the surface of semiconductor wafers during the cutting of the wafers using a micrometer saw. These tapes leave little to no glue residue on the substrate and are therefore ideal for this process. When the tape is applied on the bulk crystal it is possible to break a few layers off due to the weak van der Waals forces of the crystal lattice. The few layer-thick material remaining on the tape is thinned down further by applying another tape which is peeled off again. This process is repeated several times to produce thinner and thinner sheets. Eventually the tape is placed on a target substrate and the tape is carefully peeled off the sample. Van der Waals forces on the surface of the sample ensure that binding onto the substrate is stronger than the inter-layer bonding, therefore the crystal breaks one last time and the material is successfully transferred onto the target substrate [10, 101]. Figure 4.1 shows a schematic of the different steps during the exfoliation process. Using this method it is possible to produce monolayer sheets. However this method suffers from several drawbacks.

First of all it is not guaranteed to obtain single atomic layers but instead results in a wide spread of thin films with various thicknesses. Furthermore, this method usually also leads

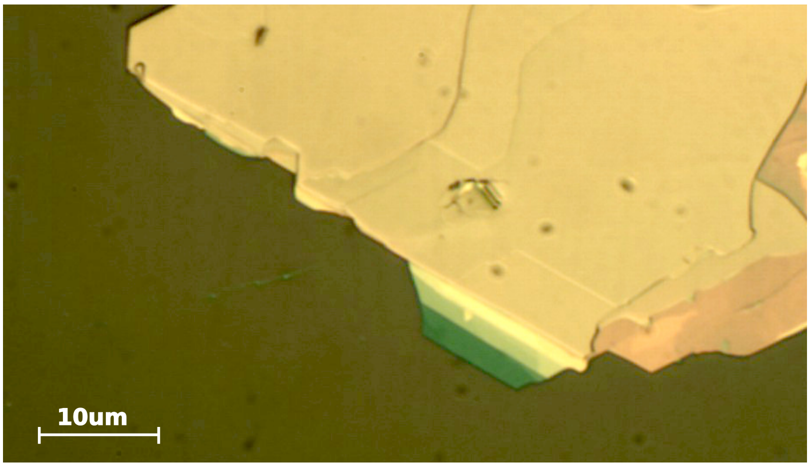

Figure 4.2: Gallium selenide thin film. The galium selenide film shows terraces with different thicknesses towards the edge of the sheet. The thickness of this sheet is ranging from 100 nm to 10 nm.

to thin films with small lateral dimensions. It is also common that a sheet does not break consistently and therefore terraces form resulting in a sheet with different thicknesses instead of an isolated monolayer sheet. An example of this is given in Figure 4.2 which shows a gallium selenide sheet with several different thicknesses on the same sheet. A way to overcome this issue is to apply the tape on the target substrate right after the first exfoliation step. This usually leaves large, thick sheets on the surface. Applying another tape carefully on the exfoliated sheets allows to peel off a layer, leaving a thinner sheet on the target substrate. This is again repeated until a monolayer sheet remains on the target substrate.

4.1.2 Transfer of monolayer structures onto arbitrary substrates

In principle the techniques described above allow the fabrication of monolayer sheets on arbitrary substrates. In most cases, however, the image contrast of a monolayer sheet is not high enough to locate them on arbitrary substrates. To reliably confirm the thickness of an exfoliated sheet atomic force microscopy (AFM) measurements are performed. This time-consuming process can be skipped, however, when the target substrate is chosen in a way that a monolayer sheet is visible under an optical microscope. The most commonly used

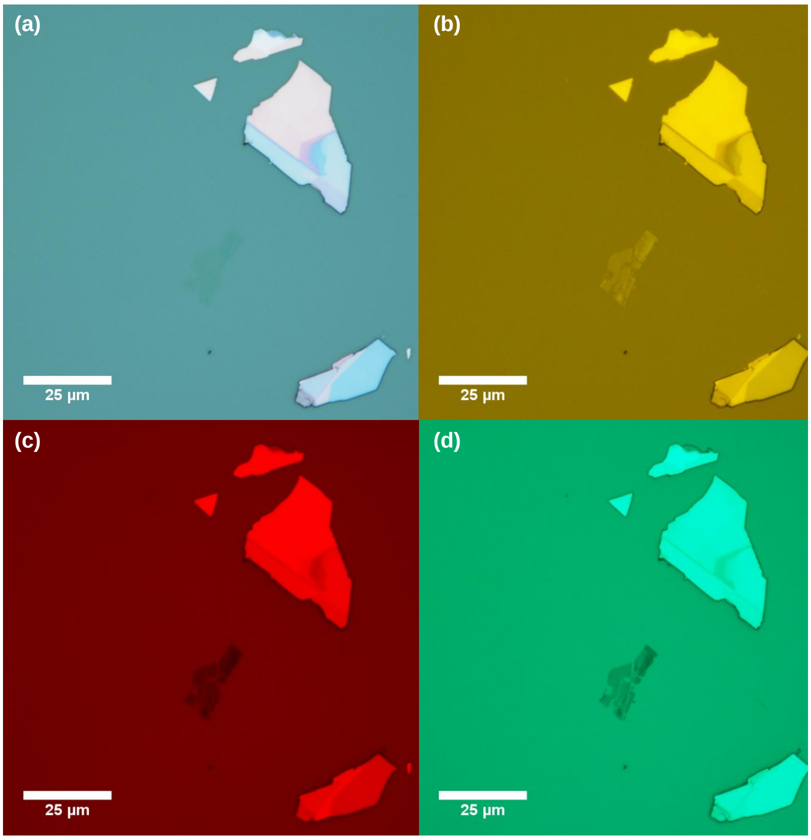

Figure 4.3: Optical microscope image of a WSe_2 monolayer sheet. Using bandpass filters in the microscope allows to enhance the contrast of monolayer sheets significantly. (a) The exfoliated monolayer is hardly visible on the polymer substrate. (b)-(d) The use of different bandpass filters increases the contrast of the monolayer. When wavelength of the filters leads to constructive interference with the underlying substrate, the contrast can be maximized in order to obtain a detailed image of the monolayer sheet.

semiconductor substrate, especially in electronics, is silicon. The contrast of a monolayer sheet on silicon can be significantly enhanced by growing a 290 nm layer of silicon dioxide (SiO_2) on the silicon surface, due to interference effects. The contrast can be further increased by using narrow bandpass filters as shown in Figure 4.3. For many applications the monolayer sheet needs to be placed on other types of substrates. Instead of exfoliating directly onto the desired substrate, the silicon/SiO_2 substrate is used to identify the exfoliated monolayer structures and the monolayers are then transferred to the target substrate [102]. Several techniques have been developed to optimize the quality of the monolayer materials after the transfer. In general there are two different approaches called *wet-transfer* or *dry-transfer*.

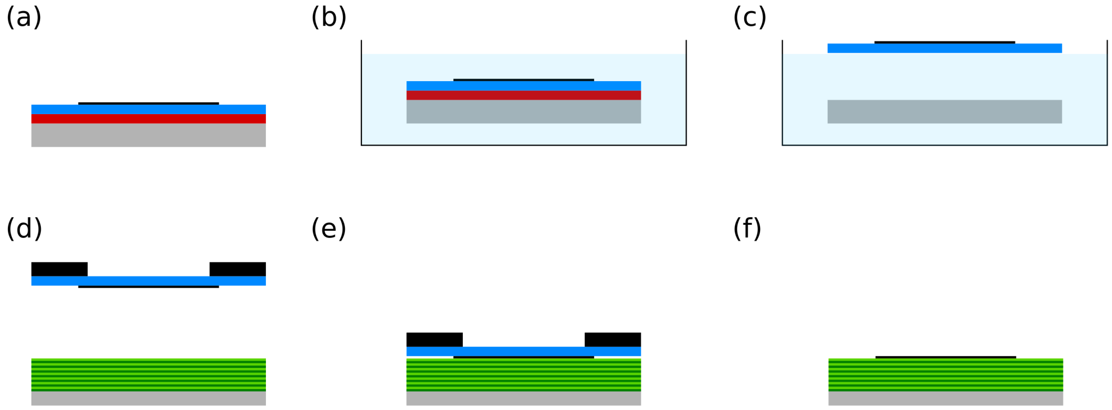

Figure 4.4: Schematic of a wet transfer procedure. The first step is to spin-coat two polymers on the Si/SiO$_2$ substrate. The first solvent is water-soluble, such as PMGI for example, the second is a hydrophobic polymer, typically PMMA. (a) The monolayer sheet is then exfoliated on top of the polymers. (b) By placing the sample in DI water, the PMGI film dissolves and (c) the monolayer film, sitting on the PMMA, is swimming on the top of the DI water. (d) The polymer is fetched out with a holder, turned upside-down and arranged on top of the target substrate. (e) The film is brought in contact with the target substrate and by heating up the substrate the polymer melts and the monolayer is sitting on the substrate. (f) Finally, the polymer is washed off in acetone and the monolayer remains on the substrate.

Wet transfer of monolayer structures

For the *wet-transfer* method two polymers are deposited onto the silicon/SiO$_2$ substrate before the exfoliation [103]. While the first polymer is water-soluble, a commonly used polymer for this layer is polymethylglutarimide (PMGI), the second one is hydrophobic, mostly polymethyl methacrylate (PMMA). After the monolayer sheets are exfoliated onto the PMMA film, the sample is placed in deionized water (DI water) which dissolves the PMGI film and the hydrophobic PMMA film remains on the surface of the DI water. This allows to fish out the PMMA layer with the monolayer structures. The monolayer structures are then placed on top of the target substrate and the substrate is heated up to around 75°C - 100°C to melt the polymer so that it adheres strongly on the surface. Finally, the PMMA film is washed off using acetone and the monolayer remains on the target substrate. A schematic of this procedure is shown in Figure 4.4.

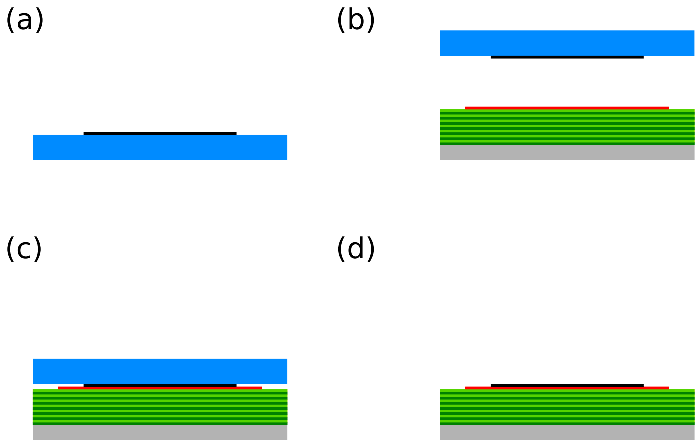

Figure 4.5: **Schematic of a dry transfer procedure.** (a) The monolayer sheet is exfoliated on top of a viscoelastic material, such as PDMS for example. (b) The PDMS is then used to align the monolayer sheet with the desired position on the target substrate, which maybe a previously exfoliated monolayer. (c) The materials are brought in contact where the thin film preferentially adheres to the substrate. (d) The PDMS is peeled off and the thin film remains on the target substrate.

Dry transfer of monolayer structures

Using several polymers and solvents can reduce the quality of the monolayer structure. Therefore a *dry-transfer* method was developed to produce high-quality samples. In order to improve the transfer method polydimethylsiloxane (PDMS) or other viscoelastic materials instead of PMMA are used. PDMS is a solid material which can be peeled off after the transfer and, therefore, no acetone is required to wash it off. This stamping method works because the viscoelastic material has a direct contact with the thin film and the thin film preferentially adheres to the target substrate than the viscoelastic material. By slowly peeling off the stamp the viscoelastic material detaches leaving the thin film on the target substrate as shown in Figure 4.5 [104].

Two-dimensional heterostructures

In order to produce high-quality heterostructures consisting of two-dimensional materials a clean transfer of monolayer sheets and a defect free stacking is required. The heterostructures used in this work have been produced using the method described in the previous

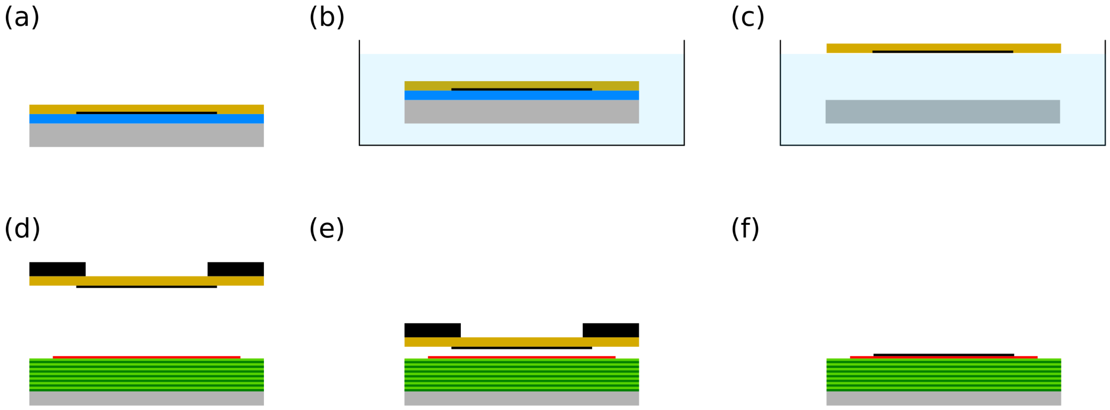

Figure 4.6: Transfer of an entire heterostructure. After an entire heterostructure has been produced on a smooth Si/SiO$_2$ substrate, the structure can then be transferred, as a whole, onto a target substrate. (a) PMMA is spin-coated on top of the heterostructure. (b) The sample is placed in KOH acid in order to etch the SiO$_2$ layer of the substrate and (c) the heterostructure and the PMMA film swim on the surface of the acid. (d) Similar to the wet transfer, the polymer is fetched out and aligned with the target substrate. (e) The materials are brought in contact and the substrate is heated up so that the polymer melts. (f) After washing off the PMMA, the heterostructure remains on the target substrate.

paragraph. The stamping method also allows to pick up the next monolayer sheet as the previous material is applied onto it where no viscoelastic material is required in between. This is possible when the inter-layer bonding of the different van der Waals crystals is larger than the bonding force of the monolayer and the substrate. This allows to stack layer by layer until the entire heterostructure is produced. This process is generally done on a Si/SiO$_2$ substrate so that the monolayer structures can be located in the microscope for the subsequent transfer process. It is then possible to transfer an entire heterostructure stack to a target substrate at once using the *wet-transfer* method where the carrying substrate is etched after the PMMA film is deposited on top of the heterostructure, this is shown in Figure 4.6.

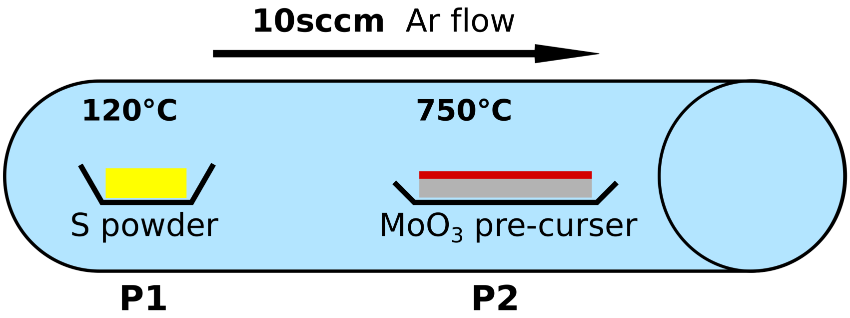

Figure 4.7: **CVD growth in a furnace.** A prepared MoO_3 thin film, sitting on a substrate, is placed in position $P2$ and sulphur powder is put at position $P1$. The two positions are heated up to 750°C and 120°C, respectively. By applying an argon flow of 10 sccm the evaporated sulphur is transported to the sample in order to sulphurize the MoO_3 film to form MoS_2.

4.1.3 Chemical vapor deposition of two-dimensional materials

The downside of mechanical exfoliation is that it is not reproducible or scaleable and therefore limits the possibilities for industrial applications. In order to grow monolayer structures consistently, various chemical vapor deposition (CVD) methods are being developed [99]. In case of TMDCs the most promising method thus far has been sulphurization of transition-metal oxides, molybdenum or tungsten tri-oxide (MoO_3 and WO_3). This process is typically done in a furnace as schematically shown in Figure 4.7.

To grow thin films of TMDCs the starting material should be thin already. To achieve this the $Mo(W)O_3$ is thinned down to small sheets of mono- and few-layer thickness using a sonication method. The $Mo(W)O_3$ layers are then placed on the target substrate and placed at position $P2$ in Figure 4.7. The sulphur is placed at position $P1$ and both positions are heated locally to $T_{P1} = 120°C$ and $T_{P2} = 750°C$, respectively. An argon flow of 10 sccm then causes the evaporated sulphur to travel on top of the target substrate where a chemical reaction leads to the formation of $Mo(W)S_2$ [105]. During the CVD growth it is thermodynamically favourable to terminate at the Mo atoms because these are the most energetically favourable terminations. The hexagonal crystal lattice then leads to the growth of islands with triangular shape with the least dangling bonds at the edges of the triangle, as indicated in Figure 4.8 [106–108]. Only when the triangular islands start to emerge a continuous film is produced.

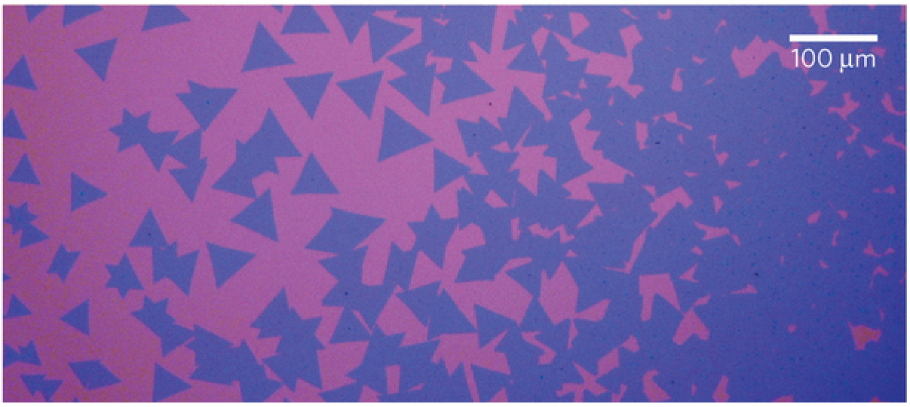

Figure 4.8: Optical image of CVD grown MoS_2. The triangular shape of the CVD grown monolayer sheets stems from the increased growth rate at the Mo atoms [105].

4.2 Photoluminescence measurements

Although the exciton binding energy in monolayer TMDCs allows strong PL emission at room temperature, most of the experiments are performed at cryogenic temperatures. where excitonic features are narrow and trion states are clearly observed. To characterize a large number of samples at cryogenic temperatures a helium continuous flow cryostat is used where the sample is placed in vacuum on a cold finger which allows to cool down the sample to roughly 10 K. All the results presented in this work, however, are perfomed in a helium bath cryostat where the sample is placed into a cryostat that is filled with helium and reaches a constant temperature of 4.2 K. The advantage of this system is that it operates without a pump and is therefore more stable than a continuous flow cryostat system. The sample is mounted on top of nanopositioners that allow accurate control of motion. The collection lens is placed on top of the sample, also inside the helium bath cryostat, which has optical access through the top. The optics is placed on a board located on top of the cryostat and the excitation laser as well as the collected emission is coupled into optical fibers.

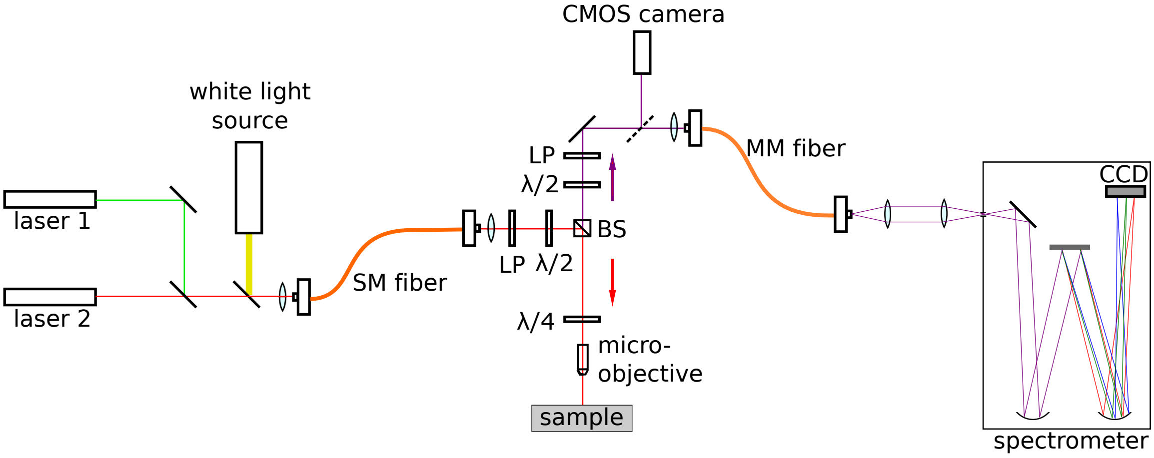

Figure 4.9: Schematic of a PL setup. The PL setup allows to use either a red diode laser or a green solid state laser. Additionally the option of a white-light source, which is used to locate the monolayer sheets on the sample, is provided. The excitation path is coupled through an optical single-mode (SM) fiber, through a beamsplitter and focused onto the sample. The emission is collected through the same objective and coupled through an optical multi-mode (MM) fiber after which the signal is focused onto the slit of the spectrometer. A CMOS camera is used to align collection and excitation paths and to navigate on the sample. Finally, after the spectrometer, the frequency-resolved signal is collected by a nitrogen cooled CCD camera.

4.2.1 Continuous-wave excitation

The concept of PL measurements has been introduced in chapter 2.1.1. The excitation laser used in the experiments depends on the material that is studied. In case of WSe_2 and $MoSe_2$ (chapter 6 and 7) the PL emission is measured around 1.72 eV (720 nm) and 1.65 eV (750 nm), respectively. A laser diode emitting at 1.94 eV (638 nm) is used to excite above the bandgap. In case of MoS_2 and GaSe, studied in chapter 5, the PL emission around 1.9 eV (650 nm) and 2.05 eV (605 nm), where a solid state laser emitting at 2.33 eV (532 nm) is used. The collected emission is coupled into an optical fiber and guided to a 0.75 m single spectrometer. The PL signal is then collected by a charge coupled device (CCD) camera. A schematic of the PL setup is shown in Figure 4.9.

In order to perform polarization dependent measurements the laser excitation, which is nearly unpolarized after the the optical fiber of several meter length, is polarized with a linear polarizer. A $\lambda/4$ waveplate, that can be flipped in and out, is placed under the beam-splitter and converts the linear polarized light in circular polarized light. It then also converts the circularly polarized emission into linearly polarized light which is then probed with a linear polarizer in the collection path. In order to study the polarization degree a $\lambda/2$ waveplate is used to rotate the linear polarization before the linear polarizer element.

4.2.2 Time-resolved measurements

Time-resolved measurements have been performed with a femto-second pulsed, tuneable titanium sapphire (Ti:Sapphire) laser. The Ti:Sapphire laser is tuned to 800 nm and the pulse duration of the laser is 300 fs with a repetition rate of 80.2 MHz. In order to excite above the bandgap of the materials, the pulse is frequency-doubled using a non-linear crystal. After second harmonic generation the emission is converted to 400 nm, which is coupled to the single-mode fiber. Through temporal dispersion when the pulse is propagating through the fiber, the pulse duration is in the order of 1 ps at the end of the fiber, limiting the resolution of the time-resolved measurements to the order of several picoseconds. The emission is collected by a single mode fiber in order to minimize the temporal dispersion of the time-resolved emission. The time-resolved emission is guided through a spectrometer and collected using a streak camera. The slit of the spectrometer is opened for this measurement in order to increase the time resolution of the experiment at the cost of spectral resolution. The streak camera has a time resolution of 2 ps. The collected emission is projected onto a slit and focused on a photocathode in the streak tube.

4.3 Tunable open-access microcavity system

This section describes the design and properties of a tunable open-access microcavity system. The principle of a microcavity is described in chapter 3 where its parameters as well as the exciton-photon coupling with an active material is described. A tunable system offers many advantages to study the exciton-photon coupling, especially in systems which are not well understood so far, such as 2D materials for example. The open cavity is formed by two distributed Bragg reflectors (DBR) that are separated by each other. The two DBRs

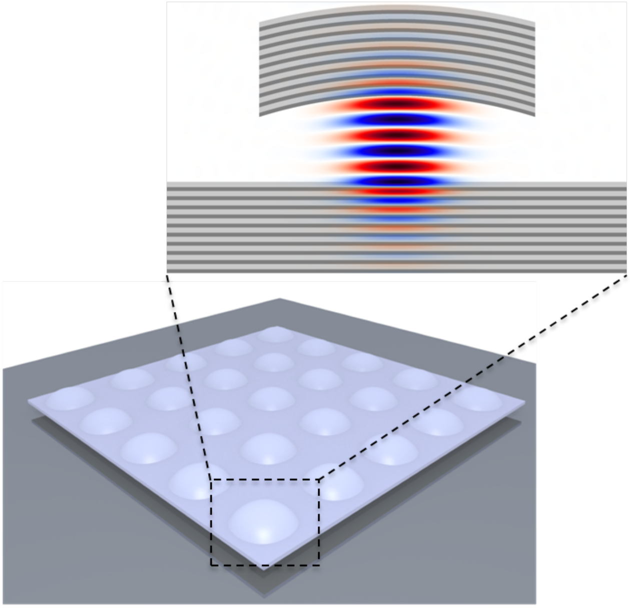

Figure 4.10: **Schematic of the open cavity design.** A concave top mirror and a planar bottom mirror form the hemispheric cavity. An array of concave mirrors is produced by ion beam milling to produce the top mirror. The DBRs consist of 10 pairs SiO_2/NbO_2. The inset shows the schematic of the cavity with the electric field anti-node at the surface of the planar mirror.

are controlled independently from each other, by two independent sets of nanopositioners. A schematic of the formed open cavity and its mirror design is shown in Figure 4.10. The concave shaped top mirror leads to a confinement of the cavity mode in all three dimensions. This results in a reduced cavity mode volume and, therefore, an enhanced coupling strength. A detailed schematic of the experiment is shown in Figure 4.13 and will be discussed at the end of this chapter.

The two DBRs are fabricated using an ion assisted sputtering deposition method where 10 pairs of SiO_2/NbO_2 are grown on silica substrates [109, 110]. As indicated in Figure 4.10 the top mirror is of concave shape in order to form a hemispherical resonator. The concave shape is produced by the group of Jason Smith at the University of Oxford by focused ion beam milling before the dielectric deposition. The bottom mirror is a planar DBR where the monolayer structures are transferred onto after mechanical exfoliation [109]. The fabrication of the concave structures is done using focused ion beam milling where a gallium ion is accelerated onto a silica substrate in order to mill into the surface. By varying the dwell time, the shape of the milled feature is controlled. Using this process an

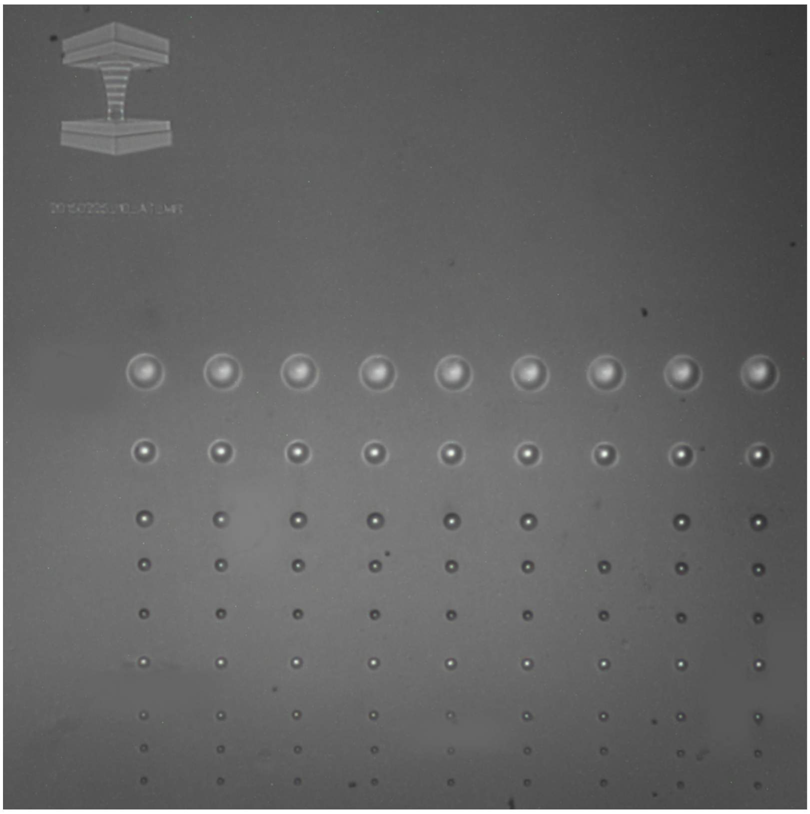

Figure 4.11: Microscope image of the concave top mirrors. The array of concave mirrors with different RoC, ranging from 20 μm to less than 1 μm is shown. The smallest RoC used in experiment is 5.6 μm. The concave shape mirrors are produced by the group of Jason Smith at the University of Oxford.

array of concave mirrors with different radius of curvature (RoC) ranging from 5.6 μm to 25 μm are produced on the sample, as shown in Figure 4.11. The advantage of using this method is the low surface roughness of less than 0.7 nm in the concave feature, which is better than the unprocessed silica surface of the substrate.

4.3.1 Hemispherical microcavity

Before the design is discussed in more detail, the physical properties of hemispherical microcavities are explained. The concave top mirror leads to a confinement of the cavity mode in all three dimensions and, therefore, to a reduction of the cavity mode volume in order to enhance the light-matter interaction. From equation 3.27, for example, it is directly obvious that a reduced mode volume V_{eff} leads to an increased Purcell enhancement. From an experimental point of view the concave top mirror allows higher Q-factors of the cavity mode because the cavity mode is less susceptible to beam walk-off which occurs in planar cavities when the DBRs are not perfectly parallel.

The electric field profile within a hemispherical cavity is derived from the scalar wave equation in vacuum, given by [114]:

$$\nabla^2 E\left(r,t\right) - \frac{1}{c^2}\frac{\partial^2}{\partial t^2}E\left(r,t\right) = 0. \tag{4.1}$$

Here $E\left(r,t\right)$ is the electric field and c is the speed of light. In case of a monochromatic plane wavefunction, where $E\left(r,t\right) = E\left(r\right)\mathrm{e}^{-\mathrm{i}\omega t}$, equation 4.1 can be written as the scalar Helmholtz equation:

$$\nabla^2 E\left(r\right) + k^2 E\left(r\right) = 0, \tag{4.2}$$

where $k^2 = \omega^2/c^2$ is the wavevector. This equation has several solutions for different wave patterns. The so-called paraxial approximation, where $E\left(\mathbf{r}\right) = E_0\left(\mathbf{r}\right)\mathrm{e}^{\mathrm{i}kz}$, is a *small-angle approximation*, where the derivation in equation 4.2 is reduced to the transverse part of the Laplacian, $\nabla_\perp^2 = \frac{\partial^2}{\partial x^2} + \frac{\partial^2}{\partial y^2}$. Equation 4.2 is then given by:

$$\nabla_\perp^2 E\left(r\right) + 2\mathrm{i}k\frac{\partial E\left(r\right)}{\partial z} = 0. \tag{4.3}$$

It can be shown that the solution of this equation takes the form:

$$E\left(r\right) = \frac{A\mathrm{e}^{\mathrm{i}\phi(z)}}{\sqrt{1+\frac{z^2}{z_R^2}}}\mathrm{e}^{\mathrm{i}k\frac{x^2+y^2}{2RoC}}\mathrm{e}^{-\frac{x^2+y^2}{\omega^2(z)}}. \tag{4.4}$$

This equation describes a Gaussian beam where $\omega(z)$ is the beam waist, RoC is the radius of the curvature of the phase profile and $\phi(z) = \tan^{-1}\left(\frac{z}{z_R}\right)$ is the Gouy phase shift. In a hemispherical cavity the electric field profile has a Gaussian beam profile, modified due to the confinement of the mode. The radius of curvature (RoC) is a boundary condition where the phase front of the beam has to match the curvature of the mirror. The minimum of the beam waist is located on the surface of the planar mirror if the stability criteria, that the cavity length L is smaller than the RoC, is fulfilled.

The eigenfrequencies, $\nu_{q,m,n}$, of the cavity modes are given by:

$$\nu_{q,m,n} = \frac{c}{2n_c L_{opt}} \left[q + \frac{m+n+1}{\pi} \cos^{-1} \left(1 - \frac{L_{cav}}{\mathrm{RoC}} \right) \right], \tag{4.5}$$

where n_c is the refractive index of the cavity, q, m, n are the mode numbers of the cavity, L_{opt} is the optical cavity length and L_{cav} is the physical cavity length. The physical cavity length L_{cav} differs from the optical cavity length L_{opt} because the cavity mode penetrates into the DBRs. The penetration depth depends on the refractive index contrast of the dielectrics used to fabricate the DBRs and is found to be 0.625 μm for each DBR using the design described above. The physical cavity length is then the optical cavity length minus the total penetration depth, $L_{cav} = L_{opt} - 1.25\mu$m. The mode numbers are used to describe the set of solutions for the wave equation with q as the longitudinal mode index and m, n the transverse mode indices. The longitudinal mode spacing, Δq, with $m = n = 0$ results in:

$$\Delta\nu = \frac{c}{2n_c L_{opt}} \Delta q. \tag{4.6}$$

Therefore it is possible to extract the optical cavity length by measuring the separation of two longitudinal cavity modes. Additionally, the transverse mode spacings allow to extract the effective radius of curvature:

$$\Delta\nu_{trans} = \frac{c}{2n_c L_{opt}} \frac{\Delta m + \Delta n}{\pi} \cos^{-1} \left(1 - \frac{L_{cav}}{\mathrm{RoC}} \right). \tag{4.7}$$

The mode profile for the different mode indices are obtained by expanding the paraxial approximation with the hemispherical structure in the x-y plane. The solutions of the second order differential equation:

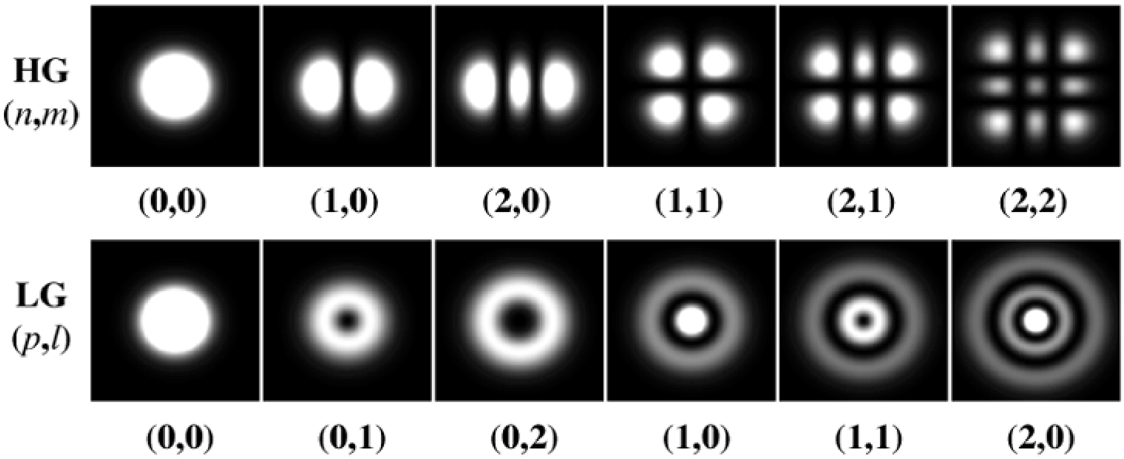

Figure 4.12: Electric field profile Hermite-Gaussian and Laguerre-Gaussian modes. The first 6 Hermite- (HG) and Laguerre-Gaussian (LG) modes are shown, demonstrating the difference between the observed modes. In the open cavity Hermite-Gaussian modes are observed. Figure is taken from [111].

$$\frac{\mathrm{d}^2}{\mathrm{d}u^2} - 2u\frac{\mathrm{d}F}{\mathrm{d}u} + \frac{c}{2}F = 0 \tag{4.8}$$

is given by the Hermite polynomials H_{mn}. The electric field of the Hermite-Gaussian modes, with the transverse indices m and n describing the Hermite polynomial order, are given by:

$$E_{m,n}(r) = E_0 \frac{\omega_0}{\omega(z)} H_m\left[\frac{\sqrt{2}x}{\omega(z)}\right] H_n\left[\frac{\sqrt{2}y}{\omega(z)}\right] \mathrm{e}^{\mathrm{i}\left[kz-(m-n-1)\tan^{-1}\left(\frac{z}{z_0}\right)\right]} \mathrm{e}^{\left(\mathrm{i}k\frac{r^2}{2R(z)} - \frac{r^2}{\omega_z^2}\right)}. \tag{4.9}$$

In case the paraxial wave equation is written in cylindrical coordinate basis, used for cylindrical micropillars or mesa, for example, the solutions are described by Laguerre-Gaussian modes. Figure 4.12 shows the electric field profile of Hermite-Gaussian and Laguerre-Gaussian modes. In the experiment perfect cylindrical systems are difficult to realize and therefore Laguerre-Gaussian modes are often not observed, but instead elliptically symmetric Mathieu- or Ince-Gaussian modes are measured.

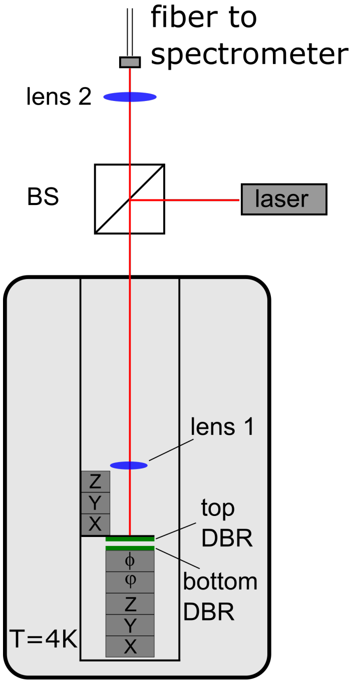

Figure 4.13: Schematic of open cavity setup. The two mirrors are placed on two independent sets of nanopositioners to have complete control of both mirrors. The cavity is placed in a helium bath cryostat allowing measurements at cryogenic temperatures.

4.3.2 Microcavity setup

The two DBRs mounted on the independent set of nanopositioners are placed in a helium bath cryostat [112]. A schematic of the setup is shown in Figure 4.13. This configuration allows to move the top mirror out of the optical path to study the PL of the monolayer material [113]. One concave structure of the top mirror is then moved on top of the monolayer structure and the emission couples to the cavity modes. With this cavity design mode volumes as low as $1.6\mu m^3$ and quality factors, Q, up to 7400 have been achieved [113]. This design allows tunability of the cavity size by adjusting the vertical displacement of the two mirrors and, therefore, allows spectral matching of the cavity mode wavelength with the emission wavelength in the cavity. The tunability is limited only by the width of the stopband of the DBRs, which is in this case about 180 nm.

5 Weak coupling of MoS_2 in a tunable microcavity

The optical properties of monolayer TMDCs discussed in chapter 2 revealed their interesting and unique characteristics but also exposed downsides of this class of materials. One of them is the relatively low emission efficiency which makes a practical use for optoelectronic devices based on those materials difficult. In this chapter the coupling of monolayer MoS_2 and few-layer GaSe with the tunable external cavity discussed in chapter 4.3 is shown. This cavity design helps to overcome this issue and allows better control of the light-matter interaction due to the tunability of the system. This type of microcavity has recently been found to be very promising in order to study light-matter interaction in conventional III-V semiconductors where polariton condensation [112, 115], or the formation of spin-vortices have been reported [116], but also in other material classes such as nitrogen vacancies in diamond, for example [117, 118]. A schematic of the open cavity design, showing the array of concave shaped mirrors milled into the top mirror, as well as the calculated electric field of the cavity mode is shown in Figure 5.1(a). The radii of curvature (RoC) used in this experiment are 5.6, 10 and 16 μm for MoS_2 and 25 μm for GaSe. The DBRs are designed as discussed above where the thickness of the dielectrics have been adjusted so that the stopband of the DBR is centered at around 650 nm as shown in the reflectivity spectrum in Figure 5.1(b). The reflectivity spectrum shows the broad stopband within the cavity experiments can be carried out. The wavelength of the excitation laser is outside the stopband, in the first minima of the reflectivity, so that only $\sim$30% is reflected when exciting through the laser.

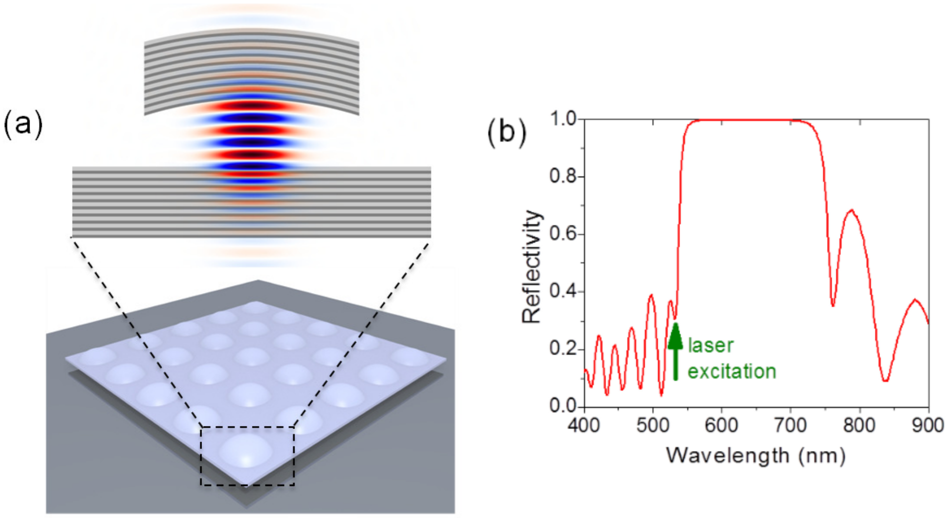

Figure 5.1: Schematic of the open cavity. (a) As a reminder, the schematic shows the array of concave mirrors milled into the top DBR and the calculated electric field inside the microcavity. It is shown that anti-node of the electric field is at the surface of the planar DBR in order to maximize the light-matter interaction. (b) A reflectivity spectrum of the DBR shows the broad stopband of the mirror. Experiments can be carried out in the wavelength range of that stopband.

5.1 Molybdenum disulphide

Figure 5.2 shows the optical image of a monolayer sheet of MoS_2. The gold stripes in the figure are used to overcome fabrication issues during the transfer of the monolayer sheet onto the dielectric mirror. The transfer technique used for this sample is the *wet-transfer* described in chapter 4.1. Compared to very smooth surface of thermally grown silicon oxide, the surface roughness of the grown dielectric DBRs is increased and wrinkles and bumps are present on the surface. While the root-mean-square (RMS) roughness of thermally grown SiO_2 is in the order of 0.2 to 0.3 nm, the RMS roughness of DBRs can be in the order of several nanometer. The increased roughness means that the monolayer sheet is less likely to stick to the surface when the PMMA film is washed off after the transfer technique. The PMMA film used for the transfer is patterned using an electron beam lithography and the gold stripes are deposited using an evaporation process. Afterwards the PMMA is washed off and the monolayer sheet remains on the surface of the DBR. The sample shows a monolayer area in light-green, the dark-green area corresponds to a film thickness of several nanometers.

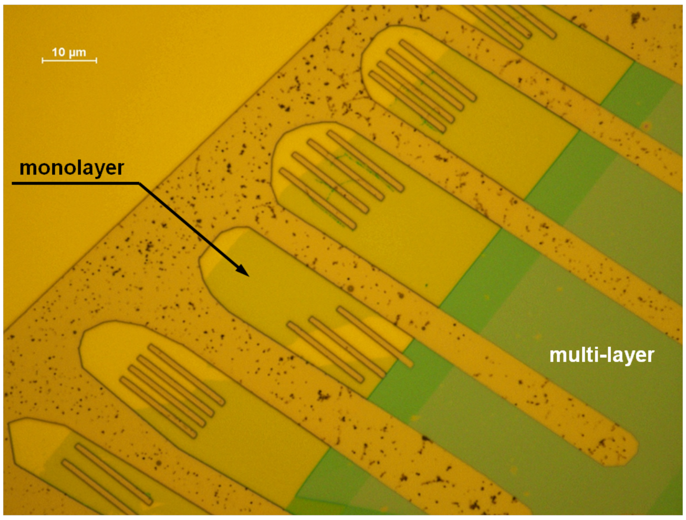

Figure 5.2: Optical microscope image of a MoS_2 monolayer sheet on top of the bottom DBR. The highlighted light-green layer shows the monolayer area, the dark-green area shows an area of few-layer MoS_2. The gold stripes are used as markers and to fixate the monolayer area onto the bottom DBR.

The PL emission from the monolayer sample on the DBR is shown in Figure 5.3. The neutral exciton is dominating the signal and due to the large PL linewidth neutral and charged exciton cannot be resolved [119].

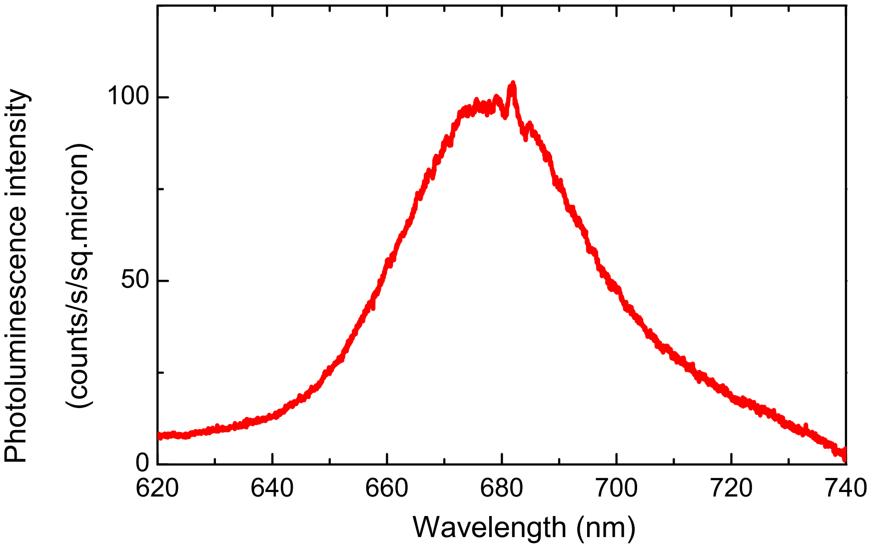

Figure 5.3: Typical PL spectrum of monolayer MoS_2 at cryogenic temperature. The spectrum consists of a neutral exciton, centered at around 680 nm with a linewidth of 40 meV. The charged exciton is not resolved due to the large linewidth. Apart from the excitonic feature a shoulder at lower wavelength, attributed to localized defect states, is observed.

As the concave mirror is placed over the monolayer to form a cavity, the broad PL emission is coupled to narrow cavity modes with a linewidth of less than 1 meV for the longitudinal mode. This is demonstrated for three different radii of curvature in Figure 5.4. The cavity length is adjusted to bring the longitudinal cavity mode in resonance to the maximum of the PL emission for the concave mirrors with RoC of 16, 10 and 5.6 μm. The measured Q-factors for the longitudinal modes in the spectra are 4000, 3000 and 1800, respectively. Higher order modes are also observed at shorter wavelength. To compare the PL intensity, the amplitude of the cavity modes is divided by a factor of 20, 10 and 5 for the mirrors with the different RoC, respectively.

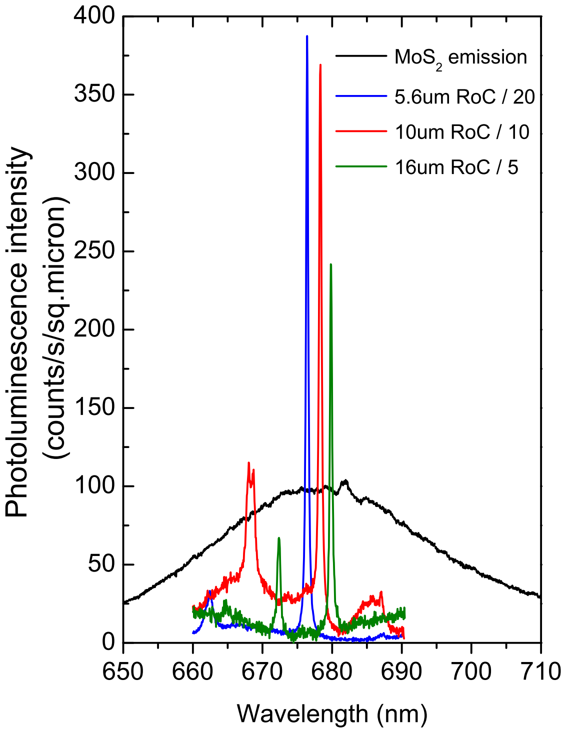

Figure 5.4: MoS$_2$ emission coupled to narrow bandwidth cavity modes. The broad and weak PL emission of monolayer MoS$_2$ is coupled into narrow cavity modes. By tuning the separation of the mirrors, the cavity mode is tuned in resonance with the exciton energy of the MoS$_2$ sheet for RoCs of 5.6, 10 and 16 μm.

Although the laser spot is similar in the full- and half-cavity (experiment with the top mirror moved out of the optical path) experiment, the waist diameter of the longitudinal modes is ≈ 1 μm. Thus in the case of the full cavity, PL is collected from a film area about 50 times smaller than in the case of a film placed on a planar DBR. This is accounted for in Figure 5.4 by using units of counts per second per square micron for PL intensity.

In other words, the emission is assumed to originate from a spot with diameter of 1 μm and 7 μm for the 'full-' and 'half-cavity' configurations, respectively. The observed PL intensity is 10, 30 and 60 times higher in the full cavity for a RoC of 16, 10 and 5.6 μm. For each measurement the longitudinal mode is tuned in resonance with MoS_2 PL roughly at the same wavelength. For this, the cavity length is adjusted to to $L_{cav} \approx 1.9$ μm for the mirrors with RoC=5.6 and 10 μm, and $L_{cav} \approx 2.9$ μm for the mirror with RoC=16 μm. As described above, the wavelength of the cavity mode can be tuned by changing the cavity length with:

$$\frac{1}{\lambda_{q,m,n}} = \frac{1}{2L_{opt}} \left[q + \frac{m+n+1}{\pi} \arccos \left(1 - \frac{L_{cav}}{\mathrm{RoC}} \right) \right] \tag{5.1}$$

Here, q, m and n are longitudinal (q) and transverse (m, n) mode numbers for Hermite Gauss cavities. L_{opt} is the effective optical length of the cavity, which differs from the physical length L_{cav} due to penetration of the cavity mode into the DBRs. To demonstrate the weak coupling regime the cavity modes are tuned through the exciton resonance of the MoS_2 film by changing the cavity length as shown in Figure 5.5. In experiment, this is achieved by changing the voltage on the piezo element of the nano-positioner where the bottom DBR is attached. It is seen that the cavity modes can be tuned over a range of about 40 nm by gradually changing the cavity length. As shown in Figure 5.1(a) the cavity mode is not only present between the surface of the mirrors but penetrates into the DBRs. This penetration depth varies depending on the refractive index contrast of the two materials used to produce the DBR. The penetration is calculated using transfer-matrix simulations where the exponential decay of the electric field inside the DBRs is calculated. In our case this depth for each DBR is around 0.675 μm, therefore $L_{opt} = L_{cav} + 1.25\mu$m. Due to unavoidable debris on the surface during the transfer of the monolayers, the minimum cavity length that can be achieved in the experiment is between 2.3 and 4 μm. This means that the longitudinal mode measured is not the first fundamental mode. The separation between two longitudinal modes, q_k and q_{k+1}, ($k \in \mathbb{N}$) with $m = n = 0$, is:

$$L_{cav} = \frac{1}{2} \frac{1}{\frac{1}{\lambda_{q_{k+1,0,0}}} - \frac{1}{\lambda_{q_{k,0,0}}}}. \tag{5.2}$$

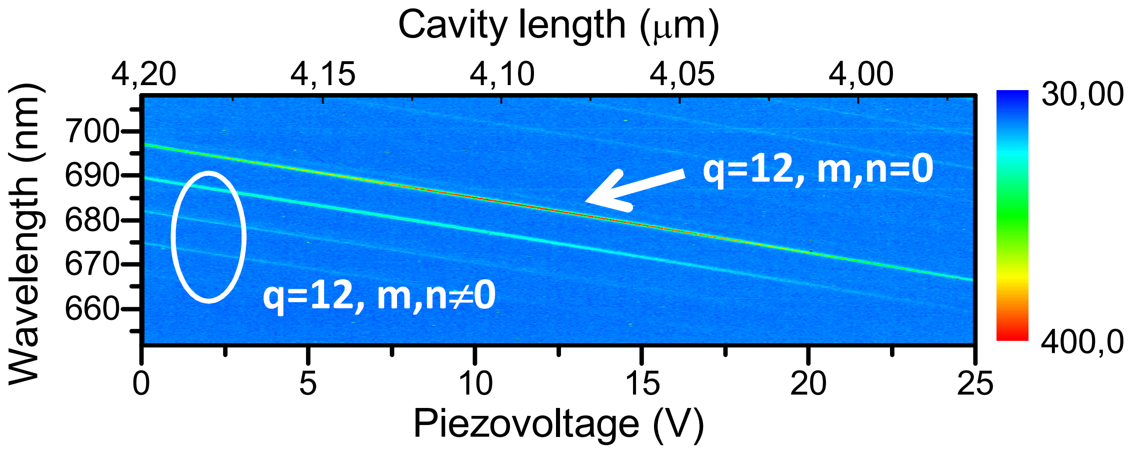

Figure 5.5: Tuning of the mode wavelength by adjusting the vertical length of the cavity. The distance between the DBRs is adjusted by changing the applied voltage on the piezo-nanopositioner. The figure shows PL map obtained for such length tuning for the cavity containing a monolayer MoS_2 film. PL of the modes is observed in a wide spectral range overlapping with the PL of the MoS_2 film: the mode PL is enhanced when in resonance with MoS_2 emission, showing weak coupling between the emitter and the cavity.

The bright peak marked in the plot corresponds to a fundamental longitudinal mode with q=12 for the optical cavity length of around L_{cav} = 4.2μm. Apart from this mode, several other transverse modes with $m, n \neq 0$ are also visible. The emission of the MoS_2 monolayer is centered at around 680 nm and the intensity of the cavity modes is enhanced when they are tuned past this spectral window. On the top right of the plot another set of transverse modes are visible, corresponding to the longitudinal mode with q=11, which would be tuned through resonance if the cavity length could be reduced further. In the experiment, however, the mirrors started to touch each other and tuning the cavity mode further was not possible.

5.2 Gallium Selenide

Using a similar pair of DBRs it is also possible to tune the modes around the emission wavelength of GaSe, down to $\approx$ 600 nm. Figure 5.6 shows PL for a 43 nm thick GaSe sheet. The emission consists of a neutral exciton centered at around 2.07 eV with a band

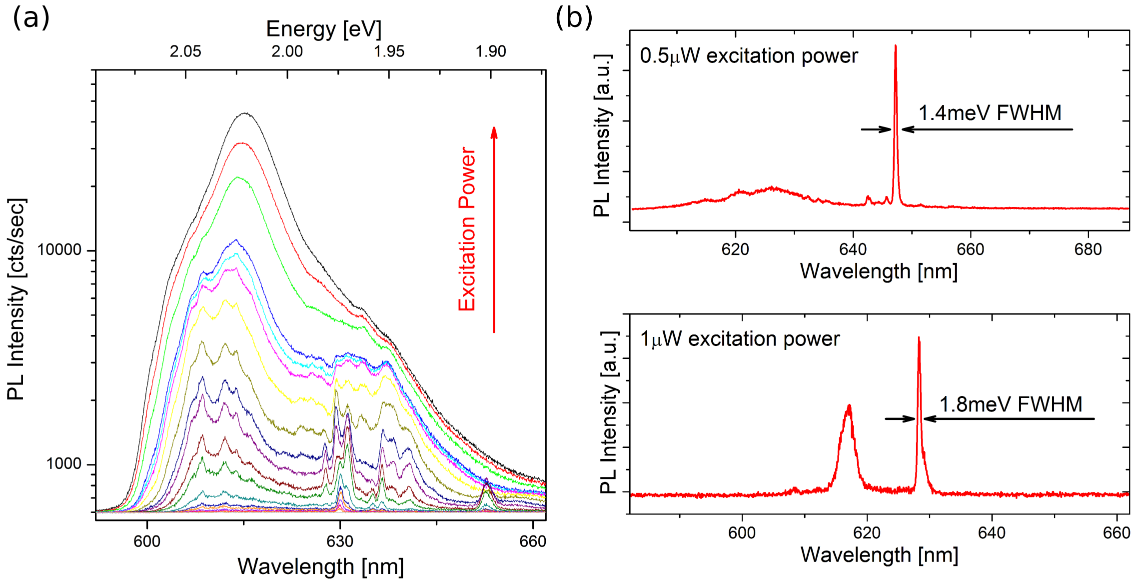

Figure 5.6: PL spectrum of a 43 nm thick GaSe sheet. (a) The spectrum consists of an exciton centered at around 605 nm and a broad shoulder attributed to defects. At low excitation power localized states are shown that emerge to a shoulder with increasing power. The power dependence is measured in the range from 1μW to 1mW excitation power. (b) The localized states can have narrow linewidth in the order of 1.4 - 1.8 meV.

consisting of localized states which occur from inter-layer stacking defects [120]. A power dependence shows that this shoulder is emerging from sharp, quantum-dot like states that saturate with increasing excitation power. At low excitation power isolated peaks with a linewidth as low as 1.4 meV are measured.

Time-resolved measurements in Figure 5.7 show the difference in PL lifetime for the exciton transition and the localized states. The trace in the colour plot shows that the emission at the wavelength of the exciton decays significantly faster than the emission of localized states. Extracting a slice for the exciton and localized states (lifetime 1 and lifetime 2 in the plot, respectively), reveals an exciton lifetime of 67 ps, which is dominated by non-radiative processes. The decay is fitted using a bi-exponential decay function, suggesting that the carrier relaxation consists of a fast and a slow decay component. This may be due to the observation of radiative and non-radiative lifetimes or localized states may be energetically close enough to the exciton line and the extracted decay is a composition of both. Further studies are required to fully understand the origin of this observation. The localized states show a long carrier lifetime up to the order of 1 ns. The measurements were taken through a 300 grating spectrometer with the slits opened in order to improve the temporal

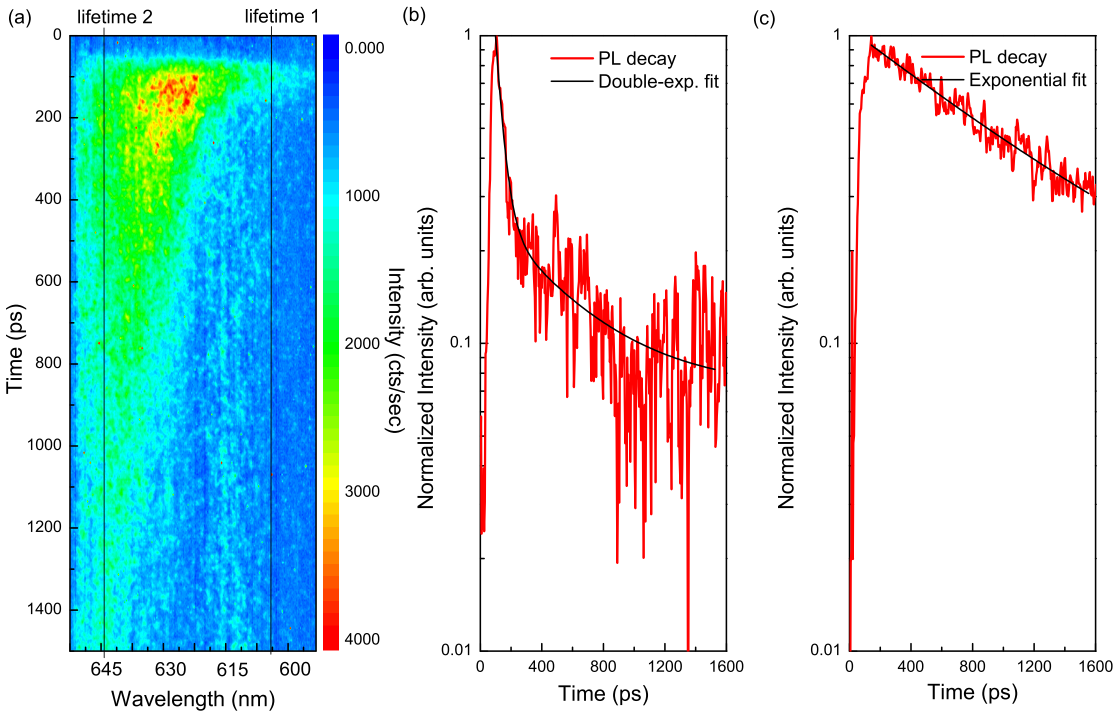

Figure 5.7: Time-resolved measurements of GaSe thin films. (a) The colour plot shows a trace of the PL decay highlighting the difference of the carrier lifetime for the exciton and the localized states. In order to extract the lifetimes, a slice for around 605 nm has been taken for the exciton (lifetime 1) and for around 645 nm for the localized states (lifetime 2). A mono-exponential fit reveals a lifetime of (b) 67 ps for the exciton and (c) 700 ps for the localized states.

resolution. The price for this is that the spectral resolution is poor. This does not affect this measurement, however, as localized states and exciton states are energetically separated far enough to still resolve them.

The PL emission is coupled to cavity modes where the broad PL is coupled to narrow cavity modes and a PL enhancement is observed as shown in Figure 5.8(a). In this case the cavity length is $L_{cav} \approx 4.2\ \mu$m and a concave mirror with a RoC of 25 μm is used. In this figure the observed Q-factor is as high as 3100, resulting in a linewidth of less than 1 meV. The highest Q-factor observed in this experiment is 7409 as shown in Figure 5.8(b). This mode has a wavelength $\lambda_{q,m,n} = 603.7$nm, and q=15 and m,n=0. The inset also shows the modes with q=14 and $m,n \neq 0$ observed in a broader spectral range. These measurements are carried out in a cavity with $L_{cav} = 3.25\mu$m and the radius of curvature of the top mirror RoC $= 25\mu$m.

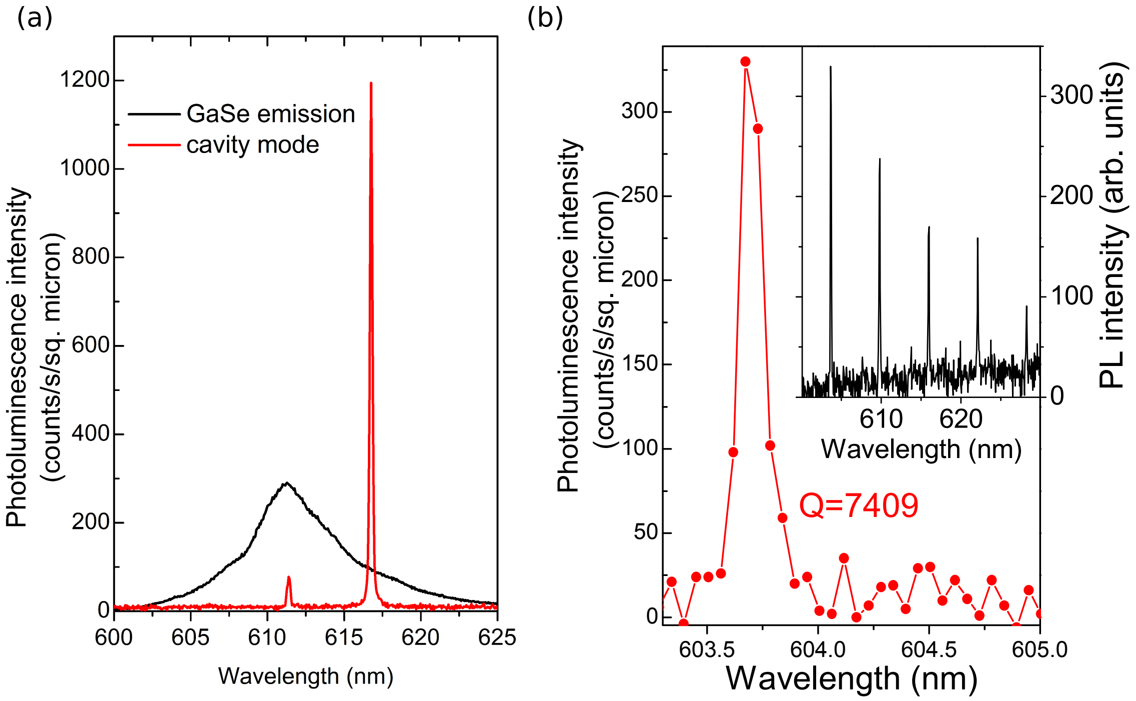

Figure 5.8: The broad PL emission of GaSe is coupled into narrow cavity modes. (a) The cavity mode is tuned to be in resonance with the localized states in this case. (b) PL spectrum measured in a microcavity containing a thin GaSe film (43 nm). A high Q-factor of around 7400 is observed for a longitudinal mode. The inset shows the same PL spectrum in a wide range of wavelength, where other modes with non-zero transverse mode numbers ($m, n \neq 0$) are observed.

5.3 Photoluminescence enhancement

The PL enhancement arises from a combination of angular redistribution of light emission and enhancement of the spontaneous emission rate (Purcell enhancement). Direct evidence for the Purcell enhancement is obtained from time-resolved PL measurements where a reduction of the radiative lifetime is observed. In order to study the angular redistribution numerical simulations have been performed using Finite-Difference Time-Domain (FDTD) simulations where the angular width of the fundamental cavity mode is calculated and compared with the radiation pattern for a dipole placed directly on the bottom DBR without the top mirror in the optical path. The observed PL enhancement is a combination of Purcell enhancement and angular redistribution of the emission pattern.

5.3.1 Geometric effect

The ratio of observed intensities for the structure with and without the top mirror depends to some extent on the collection optics since the angular distribution of emission for a given wavelength of light is different for the two cases. The objective lens which collects the light is 7.5mm above the sample. This is sufficiently far from the sample compared to the wavelength of light and to the experimentally measured spot sizes that it can be considered to be in the far field. The collection efficiency is then entirely determined by numerical aperture of the lens. The clear aperture of the objective is 4.5mm so only light emitted within ± 16.7 degrees is collected. When the top mirror is present a cavity is formed which confines electromagnetic modes at certain frequencies in all three dimensions. At these resonant frequencies the fields and hence the angular spread of the emission are determined by the cavity geometry. Simulations of the electromagnetic fields associated with the resonant cavity modes have been performed with the FDTD method, using a freely available software package, called *meep* [121]. The fields are first determined in the near-field zone close to the cavity. Simulations are performed in a cylindrical geometry on a two-dimensional grid of radial r and axial position z. This allowed much faster simulation times than a full three-dimensional calculation, which is necessary due to the rather small 10 nm grid resolution used to accurately represent the cavity layers and top mirror curvature.

Figure 5.9(a) shows a schematic of the dielectric profile used for the simulations. The lower DBR is the same as in the planar case discussed earlier. The upper DBR is of the same structure as the lower DBR with low index material adjacent to the cavity. In the radial range $0 \leq r \leq r_m$, where r_m is the mirror radius, the DBR structure is offset in the positive z-direction according to $z = z_0 + \sqrt{\mathrm{RoC}^2 - r^2} - \sqrt{\mathrm{RoC}^2 - r_m^2}$.

The separation between the upper and lower mirrors is first set to the experimentally estimated value and then refined in the following way. At the start of the simulation a broad frequency spectrum of electromagnetic radiation is excited by an electric dipole current source with short Gaussian temporal profile positioned on top of the lower DBR at $r = 400$nm. The electromagnetic energy flux passing through a box surrounding the structure, denoted by the dotted lines, is collected for a sufficiently long time to allow all the energy to leave the simulation region. The flux is Fourier transformed to obtain a spectrum of the radiation emitted by the structure. Such a spectrum is shown in Figure 5.9(b). The sharp peaks identify resonant cavity modes and correspond to modes with a range of longitudinal (z-direction) and transverse (radial) quantization numbers. To find the fundamental (zero transverse quantization number) mode the simulation is repeated a number of times using a narrow-band excitation centered on each cavity mode in the spectrum. The cavity modes have a high quality factor Q and so decay much more slowly than other transient fields caused by the excitation. After several decay-times of the chosen cavity mode the remaining electric and magnetic fields may be considered to have an approximately single-frequency harmonic time dependence and to represent the spatial dependence of the chosen cavity mode. Simulations are run for between one and three decay times $\tau = Q/\omega$ in order to reach this condition. After this the electric and magnetic fields at all points in the simulation volume are output. Figures 5.9(c-d) show the spatial profiles of the time-averaged electric intensity $E \cdot E^*$ for two of the modes in the spectrum corresponding to the longitudinal mode (c) and a mode with non-zero radial quantization number (d). The mirror separation is then adjusted slightly to bring the fundamental mode close to the experimental wavelength before the fundamental mode field profile is recalculated.

Figures 5.9(e-f) show the radial component of electric field as a function of position for

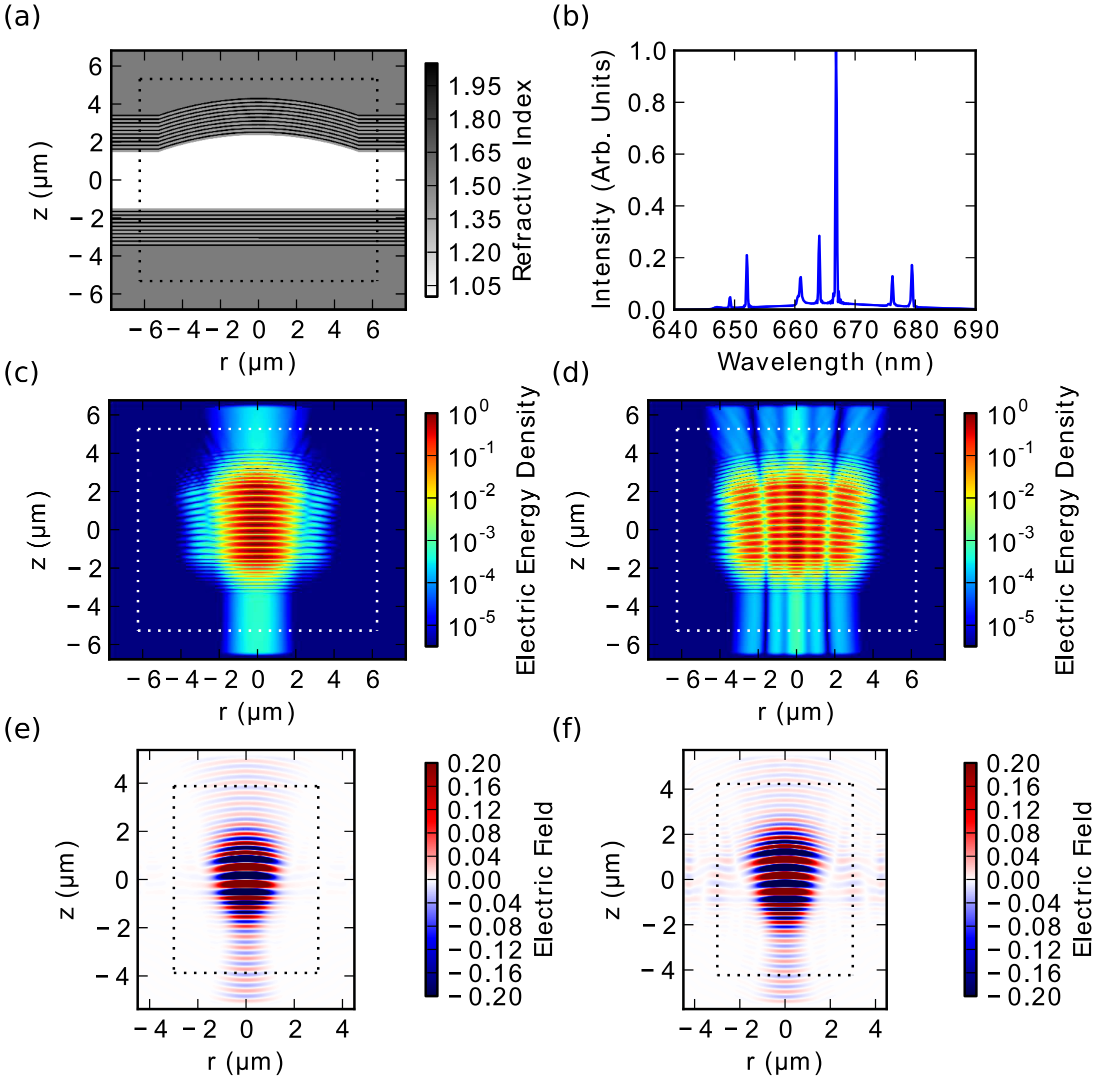

Figure 5.9: FDTD simulations of the open cavity. (a) Dielectric profile of cavity with 16μm radius of curvature mirror used in FDTD simulation. The dotted lines show the position of flux planes used to monitor the energy flux out of the structure. (b) Emission spectrum from the structure in (a) after excitation with a broadband source. (c,d) Electric density $E \cdot E^*$ for two modes in (b) on a logarithmic colour scale. (e,f) Radial electric field component on an exaggerated colour scale for 5.6μm radius of curvature cavities with mirror separations 1.12 and 1.82 respectively.

two different mirror separations, 1.1 μm and 1.8 μm, and 5.6 μm radii of curvature. For the larger mirror separation an increase in the field amplitude in the planar regions adjacent to the curved mirror and simultaneously the appearance of extra non-zero wavevector components in the angular spectrum of upwards propagating radiation is observed. These are accompanied by a drop in cavity quality factor from 5500 to 4700 and an increase in the proportion of energy flowing through the side flux planes. The quality factor and sideways energy loss get worse with further increases in mirror separation, see Table 5.1 structure C5. It has been shown experimentally that the quality-factor in hemispherical cavities increases with increasing mirror separation up to a critical value where it begins to decrease. This behaviour is attributed to a loss of mode stability which, in a purely geometrical picture, is where some rays at higher angles become able to exit the resonator on each round trip. Geometrical arguments predict that this occurs when the mirror separation is greater than the radius of curvature. However, these arguments ignore the finite diameter of the curved section of the mirror. In the real system there is a sharply discontinuous interface between curved and planar regions which may cause scattering with a strength which depends on the local field amplitude. Qualitatively, the angular spread of the mode is dictated by the radius of curvature. The spatial extent of the beam at the top mirror will be proportional to this angular spread and the mirror separation. When the separation is large the spatial beam size will overlap with the discontinuous region leading to scattering. It is likely that this scattering is the cause of the observed energy loss from the confined mode into sideways propagating modes and also of the complicated angular emission profile above the structure. The two effects together tend to reduce the fraction of power collected by the objective lens. As can be seen from Figure 5.9(c,e) the upwards radiation forms a beam centered about $r = 0$ which falls off to negligible intensity by the edge of the top flux plane. Comparing the fields above and below the structure it is shown that the curvature of the top mirror has a lensing effect which makes the beam propagating from the top of the sample spread more compared to that from the bottom. To obtain the relevant portion of the radiation pattern the total energy flux through the four flux planes is first examined and the fraction passing through the top compared to the total obtained. The field above the structure is then Fourier transformed to determine the spread of upwards power among waves propagating with different in-plane wavevectors and hence at different angles. Finally, these are integrated in the same manner discussed above for the case without top mirror. The input parameters and simulation results are summarised in table 5.1.

Table 5.1: Simulation parameters and results for microcavity structures. The parameters and results of the simulations with different RoC and different cavity length are listed. The parameters are chosen so that the cavity mode is in resonance with the MoS_2 emission. The obtained Q-factors range from 11000 to 1900 and the collection efficiency is ranging from 47% to as low as only 6% when the cavity length is approaching the stability limit.

Cavity	RoC (μm)	L_{cav} (μm)	λ_c (nm)	Q-Factor	Collected Power (%)
C1	16	2.98	679.8	11000	47
C2	10	2.05	681.1	7700	44
C3	5.6	1.82	678.9	4700	20
C4	5.6	1.12	678.1	5500	31
C5	5.6	2.52	679.9	1900	6

In order to calculate the angular distribution of the emission, the radiation pattern without the top mirror is considered at first. The bottom DBR mirror is modelled as a lossless dielectric multilayer consisting of 10 repeats of materials with refractive indexes 1.4 and 2.05 and thicknesses 116.07 nm and 79.27 nm respectively. The low index material faces the collection lens with the emitters positioned at zero separation from it. The bottom of the DBR rests on a semi-infinite glass substrate with refractive index 1.54. The coordinate axes are chosen so that the layer planes are perpendicular to the z-axis. The emission from the sample may be modelled by an incoherent ensemble of classical electric point dipole current sources. Since the excitons in monolayer sheets are two-dimensional it is assumed that the emitters are oriented randomly in the plane of the monolayer material. To model the random distribution of in-plane polarisations one may take the incoherent sum of the radiation patterns due to any two orthogonally polarised in-plane dipoles. The resulting total radiation pattern must then have circular symmetry about the z axis since there is no preferred azimuthal direction. As the spot size is small it is sufficient to treat only dipoles positioned at the origin $r = 0$ as the radial position will have little effect on the angular spread of the emission. Calculations are performed for dipoles radiating at a frequency corresponding to a wavelength of 680 nm in free space, as in the experiment. The electric field due to a point electric dipole current radiating in free space may be expanded in a basis of plane-waves. In the presence of the mirror the total upwards-radiating field (towards the collection lens) is the coherent sum of the radiation field emitted upwards by the dipole and the reflection from the mirror of the field emitted downwards by the dipole. The free-space fields are separated into components with TE and TM polarisation with respect to the planar multilayer and the amplitude reflection coefficients are calculated using a transfer matrix technique. Figure 5.10 shows the sum of radiation patterns due to x and y polarised dipoles for the case of dipoles in free space and directly on top of the DBR. For zero angle the DBR reflective phase is close to zero so the reflection reinforces the upward propagating wave and the upwards emission is enhanced with respect to free space. At larger angles the reflective phase increases so that the reflection begins to interfere destructively with the directly radiated field. For angles greater than 90 degrees the radiation is into the substrate. Very little power is radiated into modes close to 180 degrees because the DBR reflects them. For angles greater than 20 degrees from the negative z-axis, however, the DBR becomes ineffective and light is lost into the substrate. To obtain total power radiated in the range of polar angles $0 \leq \theta \leq \theta_{max}$ the radiation patterns must be integrated with azimuthal and polar collection angles according to $P(\theta_{max}) = \int_0^{2\pi} \int_0^{\theta_{max}} p(\theta,\phi) sin(\theta) d\theta d\phi$ where $sin(\theta) d\theta d\phi$ is the differential element of solid angle. Overall, 49% of the total radiation is emitted in the upwards direction and 9% is emitted within ±16.7 degrees. This compares to only 3% emitted within ±16.7 degrees for dipoles in free space.

To calculate the fraction of the collected light it is necessary to know the power radiated per unit solid angle as a function of observation angle in the far field, the so-called radiation patterns. Then the power emitted within the collection range of the lens may be compared with the total emitted power. The simulated power radiated per unit solid angle in the far field is shown in Figure 5.11 for the different RoC used in the experiment as well as the experiment without top mirror. Only the upward flux is shown although the total flux radiated in all directions is calculated. For the simulation of the cavities with a RoC of 16, 10 and 5.6 μm a physical cavity length of L_{cav} = 2.98, 2.05 and 1.82 μm have been used, respectively. These parameters match with the experiment and are slightly adjusted to ensure that the longitudinal mode is in resonance with the exciton transition of MoS_2. The parameters are summarised in table 5.1.

In Figure 5.11 it is observed that in the case of no top mirror present, the PL is emitted in a broad range of angles, whereas markedly more directional distributions are observed for the three cavities. It can be estimated that for the light to be collected by the objective placed above the microcavity, light should be emitted within a 16.7^o cone. Conse-

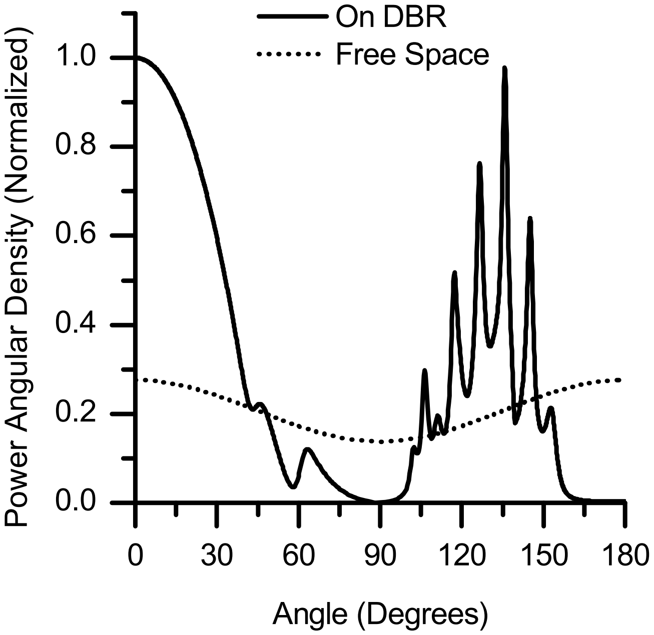

Figure 5.10: Dependence of emitted power per unit solid angle on observation angle. The emitted power is simulated for randomly oriented dipoles in the x-y plane on the DBR and in free space. Both curves have been normalised to the peak value for dipoles on the DBR.

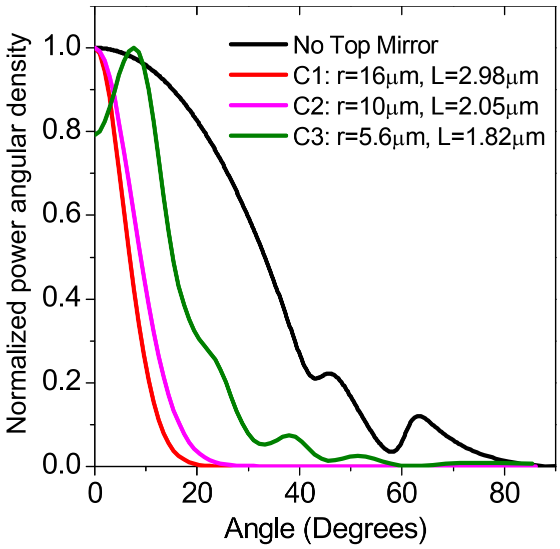

Figure 5.11: Calculated angular distribution of light emission from a 2D film with and without the cavity. The plot shows the normalized power angular density for a dipole sitting on a flat DBR without the top mirror and for the three different cavities, C1, C2 and C3 with different radii of curvature and cavity length. In the case where no top mirror is present light emission has a very broad angular spread. The cavity modes are much more directional.

quently, in the case where no top mirror is present only 9% of the total power is collected through the objective. On the other hand, for the cavities C1, C2 and C3, the fractions of power within ±16.7 degrees are 47%, 44% and 20% respectively. The marked lowering for the cavity with the smallest RoC occurs because of scattering at the discontinuity between curved and planar regions of the top mirror. Note, that in the real cavity structures this effect may not be as pronounced, as this discontinuity may be less sharp than in the model. Thus, in cavities C1, C2 and C3, 'geometrical' PL enhancements with factors, F_g of 5.3, 4.9 and 2.2 respectively occur compared to the case when no top mirror is present.

Finally, the fractions of total emitted power collected by the objective may be compared between the cavities and the case where there is no mirror. For the cavities close to the experimental parameters C1 and C3 it is expected to collect 5.3 and 2.2 times more of the total emission than in the case with no top mirror. This agrees with the qualitative notion that the larger cavity should give a more directional beam and so more of the emission should be collected.

5.3.2 Purcell enhancement

Further to the angular distribution, the FDTD method employed above can be used to calculate the Purcell enhancement factors, F_P, using the calculated values for the mode volume, V, and the Q-factor, Q. The following Purcell factors are obtained for the three considered cavities: F_{P1}=41, F_{P2}=59 and F_{P3}=70. For the time-resolved measurements discussed below a Purcell factor of F_P=51 is calculated with parameters for the cavity, $L_{cav}\approx 2.9\mu$m and R_c=10μm. These values for F_P are for the emitter in perfect spatial and spectral overlap with the cavity mode and therefore these values of F_P provide an upper limit to the Purcell factor achievable in a cavity. In the experiment, there is an inhomogeneously broadened ensemble of spectrally narrow emitters distributed in a few μm diameter area of a 2D film. This means that spatial and spectral averaging of the Purcell enhancement will occur and a value of F_P lower than given above is expected. The enhancement of the spontaneous emission rate of an emitter at position $\mathbf{r}_0$ due to a cavity may be calculated using the standard equation as explained in equation 3.28:

$$F_P(\mathbf{r}_0) = \frac{3}{4\pi^2}\left(\frac{\lambda}{n(\mathbf{r}_0)}\right)^3\left(\frac{Q}{V_{eff}}\right). \tag{5.3}$$

Here λ is the vacuum wavelength, $\mathbf{r}_0$ is the position of the field maximum in the cavity and n is refractive index. The effective mode volume is given by:

$$V_{eff} = \frac{\int_{-\infty}^{\infty}\int_0^{2\pi}\int_0^{\infty}\varepsilon(\mathbf{r})\left|\mathbf{E}(\mathbf{r})\right|^2\cdot r\cdot dr d\phi dz}{\varepsilon(\mathbf{r}_0)\left|\mathbf{E}(\mathbf{r_0})\right|^2}, \tag{5.4}$$

where $\mathbf{r} = (r,\phi,z)$ is the position in space and $\varepsilon(\mathbf{r})\left|\mathbf{E}(\mathbf{r})\right|^2 = \varepsilon(\mathbf{r})\left(\mathbf{E}(\mathbf{r})\cdot\mathbf{E}^*(\mathbf{r})\right)$ is the electric energy density. Since the full electromagnetic fields of the cavity modes are calculated as a function of position by the FDTD simulations the effective mode volumes are obtained simply by numerically performing the integral in equation 5.4. Mode volumes of 6.46, 3.10 and 1.61 μm^3 are obtained for the cavities C1, C2 and C3 respectively. The FDTD calculations also give central wavelengths and Q-factors for the modes. These are obtained by examining the field in the cavity using a harmonic inversion technique. For the cavities C1, C2 and C3 Q-factors of Q_1=11000, Q_2=7700 and

Q_3=4700 are obtained, respectively, which lead to Purcell factors of F_{P1}=40.7, F_{P2}=59.4 and F_{P3}=69.8.

These Purcell factors provide an upper limit to the enhancement which may be achieved in a cavity. The actual ratio of spontaneous emission rates observed in an experiment will depend on the spectral and spatial overlap of the emitter with the optical mode which effect the local density of states and magnitude of the vacuum field respectively. Accurate modeling of the experimentally observed cw PL enhancement and lifetime shortening in time-resolved measurements also requires the knowledge of the non-radiative decay rates in the 2D film.

5.3.3 Experimental demonstration of Purcell enhancement

The observed PL lifetime, τ_{PL}, in time-resolved experiments is a combination of radiative τ_r and non-radiative lifetime τ_{nr}. As shown above, the enhancement of the spontaneous emission rate is described with the Purcell coefficient F_P according to equation 3.28. The observed lifetime is then written as:

$$\frac{1}{\tau_{PL}} = \frac{1}{\tau_{nr}} + \frac{F_P}{\tau_r}. \tag{5.5}$$

$F_P = 1$ for the PL emission without the effect of the cavity while $F_P > 1$ is expected for emitters in resonance with the cavity mode. In this approximation non-linear effects like state-filling effects are neglected. Time-resolved measurements of monolayer MoS_2 reveal a carrier lifetime of 10 ps, which is close to the resolution limit of the streak camera, as shown in Figure 5.12.

This lifetime is dominated by non-radiative processes, which also explains the low emission efficiency in this material. In this case, even for relatively large Purcell enhancement, no reduction of the carrier lifetime is expected since for $\tau_{nr} << \frac{\tau_r}{F_P}$:

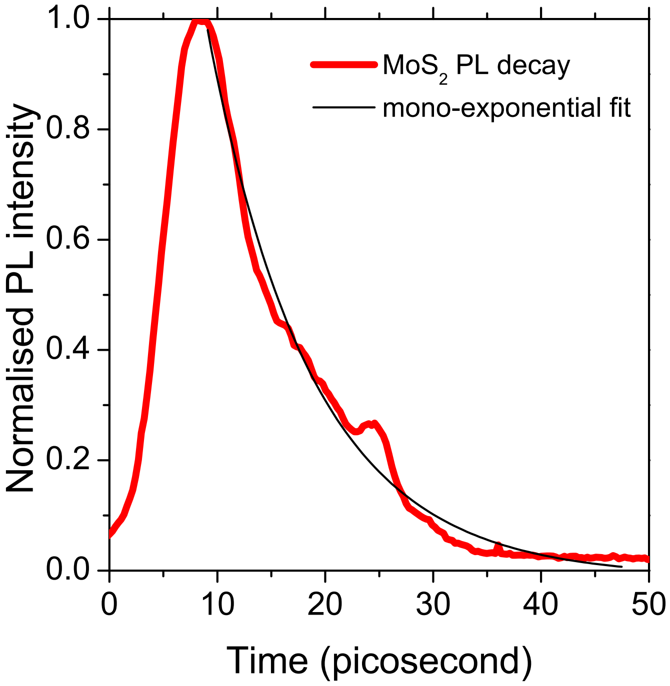

Figure 5.12: Carrier lifetime of MoS$_2$ monolayer sheets. Time-resolved measurements of MoS$_2$ monolayer sheets show a carrier lifetime of only around 10 ps, dominated by non-radiative processes.

$$\frac{1}{\tau_{PL}} = \frac{1}{\tau_{nr}} + \frac{F_P}{\tau_r} \approx \frac{1}{\tau_{nr}}. \tag{5.6}$$

Therefore, no PL lifetime reduction is expected in the case of MoS$_2$. The enhanced spontaneous emission rate, however, also leads to an alteration of the observed PL intensity which can be derived as:

$$I_{PL} \propto \frac{\tau_{nr}}{\tau_{nr} + \frac{\tau_r}{F_P}}. \tag{5.7}$$

In case of MoS$_2$, where $\tau_{nr} << \frac{\tau_r}{F_P}$, equation 5.7 can be simplified to:

$$I_{PL} \propto \frac{\tau_{nr}}{\tau_{nr} + \frac{\tau_r}{F_P}} \approx \frac{F_P}{\tau_r}. \tag{5.8}$$

This shows that the PL enhancement is directly proportional to the Purcell factor F_P. To estimate the Purcell enhancement through the PL intensity, however, also the geometric effect described in the previous section has to be included. The total PL intensity enhancement is calculated by $I_{PL} \propto F_P F_G$, where F_G describes the increase of the collected emission purely through the redistribution of the emission. In the calculations above the maximum expected enhancement caused by this effect is $F_G \approx 5$. The comparison between the bare PL emission and the cavity modes in Figure 5.4 shows a PL enhancement of 10, 30 and 60, dividing this enhancement by the geometric enhancement allows an estimation of the Purcell enhancement for MoS_2 with $F_P \approx 2$ to $F_P \approx 12$ for the different radii of curvature.

In case of GaSe the localized states show a significantly longer carrier lifetime. In this case the radiative and non-radiative lifetime is comparable and a Purcell enhancement can be directly observed by comparing the radiative lifetimes with and without the effect of the cavity. Figure 5.13 shows PL decay curves for a 43 nm GaSe film excited at 415 nm with a pulsed laser. In both half- and full-cavity configurations the time-averaged excitation density is 2.6kW/cm^2. The cavity length is adjusted to $L_{cav} \approx 2.9\mu$m and a concave mirror with a RoC of 10 μm is used for this experiment. The cavity length is set so that a longitudinal cavity mode is coupled into the low energy shoulder of the GaSe emission at 613 nm. As seen in Figure 5.13(a), without the effect of the cavity, PL decay with a lifetime of $\tau_{hc} \approx 700$ ps is observed, whereas in the full-cavity configuration $\tau_{fc} \approx 70$ ps resulting in a Purcell enhancement of 10. Both times are obtained by fitting the decay using a mono-exponential decay function. This measurement signifies the enhancement of the spontaneous emission rate in the tunable cavity device.

Figure 5.13(b) presents further evidence for the enhancement of the radiative recombination rate in a microcavity where a PL power-dependences of the 43 nm thick GaSe film in the half- and full-cavity configurations measured with a 532 nm cw laser is shown. For the full cavity the same L_{cav} and RoC is used as for the time-resolved experiments. The plot shows integrated PL intensity calculated under the full-cavity mode spectrum centered at 613 nm and having a FWHM of 0.15 nm, and under the same bandwidth of GaSe PL at the same center wavelength in the half-cavity case. As shown in Figure 5.1(b) the wavelength of the excitation laser is outside the stopband and $\sim$30% of the laser is reflected on the DBR. The reduced transmission of the green laser through the top DBR is taken into ac-

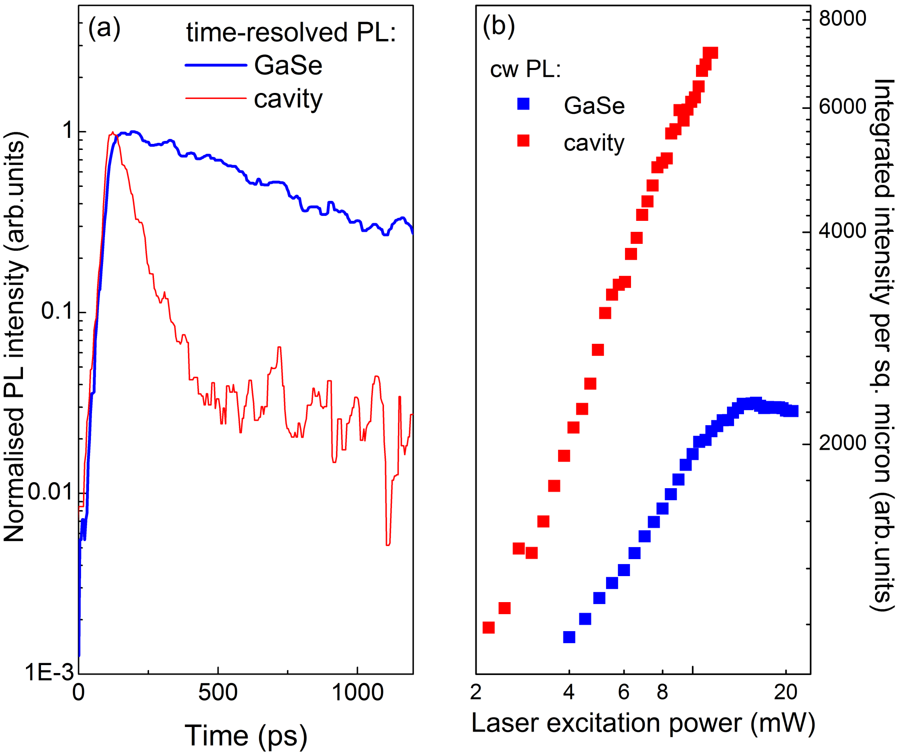

Figure 5.13: Observation of Purcell enhancement for GaSe thin film emission in a tunable microcavity. (a) Time-resolved PL emission is collected for a wavelength of 613nm. PL is measured at $T = 4.2$K using excitation with a pulsed laser at 415 nm. The blue trace shows GaSe PL decay in a film in the half-cavity configuration with a lifetime of 700 ps. The red curve is for the cavity PL decay, for which a lifetime of 70 ps is extracted. (b) State-filling effects are observed under cw pulsed excitation using a 532nm laser in the case of the half-cavity configuration (blue dots). For the full-cavity configuration (red dots) the spontaneous emission rate is enhanced so that carriers relax quicker and can be filled again by pumping higher. Therefore no saturation in PL is observed. Note, in the power dependence presented earlier the saturation has no been observed, as the power was not increased above 1mW in that graph.

count, and the data are plotted as functions of the actual laser power incident on the GaSe film. In the case of the half-cavity configuration, a clear sub-linear PL intensity growth with power is seen. PL saturation is observed at around P=10 mW, indicating that the optical pumping rate exceeds the relatively low recombination rate of the localized exciton states in GaSe, $1/\tau_{hc}$ with $\tau_{hc} \approx$700 ps [122]. This saturation effect is a state-filling effect, which has been observed previously in semiconductor quantum dots [123]. In contrast to this, a much stronger PL increase with power is found for the cavity mode in the full-cavity configuration. No PL saturation is observed, indicating that the spontaneous recombination rate remains higher than the excitation rate in the whole range of powers used. This striking difference clearly indicates that the carrier radiative lifetime is markedly shorter in the case when the full cavity is formed, the effect quantified with the 10-fold PL decay time shortening in Figure 5.13(a).

5.4 Summary

The PL emission of monolayer MoS_2 and few-layer GaSe sheets are coupled to narrow cavity modes using a tunable open-access microcavity setup. By adjusting the separation of the two DBRs the cavity mode is tuned in resonance to the exciton energy, as well as the energy of localized states in GaSe sheets. Direct evidence for the Purcell enhancement is obtained for the GaSe film in Figure 5.13. It can be shown that the ratio of $\approx$10 of the experimentally measured τ_{PL} values in the half- and full-cavity configurations corresponds to the lower limit for the Purcell enhancement factor which is reached if $\tau_{nr} \gg \tau_r$. For cavities investigated in both the time-resolved and cw measurements, the calculated maximum Purcell enhancements in the range of 41 to 70, as found in the previous subsection, exceed those observed in the experiment. One of the reasons for this discrepancy is the lowering of the measured Q-factors from their calculated values occurring as a result of cavity imperfections. In this work the calculated Q-factors are $\approx$2.5 times larger than the measured values. Furthermore, in order to reflect the finite in-plane size of the mode and varied coupling to the mode of independent emitters at different wavelengths, spatially and spectrally averaged Purcell enhancement should be calculated. In general the averaged Purcell factors are lower than the maximum values for the perfect spatial and spectral emitter-mode overlap. The averaging procedure requires summation of I_{PL} in the case of cw PL enhancement or of the simulated PL decay curves in the case of lifetime shortening over the emitters in the ensemble. The total PL or average characteristic PL decay time may then be determined. However, the result is sensitive to the ratio $(\tau_r/F_P)/\tau_{nr}$ since both τ_{PL} and I_{PL} depend on these parameters. At this stage, insufficient information exists about the non-radiative decay processes in 2D films for such averaging to be carried out accurately.

This work opens a route to a wide range of devices using 2D films as optically active materials and which are also fully compatible with various van der Waals heterostructures. This will lead to realization of cavity-enhanced and tunable light-emitting diodes. An advantage such devices would offer compared to traditional semiconductors is compatibility with a wide range of substrate materials including various dielectrics, polymers and flexible substrates. This would permit a wide choice of materials for the fabrication of microcavities and waveguides.

6 Strong exciton-photon coupling of van der Waals heterostructures

In the previous chapter the weak coupling regime has been demonstrated with MoS_2 and GaSe. In this chapter another interesting TMDC, $MoSe_2$, has been studied. To extend this work van der Waals (VDW) heterostructures consisting of $MoSe_2$ and hBN have been fabricated and incorporated into optical microcavities in order to control and modify the light-matter interaction [124, 125]. Due to the large exciton binding energy of TMDCs, they are a promising candidates to observe the strong exciton-photon coupling regime [126]. Similar to the schematic shown previously in chapter 5, Figure 6.1(a) shows the design of the open-access microcavity. A schematic of the heterostructure used in this experiment is shown in Figure 6.1(b) and consists of a 3 nm thick film of hBN on which a monolayer of $MoSe_2$ is transferred. This forms a single quantum well (QW), highlighted with the blue dashed line on the right in Figure 6.1(c). On part of the $MoSe_2$ film sits another 3 nm thick film of hBN. Finally, a second monolayer sheet of $MoSe_2$ is sitting on top of this hBN layer in order to form a double QW, highlighted with the red dashed line. The PL emission of $MoSe_2$ at 4.2 K is shown in Figure 6.1(d). The black dashed line indicates an area of a bilayer $MoSe_2$ which has also been studied within this experiment.

6.1 Optical properties of molybdenum diselenide

In general it is found that TMDC selenides (WSe_2 and $MoSe_2$) outperform their sulphide counterparts in terms of emission efficiency and PL linewidth. The complex structure

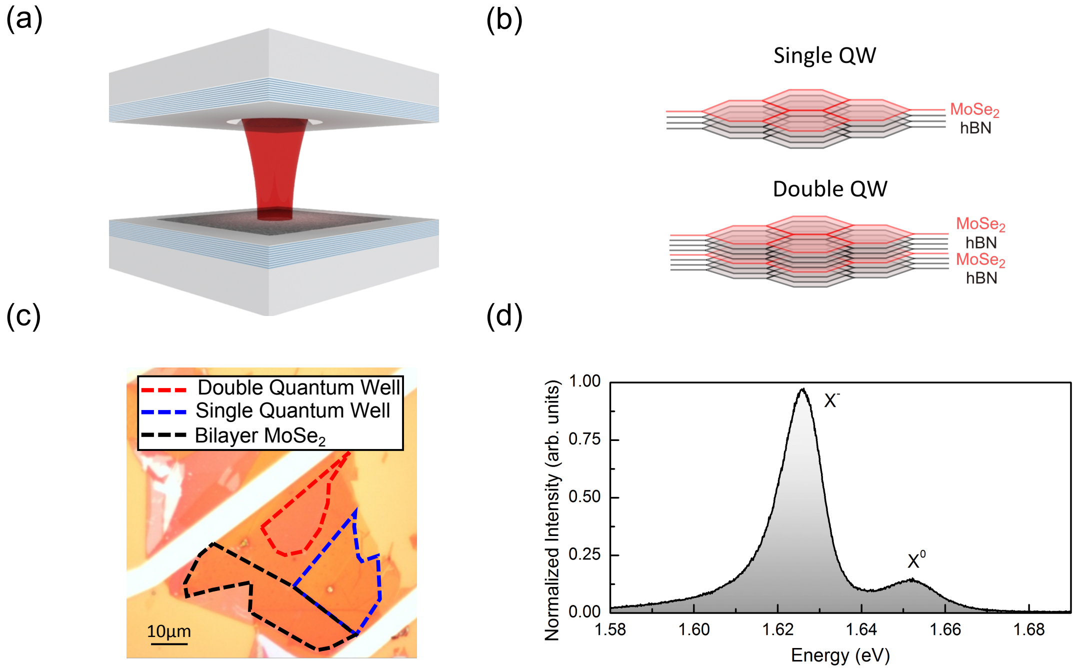

Figure 6.1: Schematic of the tunable microcavity with an embedded $MoSe_2$ heterostructure. (a) The schematic of the open cavity setup is shown as a reminder of the cavity structure where a (b) single and double QW heterostructure is placed on the planar mirror. (c) Optical image of the $MoSe_2$ heterostructure where the single and double QW areas are marked by the blue and red dashed lines respectively. A bilayer region is marked by the black dashed line. (d) The PL emission of $MoSe_2$, as measured in the open cavity setup at 4.2 K, shows the neutral and charged exciton, X^0 and X^- respectively.

of PL from a monolayer sheet of WSe_2 has been shown in Figure 7.2. A PL spectrum of $MoSe_2$, measured at around 10 - 20 K, is shown in Figure 6.2(a) where a neutral and a negatively charged trion, separated by 30 meV, are observed. Time-resolved measurements of the PL are shown in Figure 6.2(b) revealing a lifetime of 5 ps for X^0 and 12 ps for X^-, consistent with those reported previously [81] and are dominated by non-radiative processes.

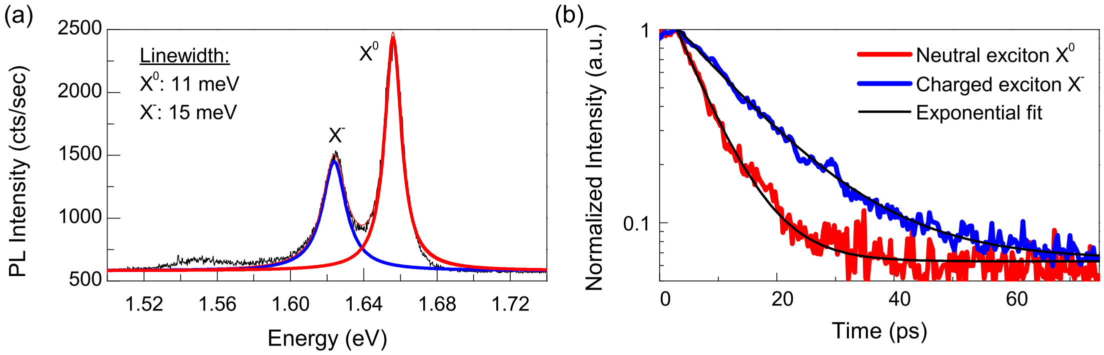

Figure 6.2: Time-resolved measurements with $MoSe_2$. (a) Time-integrated PL spectrum of monolayer $MoSe_2$ showing neutral and charged exciton, separated by 30 meV, with a linewidth of 11 meV and 15 meV. (b) Exponential decay for X^0 and X^- revealing a carrier lifetime of 5 ps and 12 ps respectively.

The linewidths of the neutral and charged exciton is 11 meV and 15 meV, respectively, highlighting the striking improvement over the PL observed in MoS_2. $MoSe_2$, therefore, appears to be a promising candidate for the observation of strong exciton-photon coupling where exciton-polaritons can be resolved. The study of exciton-polaritons has revealed a wealth of rich phenomena such as Bose-Einstein condensation in the solid state [58], polariton superfluidity [63], as well as room temperature polariton lasing in the UV and blue spectral regions using wide band gap materials such as GaN [127] and ZnO [128, 129] or organic materials [130–132]. The integration of TMDC heterostructures in optical microcavities is an attractive alternative to previously studied systems. TMDCs exhibit very large exciton binding energies and sharp exciton resonances, whose properties can be tailored by combining a wide variety of 2D crystals in heterostructures. Observation of room temperature excitons in TMDCs combined with the recently demonstrated good electroluminescence of VDW heterostructures [55] lays the foundation for the development of low threshold electrically pumped polariton lasers operating in the visible and near infrared. These devices can be easily incorporated onto a wide range of substrates allowing the development of hybrid TMDC/III-V microcavity structures as well as electrically driven polariton devices with vertical current injection using graphene contacts.

6.2 Estimation of the Rabi splitting

In order to estimate the expected vacuum Rabi splitting in MoSe$_2$ a simple model is used. Coupling a photonic open cavity mode to an exciton level is characterized by the Rabi frequency [133]:

$$\Omega_{Rabi} = 2\sqrt{\frac{2\Gamma_0 c}{n_c(L_{DBR}+L_c)}}, \tag{6.1}$$

where n_c is the cavity refractive index, which is close to unity in the open cavity system, L_{DBR} and L_c are the effective mirror and cavity length length respectively. $\Gamma_0 = 1/2\tau$ is the exciton radiative broadening given by [134]:

$$\Gamma_0 = \frac{2\pi e^2 |p_{cv}|^2}{nc\hbar\omega_0 m_e^2}\phi(\rho)^2, \tag{6.2}$$

where e is the electron charge absolute value, p_{cv} is the matrix element of the momentum between electron Bloch functions at valence and conduction band edges, $n \approx 2.2$ is the refractive index of MoSe$_2$, c is the speed of light, $\hbar\omega_0$ is the cavity mode energy, m_e is the free electron mass and $\phi(\rho)$ is the internal motion part of the 2D exciton wavefunction. For the 1s exciton state one can write:

$$\phi(0) = \sqrt{\frac{2}{\pi a_B^2}} = \sqrt{\frac{2\mu E_b}{\pi\hbar^2}}, \tag{6.3}$$

with a_B the 2D Bohr radius, $E_b \approx 0.55$ eV the exciton binding energy and $\mu = m_e \frac{m_c^* m_v^*}{m_c^* + m_v^*}$ the exciton reduced mass.

The matrix element p_{cv} may be deduced from the electron effective mass expression given by the $k \cdot p$ method:

$$m_c^* = \frac{m_c}{m_e} = \left(1 + \frac{2|p_{cv}|^2}{E_g m_e}\right)^{-1}, \tag{6.4}$$

where $E_g \approx 2.1$ eV is the band gap. Conduction and valence band effective masses are calculated ab initio for MoSe$_2$ and are given by $m^*_{c(v)} = 0.70(0.55)$ [135]. In general, the calculated effective masses at the K-points decrease as the material is thinned towards monolayer sheets. Experimentally it has been shown that the binding energy for X$^+$ and X$^-$ in MoSe$_2$ are similar, which suggests that the effective mass for electrons and holes are similar in MoSe$_2$ [152]. From this it follows:

$$|p_{cv}| = \sqrt{\frac{E_g m_e}{2}\left(\frac{1}{m_c^*} - 1\right)}. \tag{6.5}$$

Substituting equations 6.2 and 6.5 in equation 6.1 and assuming no detuning between exciton energy and photonic mode ($\hbar\omega_0 = E_g - E_b$) a Rabi splitting is obtained:

$$\hbar\Omega_{Rabi} = 8\sqrt{\frac{m_v^*\left(1 - m_c^*\right)}{2n\left(m_c^* + m_v^*\right)}\frac{E_g E_b}{E_g - E_b}\frac{e^2}{L_{DBR} + L_c}}. \tag{6.6}$$

With the absolute effective cavity length $L_{DBR} + L_c = 2.3$ μm , the obtained Rabi splitting is $\hbar\Omega_{Rabi} \approx 26.7$ meV.

6.3 Demonstration of strong exciton-photon coupling

The open cavity system allows spatial xyz-positioning of the two mirrors independently. As such, any area of the MoSe$_2$ heterostructure on the planar DBR can be placed in the optical path and a microcavity formed with the selected area as the active region. The micron sized

Gaussian beam waist on the planar mirror of the formed cavity allows each region of the $MoSe_2$ heterostructure to be coupled to the cavity modes independently. Figure 6.3 shows a PL scan of a cavity formed with a concave mirror with a radius of curvature of 20 µm and a single monolayer $MoSe_2$ active region. The various modes present in the spectra arise from the three-dimensional confinement of the photonic field which gives rise to longitudinal modes and their associated higher order transverse modes. These cavity modes are tuned through the neutral exciton resonance by reducing the mirror separation by applying a DC voltage to the bottom z-nanopositioner. The longitudinal resonance, labelled TEM_{00}, is at an energy of 1.588 eV at $V = 0$ and the modes at higher energy are its associated first (1.608 eV) and second (1.628 eV) transverse modes. The total optical cavity length is around 2.3 µm and the longitudinal mode number $q = 5$. The modes at lower energy than the longitudinal mode are transverse modes associated with a different longitudinal mode at much lower energy $(q-1)$. These are present since the mirror separation is larger than the separation of $\lambda/2$ required to reach the fundamental longitudinal resonance $(q = 1)$. Clear anticrossings between the cavity mode resonances and the neutral exciton energy are observed revealing the formation of well-resolved polariton states. Each photonic mode is characterized by a specific field distribution in the plane of the TMDC layers and couples to an excitonic mode with the same in-plane distribution. As a result, different photonic modes couple to spatially orthogonal exciton states. Polariton states from different photon modes are therefore orthogonal and are well described by the coupling between a single photon mode and a single excitonic mode for each of them.

When the dispersions for lower and upper polariton branches (equations 3.37 and 3.36) are diagonalized and the imaginary part is neglected, it reduces to a two-level problem. The two-level coupled oscillator model is then written as:

$$M(k) = \begin{pmatrix} E_{X^0}(k) & \frac{\hbar\Omega_{Rabi}}{2} \\ \frac{\hbar\Omega_{Rabi}}{2} & E_{ph}(k) \end{pmatrix}, \tag{6.7}$$

where E_{X^0} and E_{ph} is the energy of the neutral exciton and the cavity mode and $\hbar\Omega_{Rabi}$ is the vacuum Rabi splitting. The two-level coupled oscillator model is used to fit the upper and lower polariton branches (UPB and LPB) peak energies for the longitudinal mode, shown by the dashed lines in Figure 6.4(a), and reveals a Rabi splitting of $\hbar\Omega_{Rabi} = 20$ meV for a single $MoSe_2$ monolayer. Here the cavity mode energy is approximated as a linear function

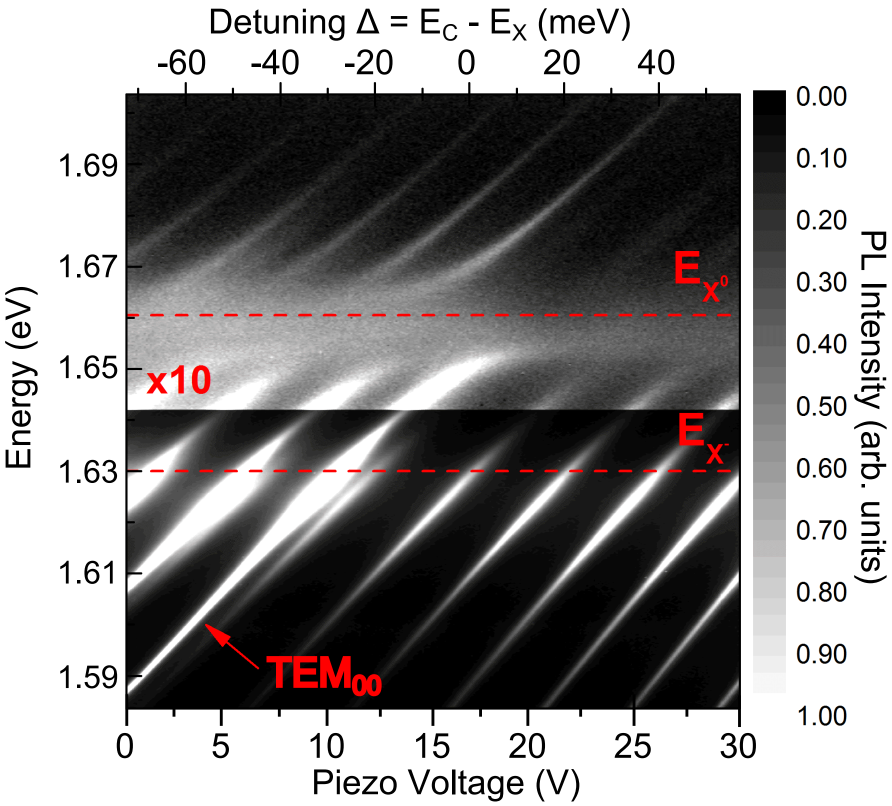

Figure 6.3: Observation of strong exciton-photon coupling in a MoSe$_2$ single QW heterostructure. A clear anticrossing in PL is observed between the discrete cavity mode energies and the neutral exciton energy at 4 K. The longitudinal mode is marked as TEM$_{00}$ and corresponds to the q=5 mode with its corresponding higher order modes appearing on the lefthand side of the mode (higher energy). The higher order modes observed at lower energy corresponds to the next longitudinal mode.

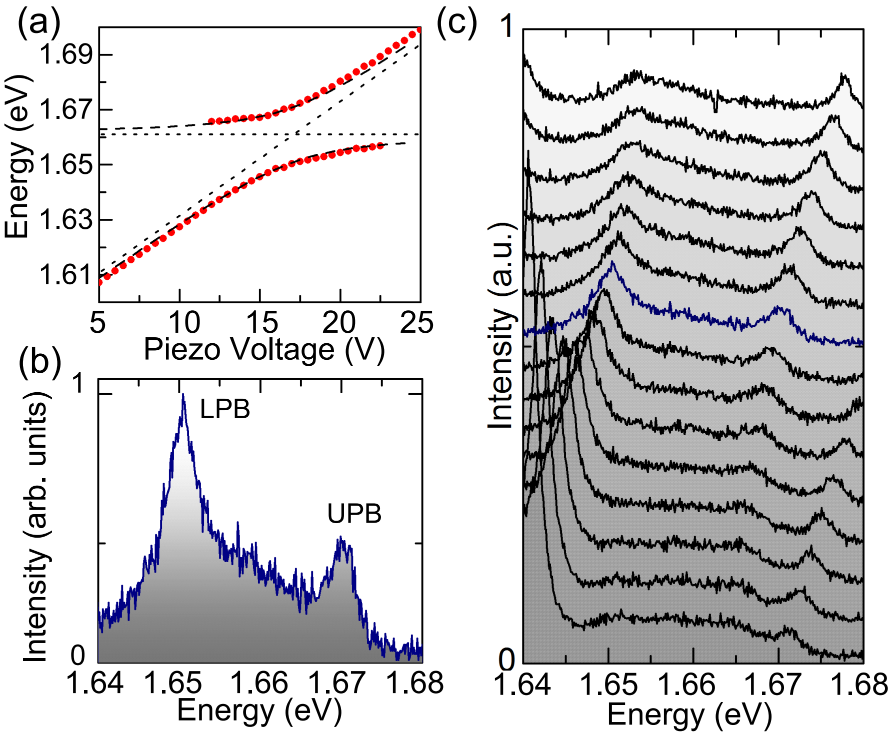

Figure 6.4: Formation of upper and lower polariton branches. The clear anti-crossing in the strong coupling regime leads to the formation of an upper and lower polariton branch. (a) Extracting the peak position of the longitudinal cavity mode highlights the anti-crossing and a vacuum Rabi splitting of 20 meV is obtained. (b) The spectrum at resonance shows that the two polariton branches are well resolved and (c) spectra for negative and positive detuning show that the anti-crossing is clearly visible.

of applied voltage which is supported by both transfer matrix simulations and reflectivity measurements. The detuning is defined as $\Delta = E_{ph} - E_{X^0}$ where E_{ph} and E_{X^0} are the fitted longitudinal cavity mode energy (TEM_{00}) and the neutral exciton energy, respectively. Spectral slices of the PL at various detunings from $\Delta = -16$ meV to $\Delta = +12$ meV are displayed in Figure 6.4(b) where the LPB and UPB can be resolved. Moreover, the PL spectrum at zero detuning shown in Figure 6.4(c) shows clearly two peaks where $\hbar\Omega_{Rabi}$ is significantly larger than the polariton linewidths γ_{LPB} and γ_{UPB}.

The polariton linewidths are plotted as a function of longitudinal mode detuning in Figure 6.5. At large negative detunings of $\Delta < -30$ meV, the LPB linewidth approaches the bare cavity linewidth of 0.8 meV due to the high photonic component of the polariton. At detunings of $\Delta = -30$ to -20 meV significant broadening of the LPB is observed, corresponding to resonance with the X^- energy. The detuning at which the increase of the linewidth occurs is in agreement with the intensity enhancement observed in Figure 6.3. The detuning of the trion to the exciton is changing slightly depending on the position of the $MoSe_2$ sheet, which explains the different detuning observed here compared to the energy separation of X^0 and X^- in Figure 6.2. This broadening is attributed to *intermediate coupling* between the X^- states and the cavity mode where the Rabi splitting is comparable to the corresponding polariton linewidths in PL but can be resolved only in reflectivity as discussed below. At zero detuning the LPB linewidth is $\gamma_{LPB} = 4.9$ meV which is less than the linewidth averaged value of $(\gamma_{X^0} + \gamma_{ph})/2 = 5.9$ meV predicted from the two-level coupled oscillator model, where γ_{X^0} and γ_{ph} are the measured inhomogeneously broadened exciton linewidth and bare cavity linewidth taken from PL measurements. This may be due to motional narrowing which is expected in systems such as this where $\hbar\Omega_{Rabi} >> \gamma_{X^0}$ leading to averaging over the inhomogeneous broadening [136]. This causes the polariton linewidth to approach $(\Gamma_{X^0} + \gamma_{ph})/2$ where Γ_{X^0} is the homogeneous neutral exciton linewidth [137]. Alternatively, this narrowing may be due to the reduced number of excitonic states that couple to the photonic mode within the 1 μm beam waist of the mode which may have a smaller linewidth in comparison to the 2-3 μm spot measured in Figure 6.1(d) due to disorder in the film. In contrast, the UPB linewidth at resonance is 8.7 meV due to broadening from relaxation through scattering to the uncoupled exciton states [138]. The radiative lifetime of the neutral exciton can be estimated from the Rabi splitting. The obtained Rabi splitting for a single monolayer sheet is $\Omega_{Rabi} = 20$ meV. Following equation 6.1, the exciton radiative rate Γ_0 and therefore the radiative lifetime τ can be obtained using:

$$\Omega_{Rabi} = \frac{20\text{ meV}}{\hbar} = 2\sqrt{\frac{2\Gamma_0 c}{n_c(L_{DBR} + L_c)}}. \tag{6.8}$$

The total cavity length is determined by the free spectral range between two longitudinal modes $(L_{DBR} + L_c) = 2.3\ \mu$m, c is speed of light and $n_c = 1.4$ is the effective cavity refractive index. This allows the exciton radiative lifetime to be calculated to be $\Gamma_0 = \frac{1}{0.8\text{ ps}}$. With $\Gamma_0 = \frac{1}{2\tau}$ the exciton radiative lifetime is then $\tau = 0.4$ ps, corresponding to a homogeneous linewidth of $\Gamma_0 = 1.6$ meV in agreement with recent work in WSe2 monolayers [139]. This is around 13x faster than the exciton lifetime of 5.3 ps measured in Figure 6.2(b) which is determined by relaxation effects to low k-states. The homogeneous exciton

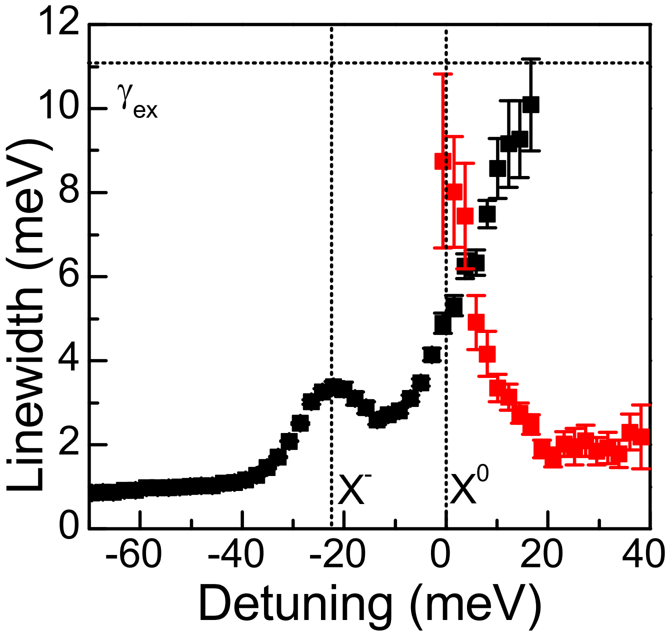

Figure 6.5: Linewidth as a function of the detuning. The linewidth of upper- (red dots) and lower (black dots) polariton branches shows the expected behavior from the Hopfield coefficients. When the lower polariton is in resonance with the charged exciton, however, an increase of the linewidth is observed.

linewdith is then given by $\Delta E = \hbar/\tau = 1.6$ meV. This is much smaller than the low temperature PL linewidth of 11 meV indicating that significant broadening occurs due to disorder effects, an aspect which might be improved using epitaxial layers allowing much narrower polariton linewidths.

The UPB is observed at positive detunings up to the recorded detunings of $\Delta = +40$ meV with a relatively narrow linewidth of around 2 meV. This is possible in TMDCs since the binding energy, E_B, is much larger than the Rabi splitting, $\hbar\Omega_{Rabi}$, and hence the electron-hole continuum is far from the polariton resonances leading to much reduced relaxation of the UPB states. This is a unique property of TMDCs which also allows both the LPB and UPB to have comparable intensities at resonance. This can be quantified further through the ratio $\hbar\Omega_{Rabi}/E_B$, which is around ≈ 0.04 for MoSe$_2$ in contrast to > 0.2 for all other materials where strong coupling was observed. This allows the UPB resonance to be both bright and narrow while remaining on the mirror stopband. A comparison

Table 6.1: Comparison of binding energy and Rabi splitting for different material systems. TMDCs show a significant difference to other material systems when the binding energy and the Rabi splitting is considered. Since the Rabi splitting is much smaller than the binding energy, the upper polariton branch is far away from the electron-hold continuum which results in a bright, narrow UPB.

Material	Binding energy in bulk (QWs)	Rabi splitting (Ω_{Rabi})	Ω_{Rabi}/E_B	Polariton linewidth at $\Delta = 0$
GaAs	4.8 ($\sim$ 14) meV [140, 141]	$\sim$ 3-15 meV [57, 142]	$\sim$ 0.2-1.1	$\sim$ 0.1-1 meV
CdTe	10 ($\sim$ 25) meV [141, 143]	$\sim$ 16-26 meV [58, 143]	$\sim$ 0.6-1	$\sim$ 0.6 meV [58]
GaN	26 ($\sim$ 40) meV [144, 145]	$\sim$ 50 meV [146]	$\sim$ 1	$\sim$ 10-15 meV [146, 180]
ZnO	60 meV[147]	$\sim$ 200 meV [129]	$\sim$ 3	$\sim$ 1.5-10 meV [129]
Organics	250 - 500 meV [148] 1 eV [130]	$\sim$ 110 meV [148] $\sim$ 200 meV [130]	$\sim$ 0.2-0.5	$\sim$ 16.5-25 meV [130, 148]
$MoSe_2$	470 meV [149]	20-29 meV	$\sim$ 0.04	$\sim$ 4-9 meV

of various material systems in which strong coupling has been observed is listed in Table 6.1.

Figure 6.6(a) shows a reflectivity scan of a single QW area. Only the longitudinal mode is visible due to the poor mode matching between the Gaussian excitation spot and the lateral transverse mode profiles. When the cavity mode is tuned through resonance with the X^- energy a small shift in the cavity energy can be observed, in contrast to the broadening observed in PL. This difference in behaviour can be understood through the dependence of the observed Rabi splitting on the measurement method, such as absorption, reflectivity or transmission, when the polariton linewidths are comparable to the mode splitting. In this case the splitting in reflectivity is expected to be larger than in PL ($\Omega_R > \Omega_{PL}$) [150].

The X^- coupling strength is proportional to $\sqrt{n_e}$ where n_e is the electron density which is due to inherent doping from impurities in the exfoliated sample [151]. In Figure 6.6(b) the measured reflectivity is theoretically reproduced based on a three-level coupled oscillator model. In this case the matrix writes as:

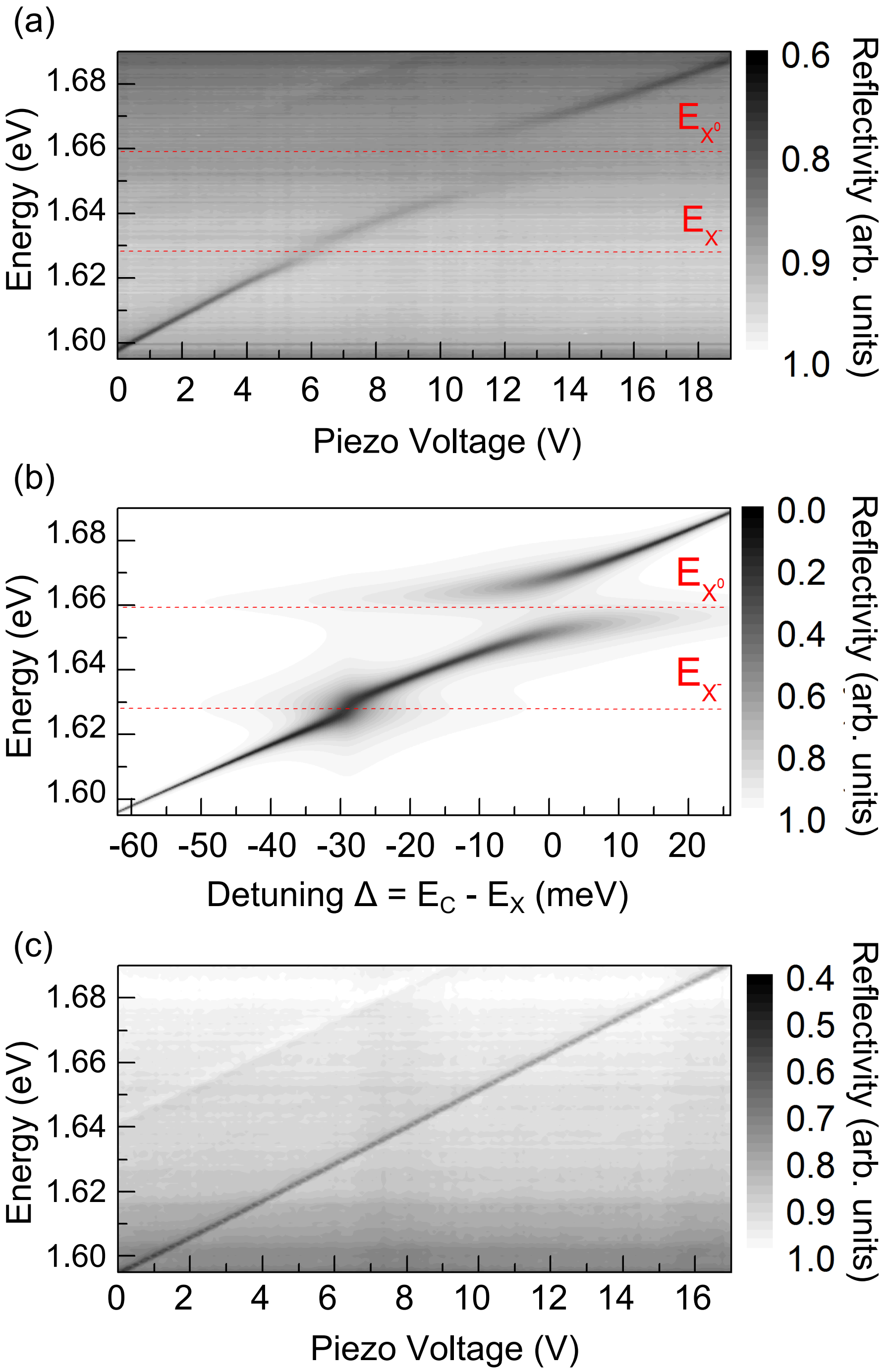

Figure 6.6: Intermediate coupling between X^- and the cavity modes in reflectivity measurements. (a) Reflectivity scan of single QW area at 4 K showing clear anticrossing with X^0. Intermediate coupling with the X^- is also apparent when close to the X^- resonance. (b) Theoretical reproduction of (a) based on a three-level coupled oscillator model with coupling strengths of 18 meV and 8.2 meV for X^0 and X^- respectively. (c) Reflectivity scan of an empty cavity with no active region showing a linear dependence of the cavity mode energy on the piezo voltage.

$$M(k) = \begin{pmatrix} E_{ph}(k) & \frac{\hbar\Omega_{Rabi(X^0)}}{2} & \frac{\hbar\Omega_{Rabi(X^-)}}{2} \\ \frac{\hbar\Omega_{Rabi(X^0)}}{2} & E_{X^0}(k) & 0 \\ \frac{\hbar\Omega_{Rabi(X^-)}}{2} & 0 & E_{X^-}(k) \end{pmatrix}, \tag{6.9}$$

where E_{ph} is the photon energy, $E_{X^0}(k)$ and $E_{X^-}(k)$ are the energies of the neutral and charged exciton and $\hbar\Omega_{Rabi(X^0)}$ and $\hbar\Omega_{Rabi(X^-)}$ are the Rabi splitting between the cavity mode and X^0 and X^- respectively. The exciton linewidths from Figure 6.2(a) are used and the coupling behaviour, using coupling strengths for X^0 and X^- of 18 meV and 8.2 meV, respectively, have been reproduced. This is consistent with the reduced oscillator strength of X^- evidenced through its low absorption [152]. It has been shown in GaAs based systems that the total oscillator strength of all excitonic components is a conserved quantity and hence the presence of X$^-$ due to doping reduces the coupling strength of X^0 [151]. A reflectivity scan of an empty cavity is performed in order to show the linear dependence of the energy tuning with the applied Piezo voltage and to proof that the observed features indeed come from the light-matter interaction between the cavity and the heterostructure. This is shown in Figure 6.6(c).

Figure 6.7 (a) shows the peak polariton intensity plotted against longitudinal mode detuning. In resonance with X^- (detuning $\Delta = -30$ meV) the peak intensity is two orders of magnitude larger than when in resonance with X^0. The integrated intensity is shown in Figure 6.7(b) showing a significant integrated PL enhancement when in resonance with X^-. This is attributed to the interplay between the maximum polariton intensity occurring at negative detunings [153] as well as intermediate coupling close to X^- resulting in a Purcell enhancement.

The PL emission of the bilayer area marked by the black border in Figure 6.1(b) is shown in Figure 6.8(a). The bandstructure of bilayer MoSe$_2$ shows that there is an indirect transition causing a reduction in the emission efficiency. When the bilayer is coupled to the cavity modes, weak coupling is observed as shown in Figure 6.8(b) where a crossing through the exciton is observed.

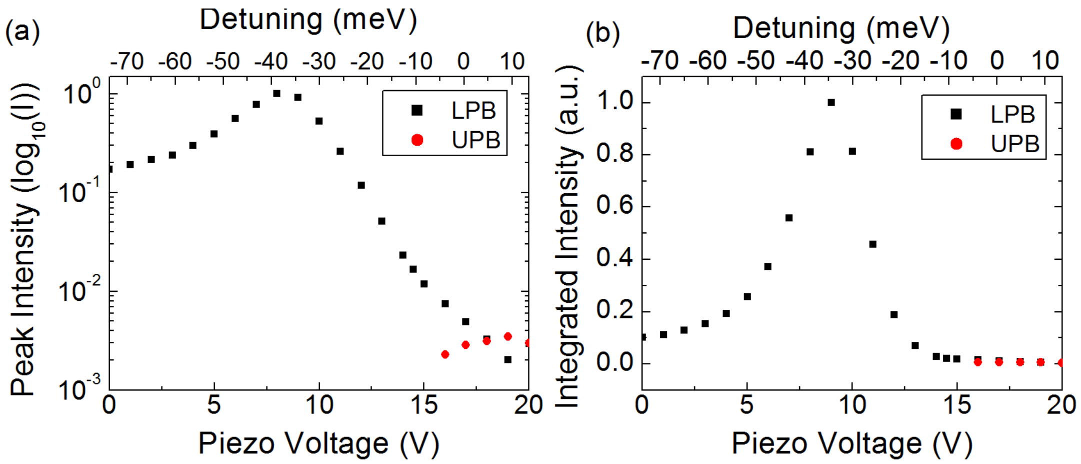

Figure 6.7: Polariton intensity at different detuning. (a) Peak intensity of the longitudinal resonance polariton as a function of piezo voltage. (b) Integrated intensity as a function of piezo voltage.

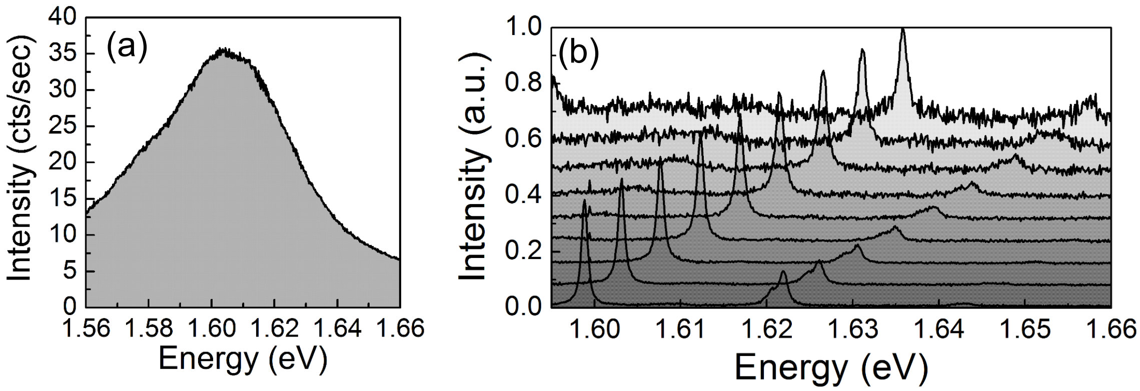

Figure 6.8: Crossing between the cavity modes and bilayer heterostructure area. (a) Bilayer emission due to indirect transition at 4 K. (b) Spectra of the cavity emission with a bilayer active region showing weak coupling.

6.4 Strong coupling in multiple quantum wells

The PL spectrum of X^0 at room temperature shows a linewidth of around 35 meV, as shown in Figure 6.9, exceeding the vacuum Rabi splitting of the single QW heterostructure. Therefore weak coupling is observed at room temperature.

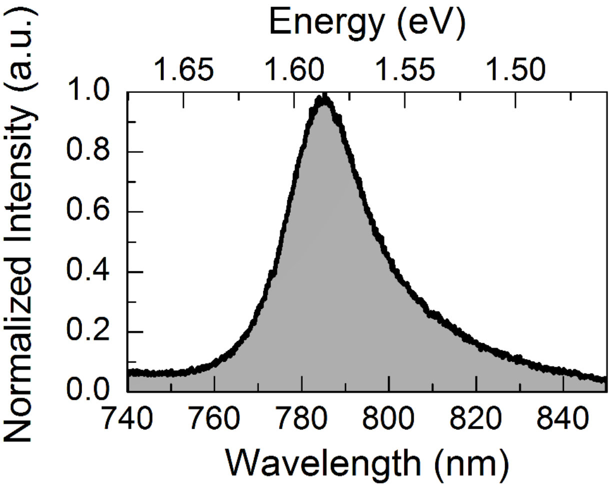

Figure 6.9: Typical room temperature PL spectrum of a monolayer $MoSe_2$ sheet. A single broad resonance of X^0, with a linewidth of 35 meV, is observed at room temperature.

Increasing the number of quantum wells, N_{QW}, leads to an increase of the Rabi splitting following $\Omega_{rabi} \propto \sqrt{N_{QW}}$ [133]. This dependence indicates that a heterostructure consisting of four or more $MoSe_2$ QWs will increase the Rabi splitting sufficiently to resolve both the UPB and LPB at room temperature. Figure 6.10(a) shows the PL spectra from a cavity formed with the double QW region of the heterostructure as the active region where the anti-crossing between the cavity modes and the neutral exciton is shown. A fit to the polariton peak energies using the coupled oscillator model as before is shown in Figure 6.10(b) revealing an increased Rabi splitting of 29 meV. Compared to the 20 meV in a single QW, this is in agreement with the expected scaling of the Rabi splitting. The spectrum at resonance is shown in Figure 6.10(c) where the two polariton branches are fully resolved. A heterostructure consisting of 4 $MoSe_2$ QWs is expected to exhibit a Rabi splitting of at least 40 meV, which is required to exceed the room temperature exciton linewidth of 35 meV. However, to obtain narrow polariton resonances at room temperature, half of the Rabi splitting has to be larger than the linewidth of the exciton resonance. The fabrication of VDW heterostructures with large numbers of QWs should allow the observation of room temperature polariton states.

A similar experiment has also been carried out in a WSe_2 EL device, similar to the device discussed in chapter 7. Figure 6.11 shows a number of longitudinal and transverse modes which are tuned through the energy of the neutral exciton of WSe_2. The characteristic anti-crossing is also observed in WSe_2 indicating the system is in the strong exciton-photon coupling regime in PL. However, the observed Rabi splitting of only 9.2 meV is drastically reduced in comparison to the single QW sample using $MoSe_2$. It should be noted that no anti-crossing is observed when the EL device is operated in the EL regime.

This unexpected reduced Rabi splitting is explained by the design of the EL device as described in the following. In contrast to the previous heterostructure, a thicker boron nitride film is used to produce the device. The entire EL device is sitting on a $\sim$30 nm thick hBN film, ensuring that the EL device is sitting flat. This is important so that not only the TMDC shows good optical properties, but also so that the graphene contacts allow efficient charging. It has been demonstrated that graphene sitting on hBN is showing a significant improvement in its transport properties. Additionally to this hBN film two tunnel barriers, which are 3 nm thick each, are used between the graphene contacts and the TMDC quantum well as tunnel barrier. Obviously, by increasing the thickness of the EL device, the active material shifts off the electric field anti-node which results in a reduction of the light-matter interaction. So far the assumption is made that the monolayer structure is sitting at the anti-node of the electric field, similar to the model shown in Figure 6.12.

The bottom DBR terminates with the low refractive index material in order to ensure that the anti-node of the electric field is at the surface of the sample. The position where the monolayer sits is highlighted with the blue line in Figure 6.12. Qualitatively there is no difference observed when the cavity length is increased leading to more anti-nodes would fitting the two mirrors. The top mirror terminates with the high refractive index since the air gap serves as the low refractive index environment to form the cavity. However, as shown in Figure 6.13, hBN has a larger refractive index than low refractive material of the DBR. This means that when a layer of hBN is placed on the surface of the bottom

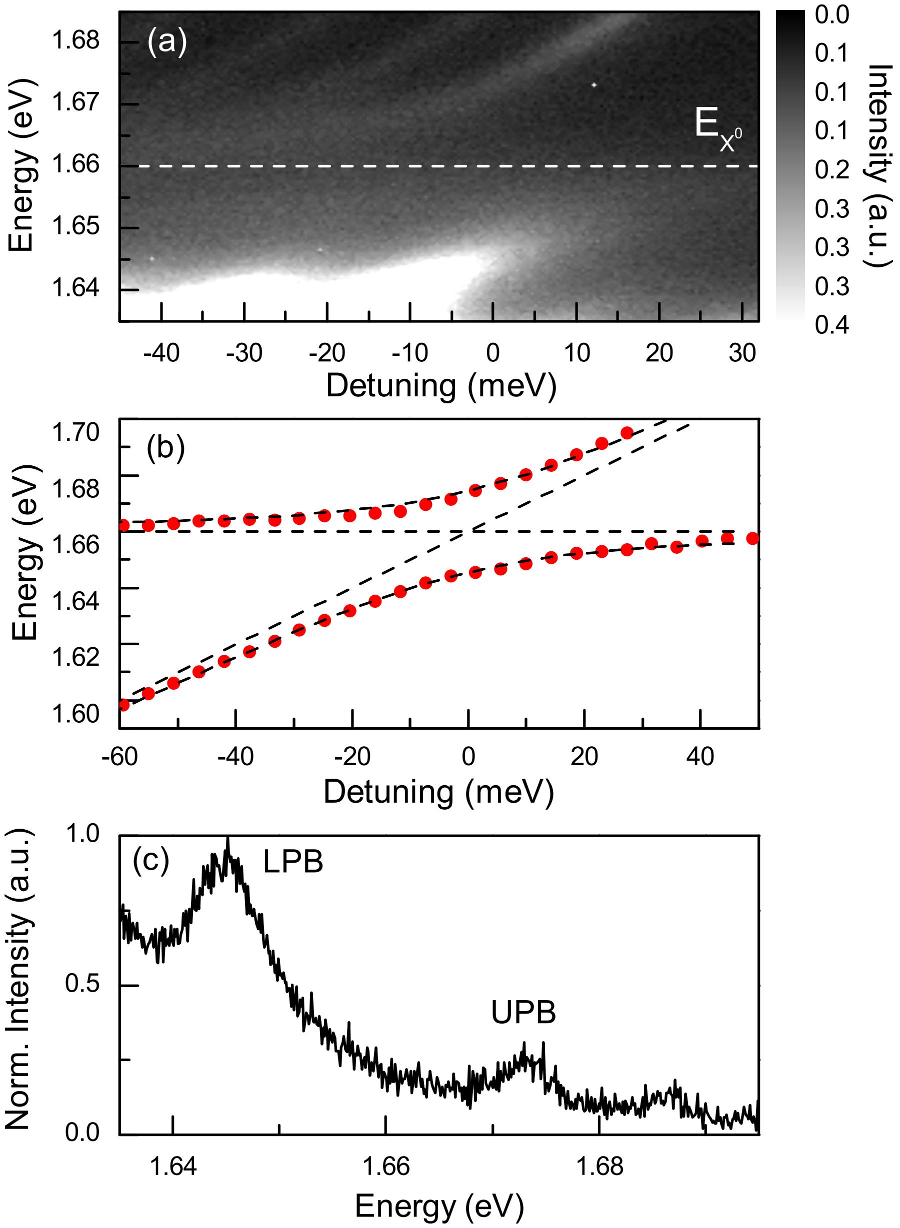

Figure 6.10: Anticrossing with a double quantum well heterostructure. (a) The double QW structure shows an anticrossing between the neutral exciton and discrete cavity modes at 4 K. Here the intensity is saturated when the cavity mode is in resonance with the charged exciton in order to highlight the anti-crossing of the neutral exciton. (b) A fit to the peak position as a function of detuning yields a Rabi splitting of 29 meV. (c) The upper and lower polariton branches are well resolved at resonance.

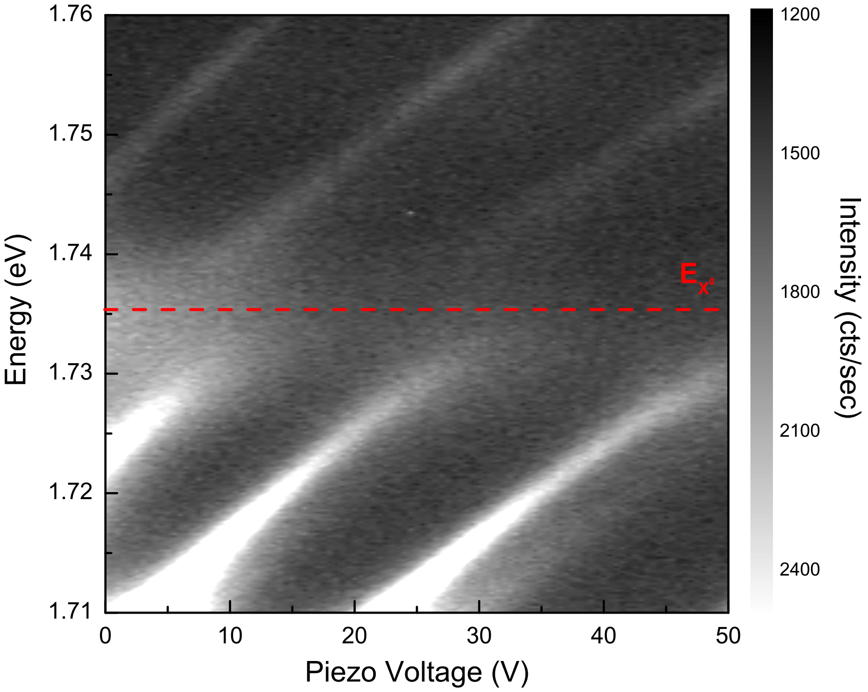

Figure 6.11: Anticrossing with a WSe$_2$ EL device. The Rabi splitting is significantly reduced due to the large hBN layer required to produce the sample.

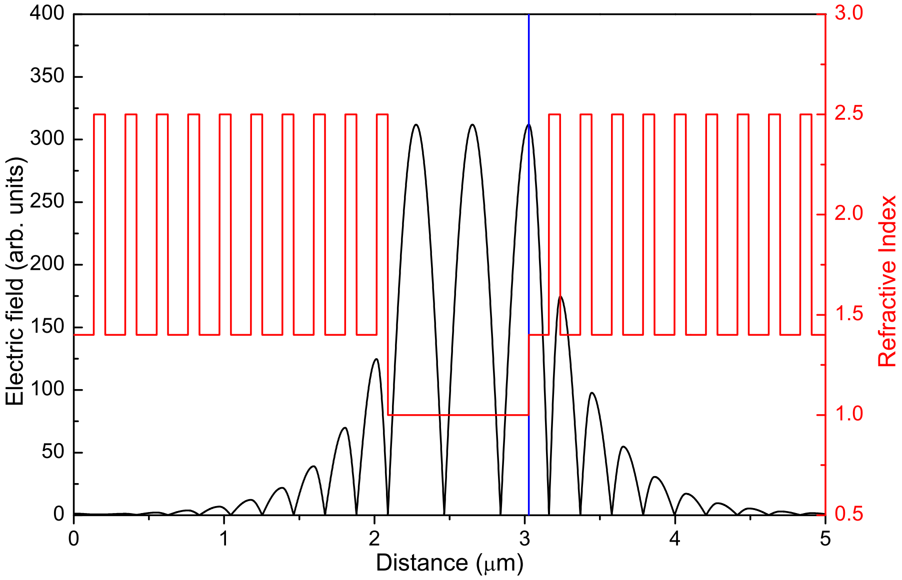

Figure 6.12: Microcavity design without boron nitride. Microcavity design for a $3\lambda/2$ cavity showing the refractive index profile in red and the calculated electric field in the cavity in black. The anti-node of the electric field is at the surface of the planar mirror where the monolayer structure is sitting.

DBR the active material is shifted off the anti-node of the electric field inside the cavity.

The light-matter interaction is reduced when the active material is not placed at the maximum of the electric field E_{max}, scaling with:

$$I \propto \frac{E(z)}{E_{max}}. \tag{6.10}$$

In case of a $\lambda/2$ cavity, the maximum of the electric field is still at the same anti-node and the effect of hBN is significantly reduced. In the open cavity, however, not only is the surface of the sample shifted from the local maximum of the electric field, due to the higher refractive index of hBN, compared to the SiO_2 layer, the absolute maximum of the electric field is no longer placed at the anti-node near the bottom DBR. Therefore, the hBN substrate on which the EL devices is placed on is detrimental to the light-matter interaction in this device. Figure 6.14 shows the ratio of $E(z)/E_{max}$ as a function of the hBN thickness. It shows that the interaction, and therefore the Rabi splitting is already

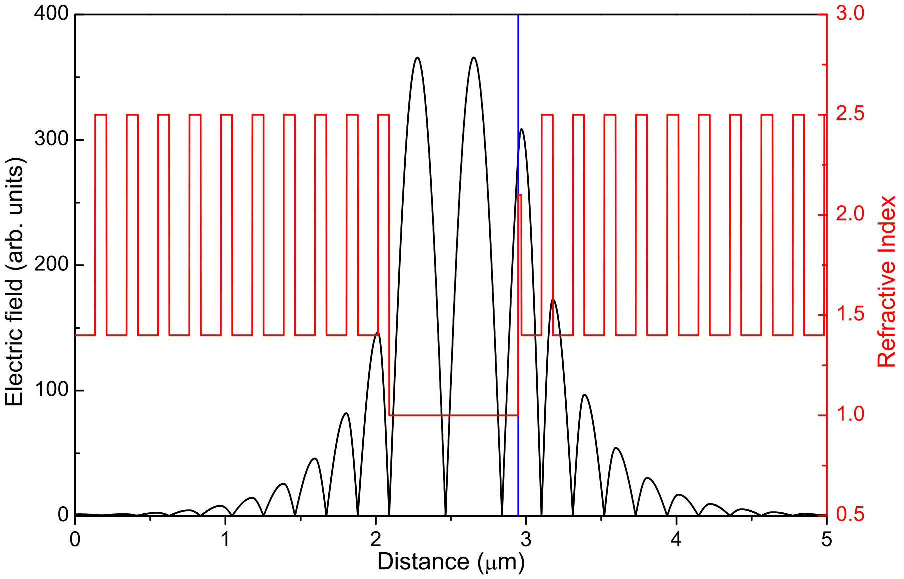

Figure 6.13: Microcavity design with boron nitride. A thin layer of hBN is added on top of the bottom DBR. The maximum of the electric field is shifted away from the DBR resulting in a reduced light-matter interaction.

reduced to 0.65% when the hBN thickness is around 30 nm. In order to study EL devices in the strong coupling regime, the devices have to be fabricated with much thinner hBN layers.

6.5 Summary

In summary, for the first time, a conclusively demonstration of strong exciton-photon coupling of $MoSe_2$ heterostructures in tunable optical microcavities through the observation of an anticrossing with the neutral exciton energy in PL and reflectivity has been observed. For a single $MoSe_2$ monolayer a Rabi splitting of 20 meV is observed for X^0. An intermediate coupling regime with X^- is observed, present due to the inherent doping from impurities in the monolayer films with an estimated coupling strength of 8.2 meV. Additionally the demonstration of multiple QW TMDC heterostructures in the strong coupling regime where the Rabi splitting is increased to 29 meV opens a new avenue in roomtemperature polaritonics. Unique to TMDCs microcavities is the presence of a bright and narrow UPB due to the large exciton binding energy causing the electron-hole continuum

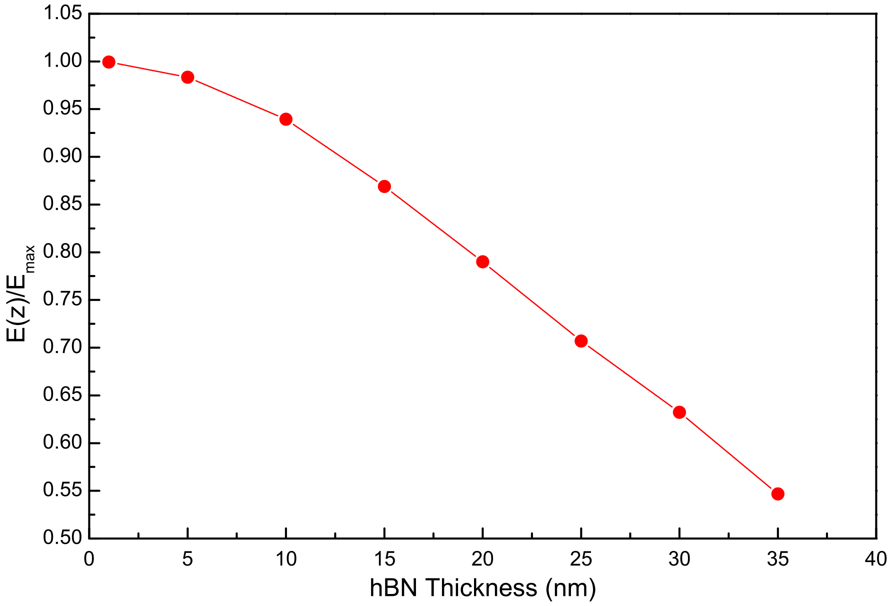

Figure 6.14: Reduced light-matter interaction depending on the thickness of hBN. Extracting the electric field at the surface of the hBN layer divided by the maximum of the electric field as a function of the hBN thickness shows that the interaction, and therefore the Rabi splitting for example, is reduced by a factor of 2 after only several tens of nm hBN.

to be far from the polariton resonance. This will allow the potential realisation of phenomena involving the UPB, such as highly non-linear parametric processes with balanced idler/signal, or polariton quantum-bits [154]. Other interesting features of van der Waals crystal based polaritonics may include studies involving the spin-valley coupling between excitonic states which leads to the formation of LT-polarised excitons with potential large polarisation splitting that will be inherited by the polaritonic system [155]. This type of spin-orbit interaction is at the origin of the optical spin Hall effect [156] and the formation of a persistent spin currents in polariton condensates [157]. It allows manipulation of polariton trajectories through the emergence of non-Abelian gauge fields [158]. Lattices of coupled open cavities [159] filled with VDW heterostructures could be realized in the near future and serve as a basis for the realization of polaritonic topological insulators [160] at room temperature operation.

7 Electroluminescence devices embedded in microcavities

In this chapter the incorporation of electrically pumped light-emitting devices in monolithic microcavities is demonstrated. This is the first demonstration of electrically pumped devices, based on 2D materials, which are embedded in photonic structures. In the previous chapters it has been demonstrated how microcavities can modify the light-matter interaction in 2D materials. The development of electrically pumped devices is essential when aiming towards opto-electronic devices. Furthermore, while the tunable open-acces microcavity serves as ideal tool to study the light-matter interaction, monolithic devices are required for potential applications. Here, the optical properties of the EL device are discussed first before the coupling of EL and PL to photonic cavity modes are shown. Vertically stacked van der Waals heterostructures allow a flexible design of opto-electronic devices combining unique properties of individual monolayer materials. Their natural property of weak interlayer bonding allows a large number of combination of stacks that has been shown to create and tune the properties of the materials. Recently, electroluminescence of p-n junctions based on WSe_2 [162, 163] and VDW heterostructures that allow vertical current injection has been reported [55]. A similar device has been fabricated in this work. A schematic of the device layout is shown in Figure 7.1. It consists of a hexagonal boron nitride (hBN) substrate on which the bottom graphene contact is transferred, followed by a hBN tunneling barrier and monolayer WSe_2 are used as active material. The device is finished by a hBN tunneling barrier and a graphene top contact. The contacts are guided towards the edge of the sample where it is contacted using silver paint. While the thickness for graphene and the TMDC is limited to one atomic layer, the thickness of hBN is designed so that the tunnel barrier allows efficient carrier injection while the leakage current is not too high. Typically the thickness varies between 1 nm and 3

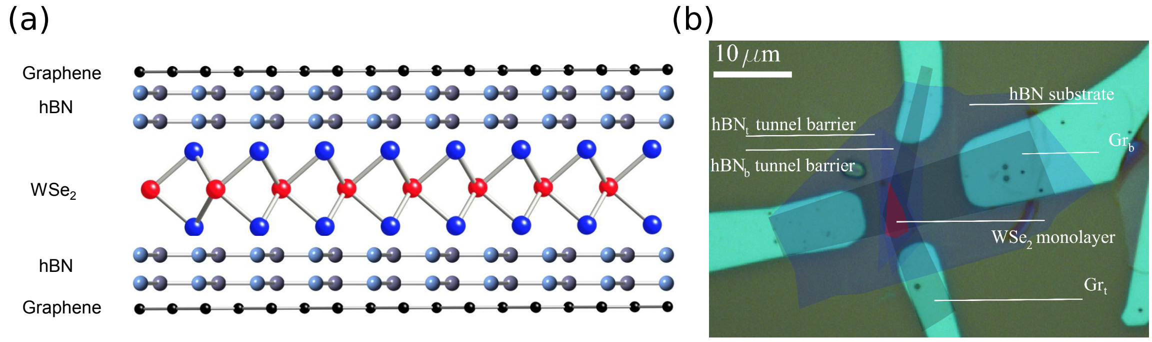

Figure 7.1: Vertically stacked heterostructure used to produce an electroluminescence device. (a) The graphene layers are used for electric contacts and the hBN layers serve as tunnel barrier allowing efficient carrier injection into the active material, WSe$_2$. (b) Optical image of the sample showing the heterostructure and the gold contacts.

nm.

7.1 Optical properties of tungsten diselenide

Tungsten diselenide (WSe$_2$) is a TMDCs with very unique properties compared to other TMDC materials. A typical PL spectrum of a monolayer sheet at a temperatures of 4.2K is shown in Figure 7.2. It highlights the complex nature of this material. The peaks marked as X^0 and X^- are the neutral and charged exciton respectively. The binding energy of the charged exciton, which is shown through the energy difference between X^0 and X^-, is 30 meV agreeing with the binding energy reported previously [152]. The feature $P0$ stems from biexcitons where a superlinear power dependence has been demonstrated prior to this work [164]. The origin of the features $P1$ and $P2$ is not generally clear to this point. Previous reports claimed that they stem from defect states [28] but recent discussions suggested that they are dark trion states. Finally, the broad feature $P3$ is attributed to defects, where at low excitation power quantum dot-like features have been observed [40–43].

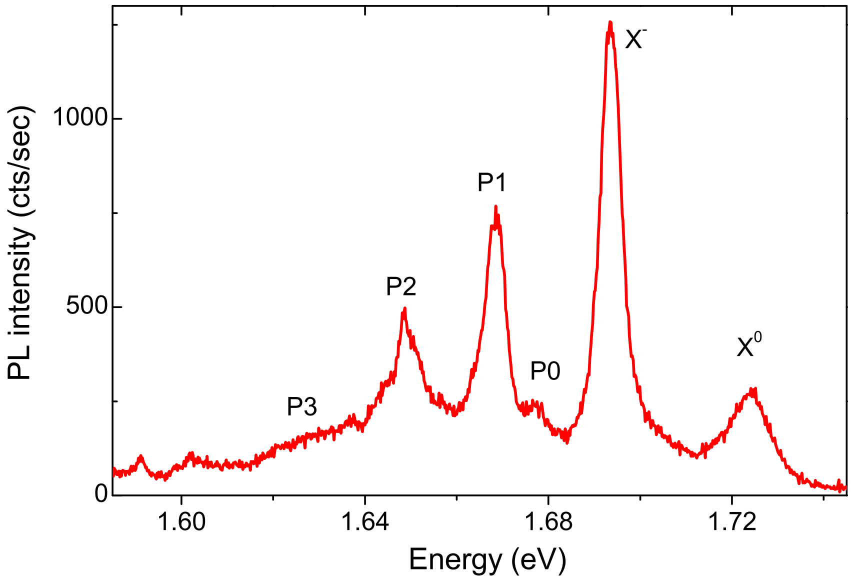

Figure 7.2: Typical photoluminescence spectrum of a monolayer sheet of WSe$_2$. The PL emission shows a spectral feature for the neutral and charged exciton, X^0 and X$^-$. The peaks P0-P3 are attributed to a biexciton, exciton features shifted due to the spin-orbit coupling, and localized states.

7.1.1 Valley Polarization of monolayer WSe$_2$

The localized states in the PL spectrum are a composition of quantum dot-like features as shown in Figure 7.3 where a slightly different position of the monolayer sheet is measured. The peaks consist of a doublet, which cannot be resolved because the linewidth is larger than the fine-structure splitting of the quantum dot-like defect. A polarization dependent measurement shows a linear polarization with a polarization degree of up to:

$$V = \frac{I_{\parallel} - I_{\perp}}{I_{\parallel} + I_{\perp}} = 88.97\%. \tag{7.1}$$

The doublet appears because of the fine-structure splitting in the quantum dots. In conventional semiconducting quantum dots a linear polarization is observed for asymmetric quantum dots due to the electron-hole exchange interaction [165].

No linear polarization dependence is observed for the exciton transitions in Figure 7.2. Similarly to previous reports, however, a circular polarization degree of up to $V = 52.64\%$

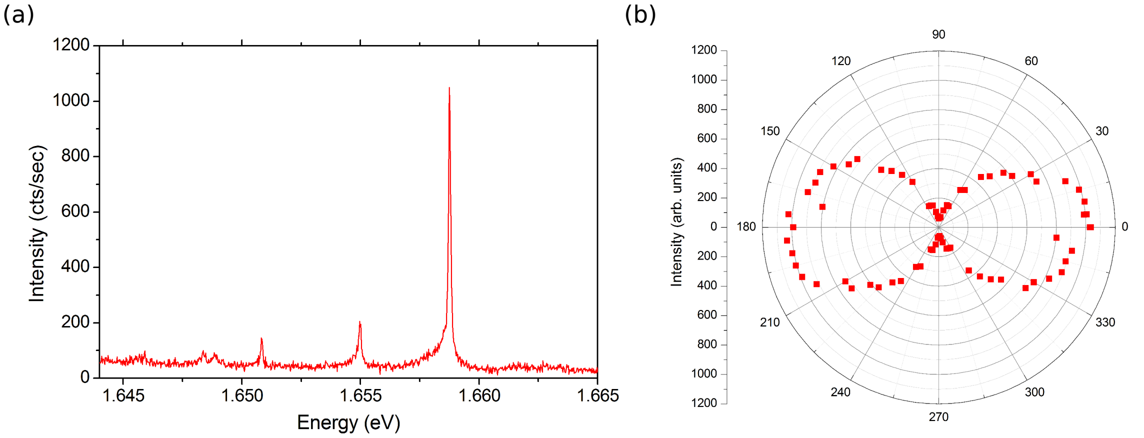

Figure 7.3: Characterization of the quantum dot-like features in WSe_2. (a) The sharp quantum dot-like features stem from localized defects in the WSe_2 layer and (b) consist of a linear polarized doublet with a polarization degree of 88.97%.

has been observed for non-resonance excitation as shown in Figure 7.4. As discussed in chapter 2, the strong spin-orbit coupling leads to a large valence band splitting in the order of 300 meV in the case of WSe_2. The two valleys are located in the K and K' point of the Brillouin zone and due to the inversion symmetry breaking in a monolayer sheet of TMDCs the two valleys are addressed with different polarizations, σ^+ and σ^- respectively. Therefore, circularly polarized light selectively excites an electron-hole pair in one valley and this valley polarization is retained during hot-carrier relaxation, exciton formation and radiative recombination processes. Intervalley scattering processes are suppressed by the large momentum separation between the valleys and are therefore slower than the very fast recombination with sub-picosecond carrier lifetime.

7.1.2 Valley Zeeman splitting in monolayer WSe_2

To prove that the origin of the polarized PL is indeed the valley and not the spin, magnetic field measurements have been performed with MoS_2 where the polarization degree is preserved to a transverse magnetic field up to 9 T. A transverse magnetic field would cause the spin to precess and thus reduce the polarization degree. This is called the Hanle effect. A magnetic field leads to a splitting of the exciton states due to the valley depen-

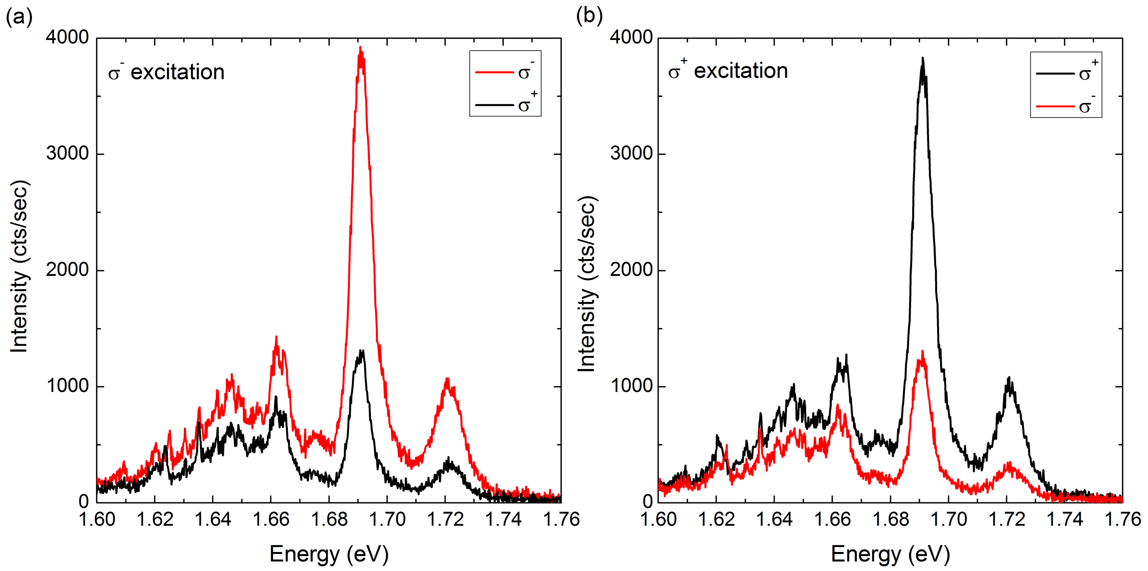

Figure 7.4: Circular polarization degree of the excitonic features in WSe_2. Circularly polarized PL is observed for (a) σ^- and (b) σ^+ excitation where the polarization degree is around 52% in both cases.

dence of the magnetic moment **m**. Polarization dependent measurements show that the different valleys are addressed with σ^+ and σ^-, respectively, but the valleys are degenerate. Applying a magnetic field B leads to a splitting between the excitons in the different valleys which results from a combination of three effects. First, the exciton transition is coming from spin-up and spin-down transitions which have a magnetic moment $\pm\frac{1}{2}$. The magnetic moment is, therefore, either parallel or anti-parallel to the magnetic field and causing a shift to higher and lower energies respectively. The energy shift is calculated by:

$$\Delta_s = g_e \mu_B B. \tag{7.2}$$

Here, $\mu_B = 5.788 \times 10^{-5}$ eV/T is the Bohr magneton, the natural unit for expressing the electron magnetic moment. The g-factor, g_e, is a multiplicative term and is used to quantify magnetic moment. The magnetic moment of the tungsten d-orbitals leads to a shift of the valence band with $m = \pm 2$ for the $\pm$K valleys (here -K corresponds to K' valley). The conduction band is unaffected by the atomic orbital moment, $m = 0$, so that the energy shift is given by:

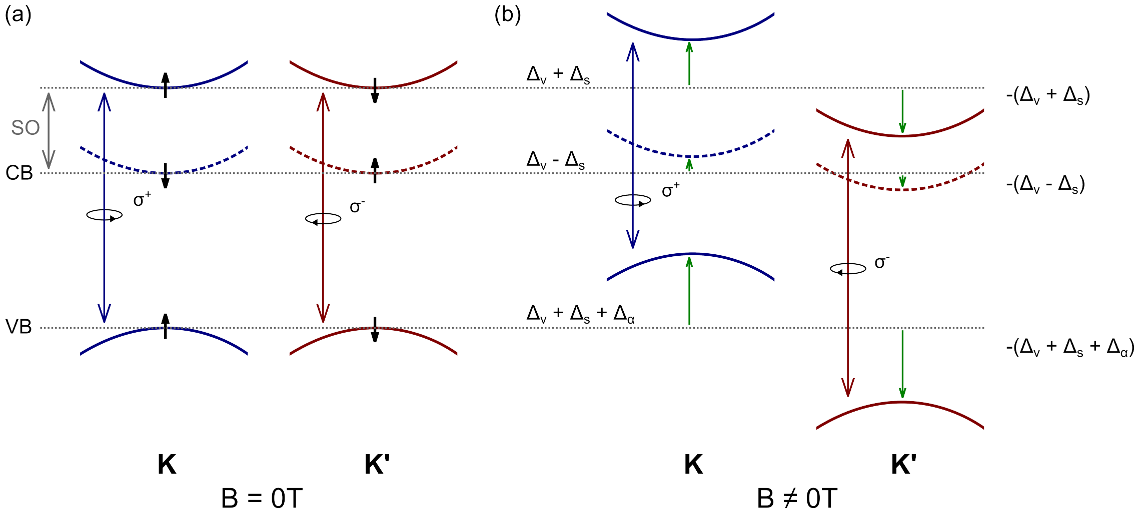

Figure 7.5: Energy shifts caused by the valley Zeeman splitting. (a) Bandstructure of monolayer WSe_2 showing the valence and spin-split conduction band. The black arrows indicate the spins, a bright exciton transition is observed for the higher energy conduction band to the valence band, addressed with σ^+ and σ^- for K and K' valleys. (b) Applying a magnetic field results in an energy shift for conduction and valence band in both valleys, for different magnitude.

$$\Delta_\alpha = \pm 2\mu_B B. \tag{7.3}$$

Finally, a shift is observed due to the valley magnetic moment, called valley Zeeman shift, which is described by:

$$\Delta_v = \pm g_v \mu_B B. \tag{7.4}$$

As recently reported, via $\mathbf{k}\cdot\mathbf{p}$ approximation a massive Dirac fermion model is obtained for the band-edge carriers with $g_v = m_0/m^*$, where m^* is the effective mass [166]. Considering the orientation of the spins and pseudo-spins in this system, the total energy shift is shown schematically in Figure 7.5.

Because the spin of the optical transitions is the same for conduction and valence band, both bands shift in the same direction when a magnetic field is applied so that no splitting is observed due to the spin magnetic moment. The orbital contribution leads to a shift caused

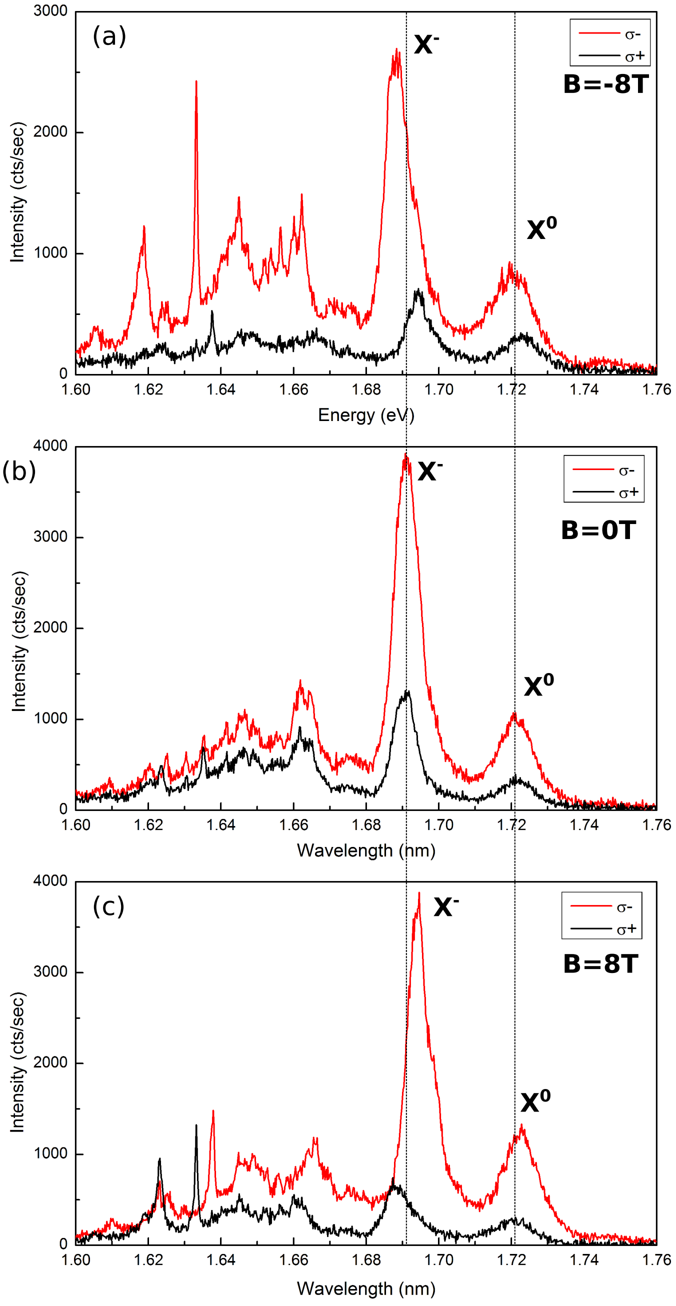

Figure 7.6: Valley Zeeman splitting observed in PL. Polarization dependent PL measurements with σ^- excitation has been performed at (a) -8T, (b) 0T and (c) +8T, where the valley Zeeman splitting is shown.

by the magnetic moment of $m = 2$ for K and $m = -2$ for K', resulting in a total shift of $\Delta m = 4$. This allows to determine a value of the valley magnetic moment by measuring the total Zeeman splitting where different effective masses and different valley magnetic moments for the electron and holes are taken into account. This results in a net valley Zeeman splitting larger than 4, which would be expected when only the orbital contribution is considered. Figure 7.6 shows three spectra at -8T, 0T and +8T, in order to demonstrate the shift and the preservation of a polarization degree.

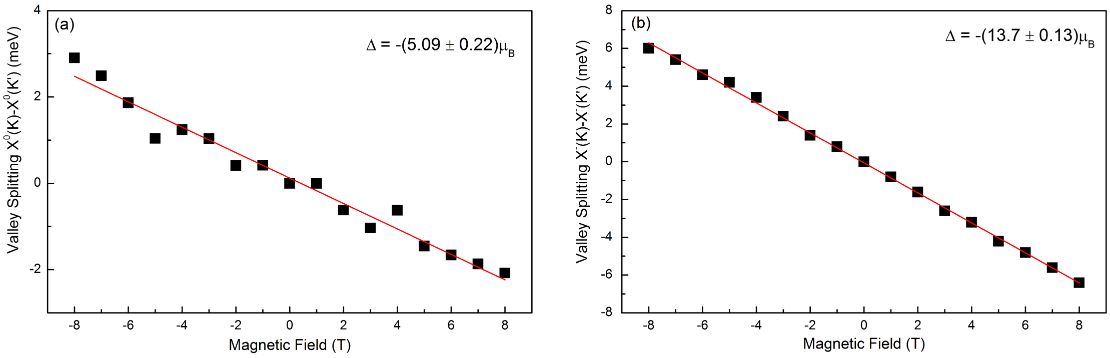

Figure 7.7: Extracted Zeeman splitting for X^0 and X^-. The peak positions of the excitons are extracted in the K and K' valley as a function of the magnetic field. The valley Zeeman splitting is then given by (a) X^0(K)-X^0(K') for the neutral exciton and (a) X^-(K)-X^-(K') for the charged exciton.

By measuring the peak position of the split exciton, the Zeeman splitting is extracted for the neutral and charged exciton, as shown in Figure 7.7. It should be highlighted that the energy shift is less than the exciton linewidth so that simply fitting the exciton peaks using a Lorentzian function is not possible in order to extract the peak position [166, 167]. Here the spectra are processed using a low pass filter and the peak position is extracted by finding the maximum of the smoothened exciton peaks. The extracted Zeeman splitting is $-(5.09 \pm 0.22)\mu_B$ for X^0 and $-(13.7 \pm 0.13)\mu_B$ for X^-. The observation of the valley Zeeman splitting provides evidence for the predicted bandstructure of TMDCs and shows that the valley degree of freedom serves as a pseudo-spin index.

7.2 Electroluminescence devices

The heterostructure shown in Figure 7.1 allows electrical carrier injection by applying a bias voltage between the two graphene contacts. The band alignment of the heterostructure for zero bias is shown in Figure 7.8(b). With increasing bias voltage V_b the bandstructures are tuned as shown in the Figure 7.8(c). At some point the Fermi level in the bottom graphene electrode lies above the conduction band of WSe_2 allowing injection of electrons in the active material. At this bias the conductivity of the device significantly changes because of the increased tunneling probability, allowing an increased current flow, as shown in the IV-curve in Figure 7.8(a).

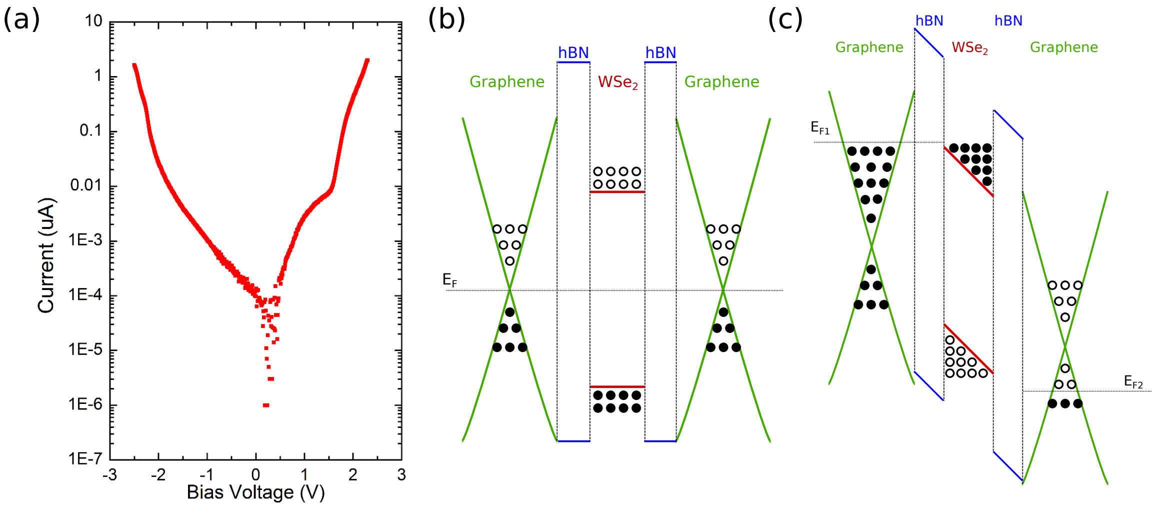

Figure 7.8: IV-curve and band alignment of the EL device. (a) A typical IV-curve shows that the conductivity changes significantly once the quasi-Fermi level of the graphene contact is tuned to a higher energy than the conduction band edge of the WSe_2 layer. At this bias the tunneling probability is significantly enhanced. The band alignment of the heterostructure shows the Dirac cones of the graphene contacts, the hBN tunnel barriers and the WSe_2 layer as active region for (b) zero bias and (c) the onset bias for EL, where the quasi-Fermi levels of the graphene contacts are aligned with the minimum of the conduction band and the maximum of the valence band, respectively.

The threshold voltage for electroluminescence (EL) is reached when the Fermi level of the top graphene is below the edge of the valence band so that holes are injected into the WSe_2 from the top electrode, as shown in Figure 7.8(c). At this point the formation of excitons in the WSe_2 layer and their radiative recombination is possible. A bias dependence of the

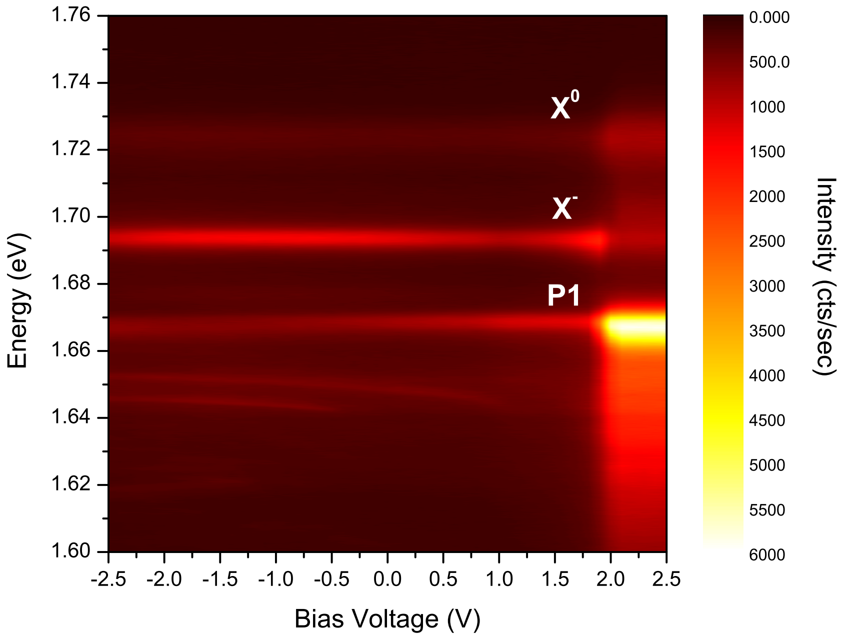

Figure 7.9: **Bias dependence of the PL emission in the WSe_2 device.** By increasing the bias voltage electrons are injected to the WSe_2 resulting in an increase of the charged exciton. The onset voltage for EL is around 1.9V, at which the EL is dominated by the P1 peak.

PL emission from a device without a cavity is shown in Figure 7.9 where features shown in Figure 7.2 are visible. By increasing the bias voltage the charged exciton contribution increases because more electrons are injected into the conduction band of the WSe_2 layer. The threshold voltage where the EL is observed is around 1.9 V. The main contribution of the EL signal stems from the feature $P1$ in Figure 7.2 as discussed further in Figure 7.10.

Figure 7.10 shows the EL for positive and negative bias voltage, where the different onset bias voltage for opposite polarity is explained by different thicknesses for the two hBN tunneling barriers. The EL is shown for different bias voltages and highlights that, especially for positive bias, the feature $P1$ is dominating the spectrum. The maximum current through the device is set to 2 μA, which is reached for 2.3V in positive bias. The spectra show the four of the explained features. For negative bias (Figure 7.10(a)) the neutral exciton X^0 is negligible compared to the charged exciton X^-, while the features $P1$ and $P2$ are dominating signal. By increasing the bias it appears that the low energy state, $P2$, is populated

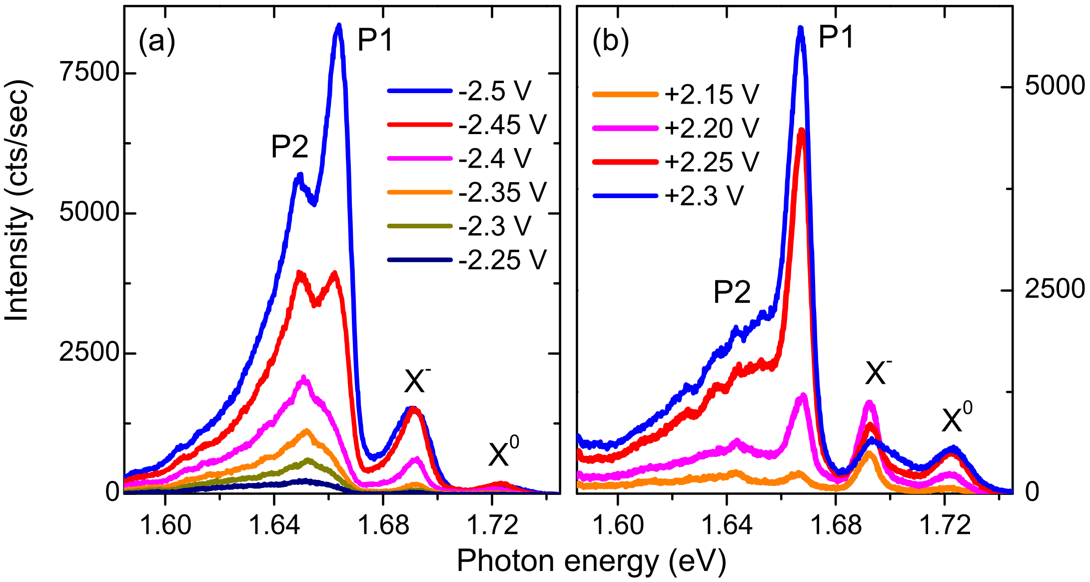

Figure 7.10: Electroluminescence spectra of the WSe$_2$ device. The EL for (a) negative and (b) positive bias shows similar spectral features compared to the PL spectrum above. However, the EL spectra are dominated by the P1 peak.

first before the emission from $P1$ starts to dominate the spectrum. Because in EL the entire sample is excited, an ensemble of quantum-dot like features are observed, resulting in a broad shoulder towards lower energy. Similar behavior is observed for positive bias (Figure 7.10(b)), where the $P2$ state appears to be broadened.

Magnetic field measurements are also performed in EL, which is shown in Figure 7.11 for negative bias at $V_B = -2.5$ V. The magnetic field results, again, in a valley Zeeman splitting, similar to the Zeeman splitting observed in PL. Because the EL is dominated by the peaks $P1$ and $P2$, the valley Zeeman splitting for these peaks is extracted in Figure 7.12. The Zeeman splitting for X^0 and X$^-$ is found to be similar compared to the values obtained in PL, but because the total energy shift is less than the exciton linewidth, it is difficult to conclusively extract the exact peak position for the relatively weak exciton peaks. In EL the injected carriers have no preferential spin and therefore populate the K and K' valley with the same probability, leading to an equal contribution of σ^+ and σ^- emission in EL. Due to a magnetic field, however, a polarization degree of 18% is observed for a magnetic field of -8T, where the emission corresponding to the valley, which is tuned to a high energy, is more robust than the low energy peak.

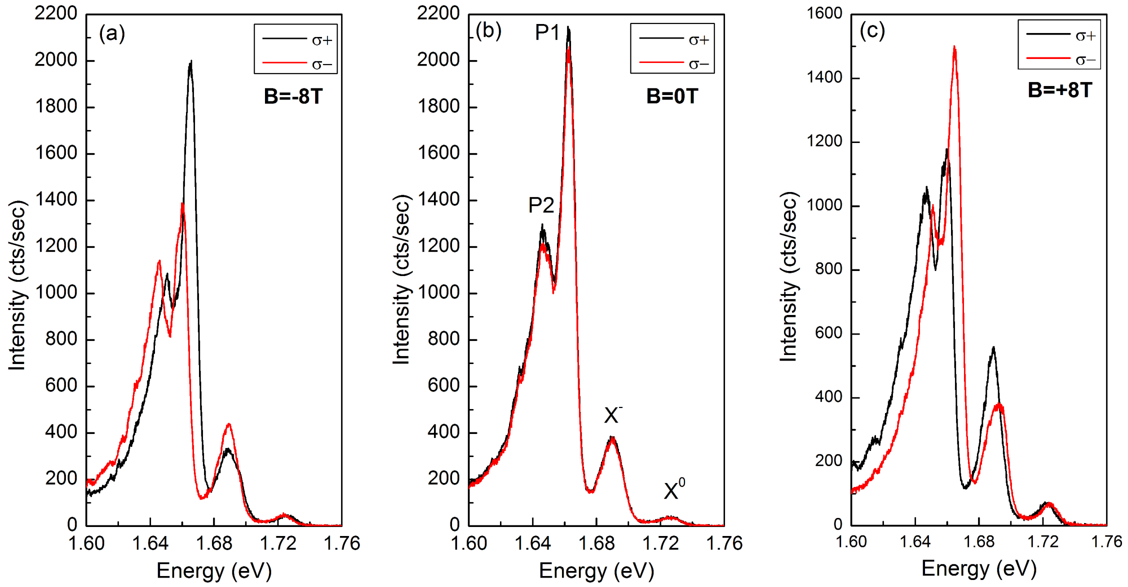

Figure 7.11: Valley Zeeman splitting in electroluminescence. The EL is measured for a bias voltage of -2.5V for a magnetic field of (a) -8T, (b) 0T and (c) +8T, where the valley Zeeman splitting is observed. Additionally a valley polarization is observed in EL due to the Zeeman splitting caused by the magnetic field.

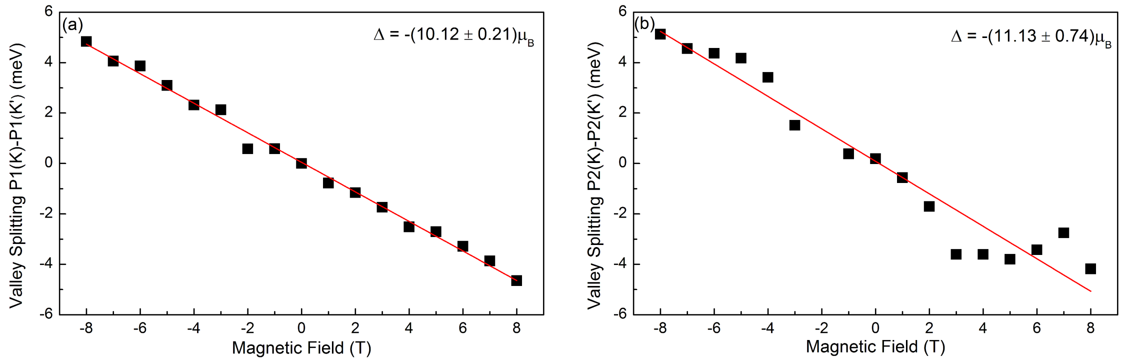

Figure 7.12: Valley Zeeman splitting for the peaks $P1$ and $P2$. The EL spectra are dominated by the two peaks, $P1$ and $P2$, for which a valley Zeeman splitting of (a) $\Delta = -(10.12 \pm 0.21)\mu_B$ is extracted for $P1$ and (b) $\Delta = -(11.13 \pm 0.74)\mu_B$ for $P2$.

7.3 Electroluminescence devices coupled to microcavities

Microcavity structures or waveguides are often used as a mean to enhance light absorption or emission in a semiconductor. This has been shown on graphene, for example, where an increase of the photocurrent in a photodetector has been observed [65]. PL enhancement has been demonstrated in MoS_2 and WSe_2 monolayer sheets coupled to photonic crystal cavities [66] and more recently, also photonic lasing has been shown with monolayer WSe_2 in a photonic crystal cavity and WS_2 in a micro-disk cavity structure [67–69]. Given that the total thickness of the entire EL device is only a few atomic layers, it is promising to incorporate such devices in Fabry-Perot microcavities. This approach is widely applied in optoelectronics for engineering of the photon density of states around the emitter, which enables control of the spectral and temporal characteristics of light emission as well as its directionality. The entire EL device heterostructure is transferred onto a planar distributed Bragg reflector (DBR) and the device is completed with a second DBR which is grown on top of the device after the transfer.

7.3.1 Microcavity design

The schematic of the heterostructure and an optical microscope image of the sample is shown in Figure 7.1. Figure 7.13(a) shows the incorporation of this light-emitting diode (LED) into a microcavity structure. The DBR consists of 10 pairs of NbO_2/SiO_2 layers with thicknesses of 95 and 127 nm, respectively, to match the $\lambda/(4n)$, where n is the refractive index, condition for a center wavelength $\lambda_c = 750$ nm. The WSe_2 single quantum well EL is fabricated on top of this DBR. An identical DBR is then grown on top of the cavity in order to complete the $\lambda/2$ microcavity device. The vertical heterostructure protects the active material for this DBR growth as it is entirely covered by a hBN layer. This is required because the higher temperatures and oxygen environment would lead to a significant degradation of the active material. The design of the EL device, however, allows the fabrication of such devices embedded in microcavities. A scanning transmission electron microscope (STEM) image of the entire device is shown in the upper image of Figure 7.13(b). The bottom DBR is grown on a polished silica substrate which allows good growth

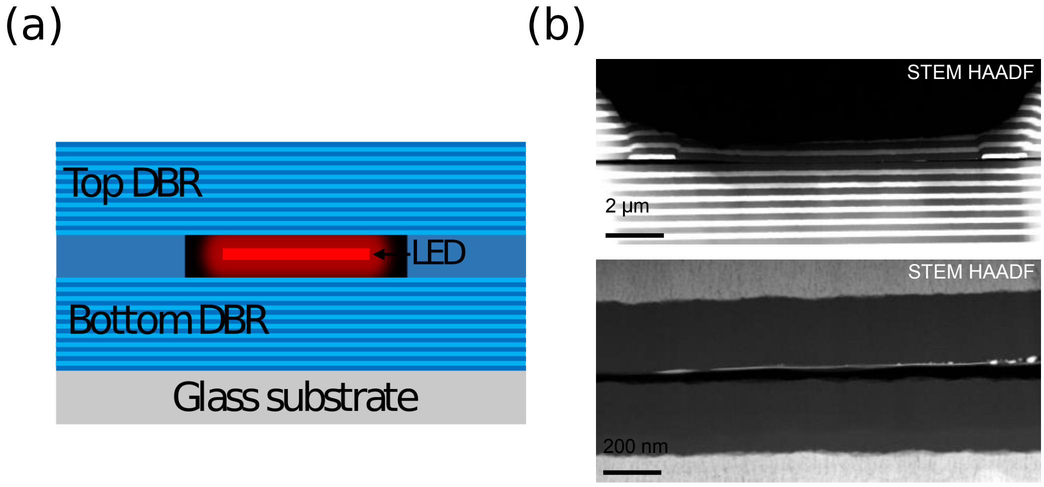

Figure 7.13: WSe_2 LED embedded in a monolithic microcavity. (a) Schematic drawing and (b) STEM image of a WSe_2 device embedded in a monolithic microcavity structure. The STEM image shows the imperfections in the growth of the top mirror, especially around the gold contacts (top handle) but also variations of the growth quality at the area of the EL device (bottom handle).

quality. The fabrication of the EL device, especially around the gold contacts, causes imperfections of the surface which results in an uneven growth of the top mirror. The bottom image of Figure 7.13(b) shows a higher magnification of the STEM image where the EL device represents the black area. The dark-grey area shows the $\lambda/2$-SiO_2 microcavity and the light-grey area shows the first NbO_2 layer of the DBR.

Optical characterization of the microcavity devices is carried out using angle resolved micro-photoluminescence and electroluminescence spectroscopy, shown in Figure 7.14. The device is placed in a flow cryostat that allows to perform experiments at different temperatures from 10 to 300 K. This setup consists mainly of a goniometer that is able to rotate the detection optics in order to collect the light emitted by the sample at different angles (θ from -30° to 30°). The excitation is carried out from the back of the sample focusing the beam on the sample with a 20-times microscope objective. The collection arm, which is in front of the sample, consists of a collection lens with a focal length of 3 cm and a pin-hole in front of it so that only a few degree of the emission is collected at each angle. This configuration also allows transmission measurements when the microcavity is excited with a white-light source.

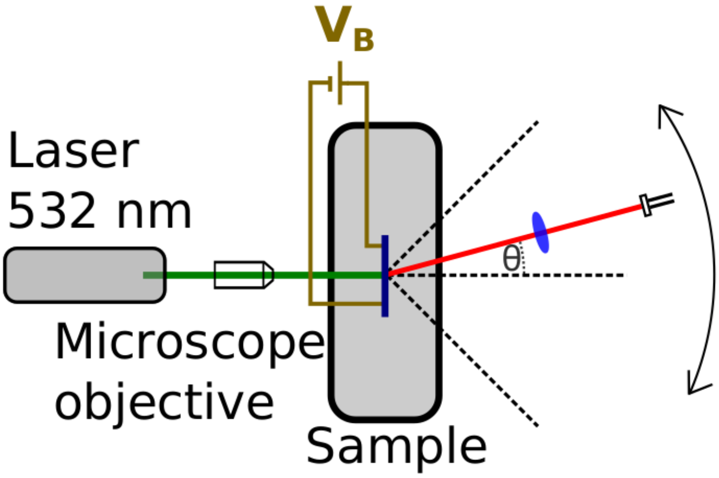

Figure 7.14: Optical setup for angle-resolved measurements. The setup consists of a goniometer which is used to rotate the detection optics. The emission can be collected at different angles, ranging from -30° to 30°.

Transmission measurements of the empty cavity at an area far away from the EL device in Figure 7.15 show a prominent cavity mode at 1.641 eV at zero degree collection angle. A Lorentzian fit of the normalized transmission degree reveals a photonic Q-factor of 980 at normal incidence. Angle-resolved measurements show the tuning of the cavity mode from 1.64 eV to 1.7 eV. The dispersion from a Fabry-Perot resonator has been discussed in chapter 3 and it can be shown that for small angles, where the small-angle approximation:

$$\cos(x) \approx 1 - \frac{x^2}{2} \tag{7.5}$$

is valid, a planar microcavity can be described with a parabolic dispersion. This will also be used in the fits for the dispersion of EL and PL in the following section.

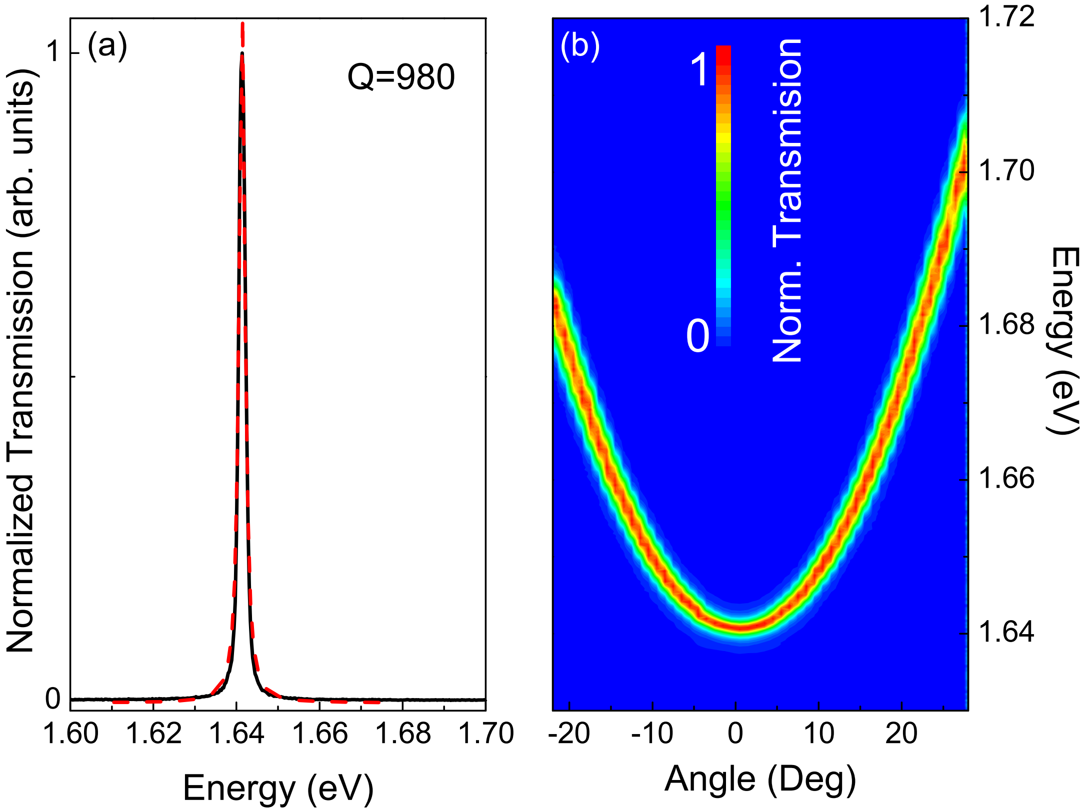

Figure 7.15: Transmission spectra of the empty microcavity. (a) The transmission spectrum shows a Q-factor of 980 at zero degree and (b) the cavity mode is tuned in a parabolic dispersion by varying the detection angle.

7.3.2 Electroluminescence in a microcavity

The EL device has been characterized before the deposition of the top DBR in order to verify electrical and optical functionality of the device. Furthermore this allows a direct comparison between the emission of the device with and without the effect of a cavity mode. Figure 7.16(a) shows EL spectra at 200K with a positive bias voltage. The EL is measured in half- and full-cavity configuration shown in black and red, respectively, where significant changes in spectral line shape are observed. While in the half-cavity device it consists of two peaks corresponding to a negatively charged exciton and localized defects in the device, it changes to a more complex pattern when top DBR is present. A narrow peak at 1.65 eV and further broader features at lower energy, of around 1.62 eV are observed. The narrow peak is attributed to the designed cavity mode, which negatively detuned from the exciton and, as such, can be tuned through the exciton energy by increasing the collection angle.

The tuning of the cavity modes is shown in Fig. 7.16(b) where the collection angle is increased from 0° to 21°. The spectra are tuned to higher energies as the collection angle is increased. A small shoulder is observed which does not tune with increasing collection angle. Furthermore, the intensity of the cavity mode is enhanced as the collection angle is tuned to 15 degrees because the cavity mode is tuned into resonance with the exciton. As the collection angle is increased further, the intensity drops as the mode is more and more positively detuned to the exciton. In order to investigate the tuning of the modes in more detail the peak positions of the features are presented in Fig. 7.16(c), where two 2D cavity modes are observed, which follow the expected parabolic dispersion of the planar cavity device. These two 2D cavity modes correspond to the cavity areas with and without the EL device since its presence causes a local increase in the optical cavity length. The 2D cavity mode separation of 16 meV corresponds to a change in cavity length of 6 nm which agrees with the fabricated device height of several nanometers. A cavity mode outside the EL device is observed because of a so-called 'walk-off' of the cavity mode, which commonly occurs when the mirrors are not perfectly parallel. Variations of the cavity thickness around the EL device, as well as the imperfections around the gold contacts, create photonic defects resulting in a confinement of the cavity mode in the lateral direction. This confinement leads to an additional quantization of the photonic states [170].

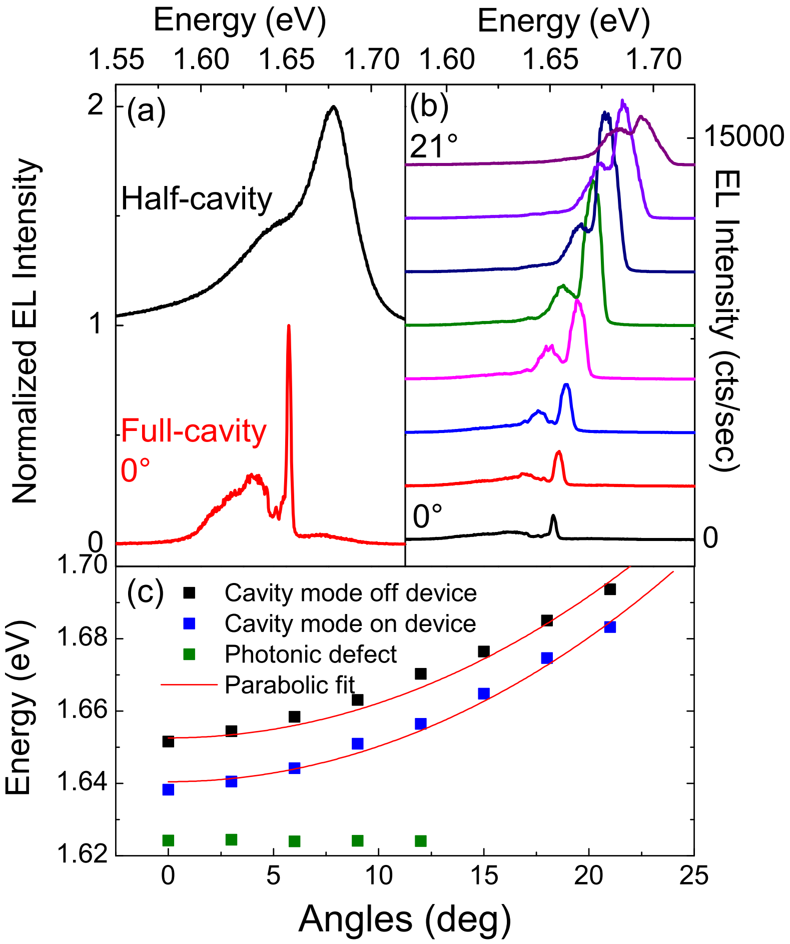

Figure 7.16: EL coupled to the microcavity. (a) EL spectra before (black) and after (red) deposition of the top DBR. (b) Angle-dependent collection of EL shows the tuning of the cavity mode as a function of collection angle. (c) The peak positions of the features can be fitted by two parabolic cavity modes, corresponding to the cavity modes which are formed on and off the area of the EL device. Photonic defects lead to a confinement in all three dimensions where a flat dispersion is observed.

Photonic defects in the microcavity, present due to the poor DBR growth around the gold contacts, result in a quantized dispersion of the cavity mode due to the strong lateral confinement as shown in Figure 7.16(c). The STEM image in Figure 7.13 shows the variation of the cavity length and the step-like growth of the top DBR around the gold contacts. The angular spread of the mode corresponds to a dimension in the momentum space which is obtained by the projection of the wave vector:

$$k = \frac{2\pi}{\lambda} \sin\theta, \tag{7.6}$$

where λ is the wavelength of the mode and θ is the angle to which the cavity mode extends to. Here, the localized cavity mode extends to an angle of approximately 15 degrees. The spatial Fourier transformation of the momentum space into real-space allows to extract the physical dimension of the photonic defect. The size of the defect calculates as $r = 1.84\mu$m, which corresponds to the lateral size of the gold contacts near the EL device.

Similar behaviour is observed in the case of the PL experiment at the same temperature at 200K. Figure 7.17(a) shows the PL spectra before (black curve) and after (red curve) top DBR deposition, where variation in spectra pattern is observed. The peak in the black curve corresponds to a negatively charged exciton. The effect of localized states is minimized in PL because while the emission from EL stems from the entire device, the PL is coming from a small spot, which is excited by the laser. The two main peaks at 1.65 and 1.62 eV in the red curve arise from 2D and confined cavity modes respectively as explained earlier. Angle dependence of PL is presented in Figure 7.17(b). The observed angle dependence shows again the designed cavity mode and additional cavity modes coming from the cavity mode outside the device and photonic defects. Although only a small spot is excited in PL, the cavity mode is still extended over a larger area in the full-cavity device. This can be explained due to the walk-off of the cavity mode, as mentioned above. Therefore, even though less defect states are observed for the half-cavity device, the contribution of the localized mode and the mode off the EL device are comparable to the EL experiment in the full-cavity device.

The full temperature and angle dependence of EL can be analysed as an integrated normalized intensity map as a function of both parameters. This is presented in Figure 7.18.

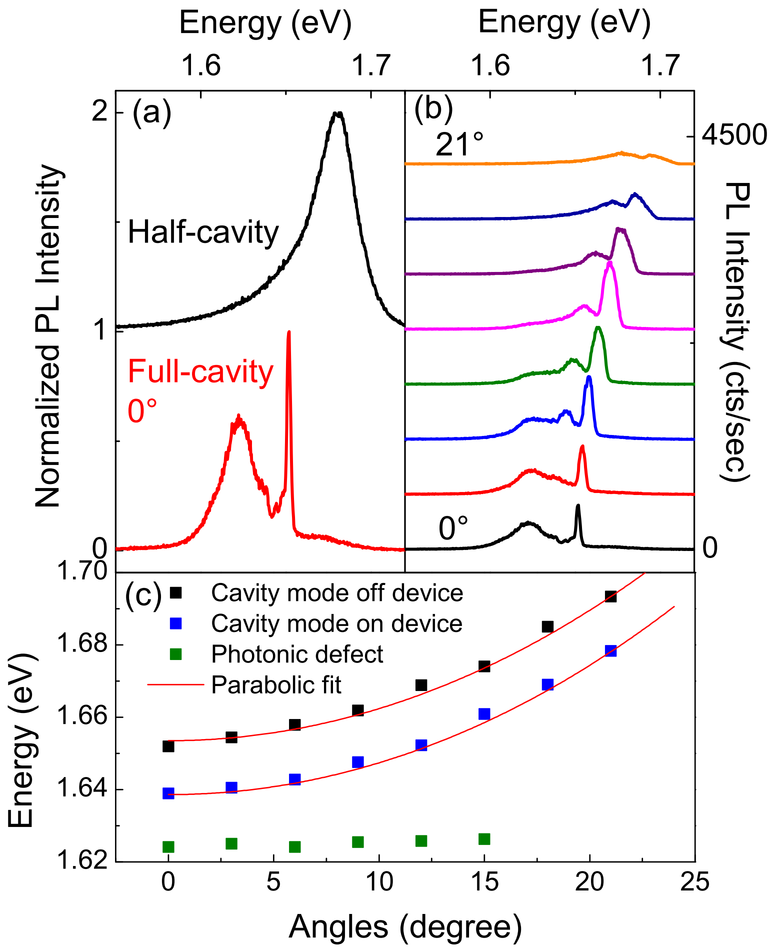

Figure 7.17: PL coupled to the cavity mode at 200K. (a) Comparison of the PL spectra before (black) and after (red) deposition of top DRB showing a similar behavior as in EL. (b) Angle dependent measurements of PL show again the parabolic tuning of the PL.

The exciton energy shifts from 1.66 eV at 4.2K to 1.58 eV at room temperature. Apart from the red-shift of the exciton energy with increasing temperature, a broadening of the exciton is shown and the shoulder, attributed to localized defects, thermalizes and is no longer observed at room temperature. At room temperature the integrated EL intensity reaches the maximum around 10°. As the temperature decreases and the exciton energy shifts, the cavity mode is in resonance with the EL at larger angles where the maximum of the intensity is observed at angles up to 25° at T=50K.

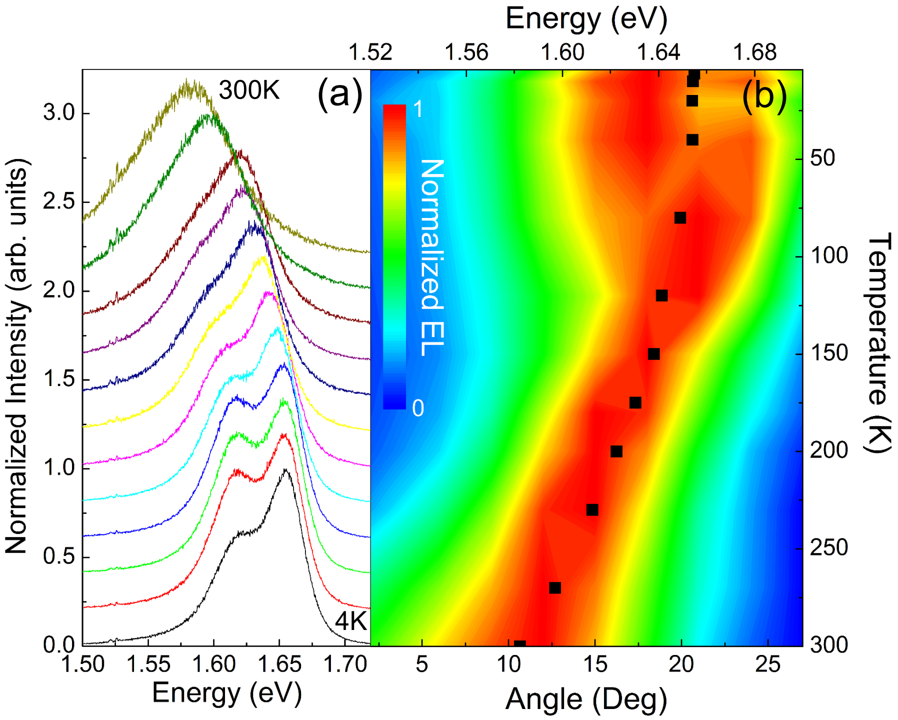

Figure 7.18: Normalized EL intensity as a function of angle and temperature. (a) The temperature dependence of the EL in the half-cavity configuration shows the red-shift of the exciton energy with increasing temperature. (b) The exciton is tuned closer to resonance with the cavity mode as the temperature is increased causing the maximum of the EL intensity to be observed for smaller angles. The peak position of the exciton is marked with the black squares.

The Purcell enhancement of a cavity mode corresponds to the enhanced spontaneous emission rate caused by the microcavity when the cavity mode is in resonance to the exciton due to the change in the photonic density of states. In the case of strongly inhomogeneously broadened emitters such as WSe_2, for example, where the exciton linewidth is spectrally broader than the cavity linewidth, only the spectral slice which is in resonance with the cavity mode is affected by the Purcell enhancement. Therefore spectral and spatial averag-

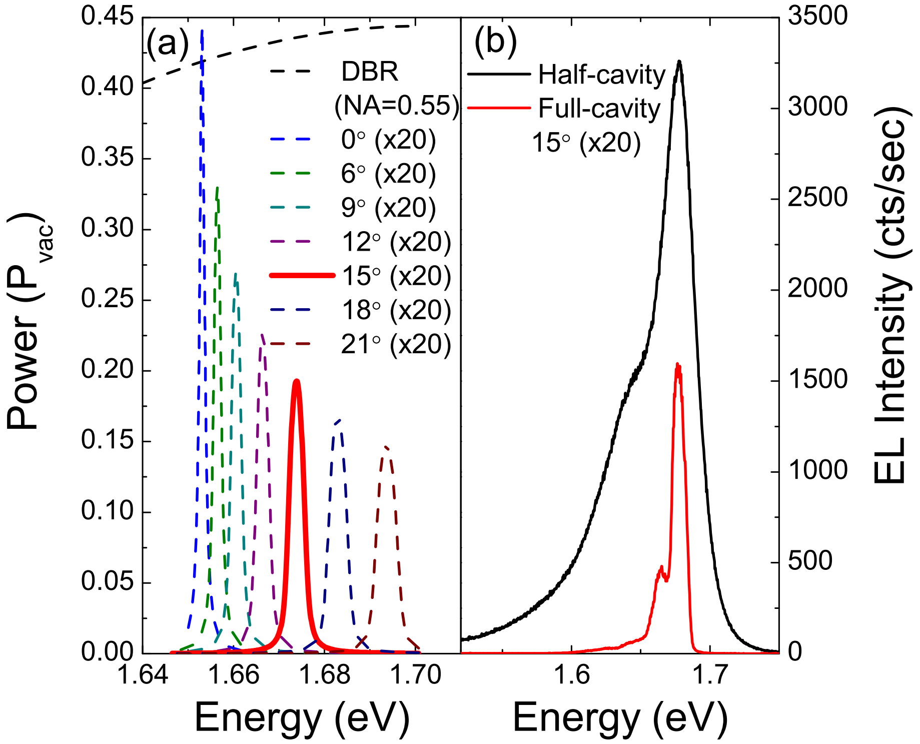

Figure 7.19: Angle dependent emission density. (a) The black dashed curve shows the emission pattern for a dipole sitting on the bottom DBR. The cavity mode is tuned in energy by changing the collection angle. (b) At 15 degrees the cavity mode is in resonance with the exciton.

ing over the emitter is required in order to calculate the Purcell enhancement. Numerical simulations of the cavity structures reveal a Purcell enhancement of the order of unity. A change of the observed intensity is therefore a purely geometrical effect, which will be discussed in the following. Figure 7.19(a) shows the comparison of the emission collected from the half- and full cavity respectively. The black dashed line corresponds to the emission of the half-cavity device and the emission of the cavity mode at different angles is shown in the different colored lines. The highlighted line corresponds to the angle where the cavity mode is in resonance with the exciton in order to compare the simulation with the experimental results in Figure 7.19(b).

First of all, in the experiment a finite Δk, corresponding to an angular span of 1.4 degrees, is measured. At larger angles, the parabolic dispersion $E(k)$ is steeper, and therefore a larger ΔE is measured for the same Δk, which explains the broadening of the collected mode at larger collection angles in Figure 7.19. The EL device in the half-cavity configuration

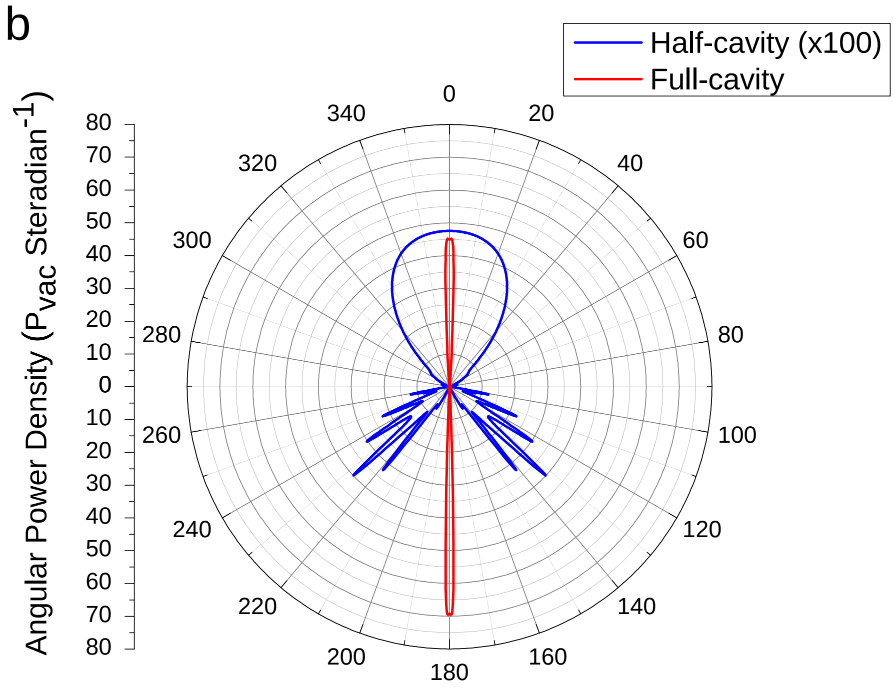

Figure 7.20: Comparison of the angular distribution. The angular distribution of the half- and full-cavity configuration shows that the emission is forced into a much tighter angle in the full-cavity device allowing a more efficient collection.

is characterized in a standard micro-PL setup where a micro-objective with a numerical aperture of NA=0.55 is used. In this setup the entire angular span of approximately ±35 degrees is collected at the same time, which results in a higher collection efficiency of the setup compared to the angle-resolved setup where a lens with a numerical aperture of NA=0.0125 is used. From the different collection optics it is expected to collect a factor of 2000 less emission in the angle-resolved setup. The simulation, however, shows that only a factor of 20 less light is collected in the full-cavity configuration, when the emission from the half-cavity and full-cavity is compared at zero degrees. The discrepancy comes from the fact that the angular distribution of the emission is directed into smaller angles due to the DBR on top of the EL device. This is shown in Figure 7.20, where the angular distribution of the half- and full-cavity configuration is compared. It shows that if both devices are measured in the angle-resolved setup, the full-cavity device leads to a 100 times increase of the collection efficiency.

Finally, the sample design enables to use this device as a photodetector. In the experiment, a tunable laser is coupled into the collection path, allowing angle- and wavelength-dependent excitation of the sample. By changing the excitation angle, the cavity mode is again tuned and the maximum of the photocurrent is observed at a different energy, accordingly. This device, therefore, operates as a tunable photodetector, where a detection wavelength can be designed by the microcavity. Figure 7.21(a) shows spectra of the measured photocurrent for different excitation angles demonstrating this tunability. The photocurrent is increased when the cavity mode is in resonance with the exciton. This is achieved for an excitation angle of 12 degrees, where a photocurrent of up to 5 nA is measured where an excitation laser power of 1 nW is used as shown in Figure 7.21(b). The device is operated at a low forward bias of $V_B = 0.1$ V, where a dark current of 0.5 nA is measured. The responsivity R is defined as the output signal divided by the input power. In a photodetector the responsivity given by:

$$R = \eta \frac{e}{hc} \lambda, \tag{7.7}$$

where $e = 1.602 \times 10^{-19}$ As is the elementary charge, $h = 6.626 \times 10^{-34}$ Js is the Planck constant, $c = 2.9979 \times 10^{8}$ m/s is the speed of light, λ is the detection wavelength and η is the quantum efficiency. The measured photo current $I_{ph} = 50$ nA at an excitation power of $P_{exc} = 1nW$ leads to a responsivity of $R = I_{ph}/P_{exc} = 5 \times 10^{-3}$ A/W at an excitation energy of 1.66 eV. The total quantum efficiency therefore is $\eta = 4.15\%$. One should note, that this quantum efficiency is relatively low. However, the device was not optimized to operate as a photodetector. Additionally the experimental setup could be optimized and losses in the setup are not included, which means the estimated quantum efficiency is a lower limit. At the cost of a higher dark current, the responsitivity could be increased by increasing the forward bias of the device. Furthermore, improvement of the device quality and optimizing the tunneling barriers may lead to significant increase in the quantum efficiency.

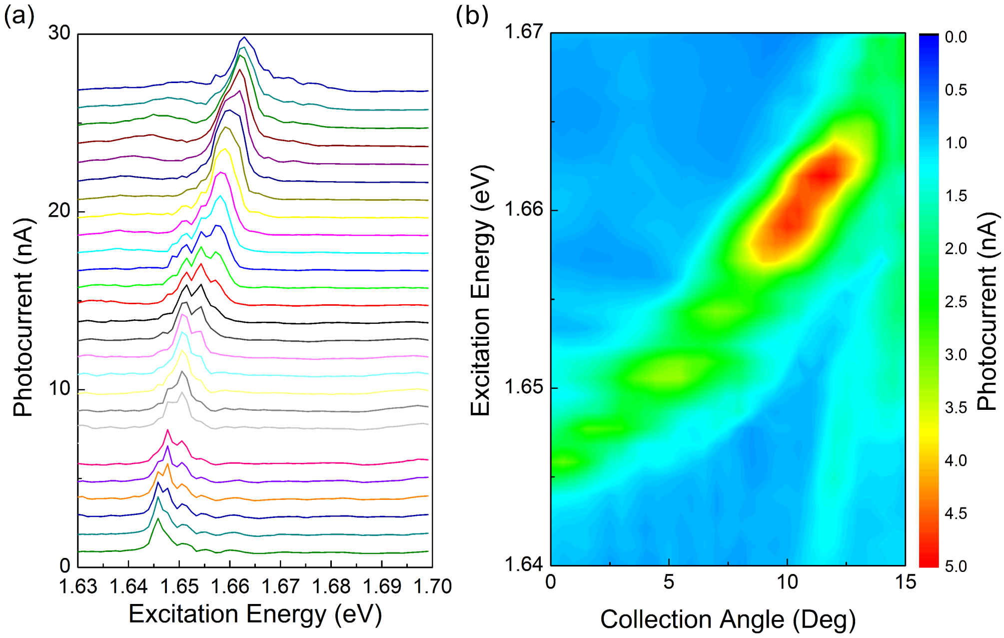

Figure 7.21: Angle-dependent photocurrent measurements. The device can also be used as a tunable photodetector, where the detection wavelength is tuned by the angle of incidence. This tunability is shown (a) as individual spectra for different angles and (b) as colorplot showing the parabolic dispersion of the cavity mode.

7.4 Summary

In summary, EL and PL from atomically thin light-emitting diodes based on vertically stacked van der Waals heterostructures coupled to cavity modes in monolithic microcavity devices have been demonstrated. PL and EL characterization of WSe_2 allows a clear identification of the different features in the spectrum. Polarization dependent measurements show a strong linear polarization of the quantum dot-like states while strong circular polarization is observed in the excitonic features. Magnetic field measurements are performed in order to extract the valley Zeeman splitting of the exciton features. The emission is coupled to narrow cavity modes with Q-factors of around 1000. Different types of modes are observed, which arise due to the present of the device, leading to vertical cavity modes on and off the area of the device, as well as additional cavity modes stemming from photonic defects caused by imperfections in the fabrication process. These devices are the first electrically pumped 2D materials embedded in microcavity structures and serve as a prototype for further investigation towards lasing devices. Improvement of the fabrication quality as well as growth of dielectric layers on top of van der Waals crystals and gold contacts may lead to an attractive avenue towards vertical-cavity surface-emitting lasing devices (VCSELs). The increased directionality of the emission in the device is a promising feature in order to guide the emission in a more controlled way. An additional advantage here is the use of graphene as a transparent electrode, which allows uniform current injection across the whole surface of the device. Furthermore, the device layout allows electrostatic tuning of the exciton features.

8 Conclusion

In this work the optical properties of van der Waals crystals with thicknesses down to single atomic layers are investigated and light-matter interaction in such two-dimensional layers embedded in microcavity structures are investigated. Out of the large number of van der Waals crystals, transition-metal dichalcogenides (TMDCs) appear to be the most promising candidate for opto-electronic devices. A tunable open-access microcavity has been used to study MoS_2 and GaSe in the weak coupling regime, where a Purcell enhancement has been observed. Strong exciton-photon coupling with large Rabi splitting of 20 meV has been observed in $MoSe_2$. The tunability of this microcavity design serves as an ideal system to study the light-matter interaction. Towards opto-electronic applications, however, monolithic cavity devices are desired, which are studied in the final part of this thesis. Vertically stacked van der Waals heterostructures allow to produce electrically pumped light-emitting devices. These atomically thin devices are embedded in a microcavity in order to couple the electroluminescence to narrow cavity modes.

8.1 Results

Weak coupling of MoS_2 and GaSe in a tunable microcavity

A tunable open-access microcavity system has been developed to have more freedom and control over the light-matter interaction of 2D materials and the cavity. The main advantage of this system compared to monolithic microcavity devices is the tunability of the cavity mode by simply changing the separation of the two mirrors. In this system monolayer sheets of MoS_2 and thin films of GaSe have been studied in the weak coupling regime. A PL enhancement up to 60 has been shown, which stems from a combination of a Purcell enhancement and a geometric effect, where the emission of the monolayer is redirected into a smaller angle. Due to the presence of the top mirror, and the formed cavity mode, more directionality in the emission pattern is observed, which results in a larger collection efficiency in the optical setup. After considering this effect, a Purcell enhancement of around 12 is estimated for MoS_2 films where a direct evidence via time-resolved measurements is not possible because the carrier lifetime is dominated by non-radiative processes. In localized states of GaSe, however, the radiative lifetime is comparable to the non-radiative lifetime. Therefore, when these states are coupled to the cavity, a reduced carrier lifetime is observed due to the enhanced spontaneous emission rate and a Purcell enhancement of 10 is obtained in GaSe sheets.

Strong exciton-photon coupling in van der Waals heterostructures

Light-matter interaction was studied in hBN/MoSe2 heterostructures placed in tunable microcavities. Both, single- and double-QW structures of the form hBN/MoSe2 and hBN/-MoSe2/hBN/MoSe2 are studied, respectively. $MoSe_2$ has been selected for this experiment because higher emission efficiency and narrower linewidth are observed in $MoSe_2$ compared to other TMDCs. It was possible to observe the strong exciton-photon coupling regime with single and double quantum well structures. In a single monolayer structure, the clear anti-crossing between the cavity modes and the neutral exciton with a Rabi splitting of 20 meV allows to resolve both polariton branches at resonance. By increasing the number of QWs, the Rabi splitting can be increased, which is demonstrated for the double QW where a Rabi splitting of 29 meV has been observed. This allows to scale the Rabi splitting so that in future strong light-matter interaction may be observed at room temperature in heterostructures with an increased number of QWs. However, with the increasing number of QWs the total thickness of the structure will also increase, leading to displacement of the QWs from the antinode of the cavity mode, and resulting in a reduced light-matter interaction.

Electroluminescence devices in microcavities

Vertically stacked heterostructures consisting of graphene contacts, hBN as tunnel barriers and TMDCs as active material, have been fabricated in order to produce electroluminescence devices. These EL devices are embedded in monolithic microcavities where the EL from the device is strongly modified by the cavity. WSe_2 was found to be an interesting material for room temperature applications because in WSe_2 the quantum efficiency was found to increase with increasing temperature. This is due to the ordering of dark and bright exciton sub-bands, where the dark excitons are the lower energy states and thus are populated first at cryogenic temperatures. The incorporation of such devices showed first results of light-matter interaction where a significant change of the spectral emission pattern, as well as the emission directionality, has been observed. Angle-resolved measurements showed evidence that the EL device is coupled to the microcavity structure. This is the first demonstration of electrically pumped devices, based on 2D materials, embedded in microcavity structures.

8.2 Outlook

The obtained results are promising for many follow-up experiments. The ability to produce vertically stacked heterostructures on arbitrary substrates allows for a flexible sample design for various opto-electronic devices. Because this research area is still emergent, there are a lot of details on the physical properties of TMDCS still not unravelled. Looking at the emission spectra of WSe_2, for example, shows that the origin of some feature are still not clear. Due to the inhomogeneous broadening and extremely short carrier lifetime, detailed studies on spectral features, as well as their dynamics, are difficult. One of of the most striking properties of TMDCs is the valley polarization caused by the large spin-orbit coupling. In this work a large valley-polarization degree of almost 70% is achieved for non-resonant excitation. The polarization degree as a function of the magnetic field reveals further interesting properties as shown in Figure 8.1. In case of the neutral exciton the formation of σ^- exciton is favorable for B>0T, while σ^+ formation is more favorable for B<0T because of the magnetic tuning. Therefore the valley polarization degree is larger for the higher energy exciton. This is the opposite of what is expected for thermal relax-

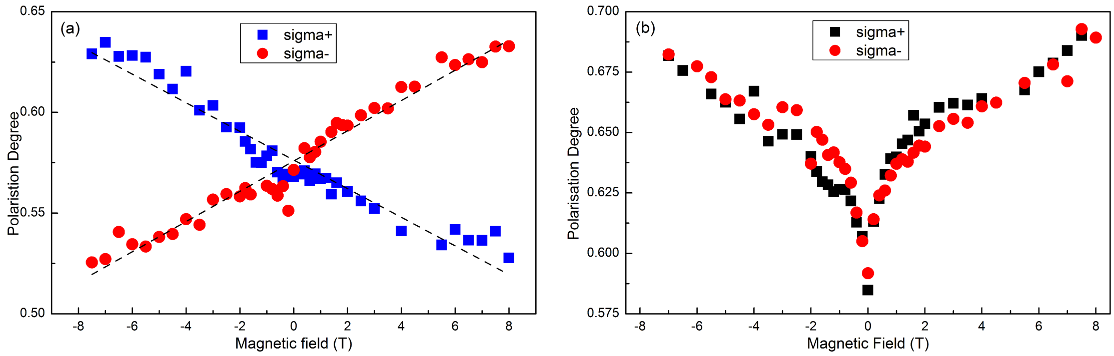

Figure 8.1: Polarization degree as a function of the magnetic field. The degree of valley-polarization for (a) the neutral exciton and (b) the charged exciton shows a significant difference for the two exciton complexes.

ation, which allows to conclude that the polarization degree of X^0 is determined during the exciton formation.

The negatively charged trion is formed with an additional electron in the conduction band and there are four possible configurations to form a bright trion as demonstrated in Figure 8.2. The additional electron is occupying either the spin-split conduction band in the same valley or the corresponding spin-flipped state of the conduction band in the other valley. In the latter case, an exchange energy has to be overcome in order to allow inter-valley scattering. The polarization dependent measurements of the charged exciton shown in Figure 8.1(b), together with the corresponding valley Zeeman splitting discussed in chapter 7 may allow to extract the inter-valley exchange energy. At first, the Zeeman splitting is less than the exchange energy and a rapid increase of the polarization degree is observed when the magnetic field is tuned from 0T to ±1T. This is due to the valley Zeeman splitting which breaks the energy degeneracy of the charged exciton leading to a suppression of the valley relaxation. For higher magnetic fields the Zeeman splitting exceeds the value of the exchange energy and the transition of the additional electron from one valley to the other is suppressed. This may be the first experimental demonstration of the intervalley-exchange energy but further experimental data and theoretical support is required to fully understand the observed development of the polarization degree.

Following from the first demonstration of electrically pumped devices embedded in micro-cavity structures and the observation of strong light-matter interaction offers a variety of avenues that are pursued following this work.

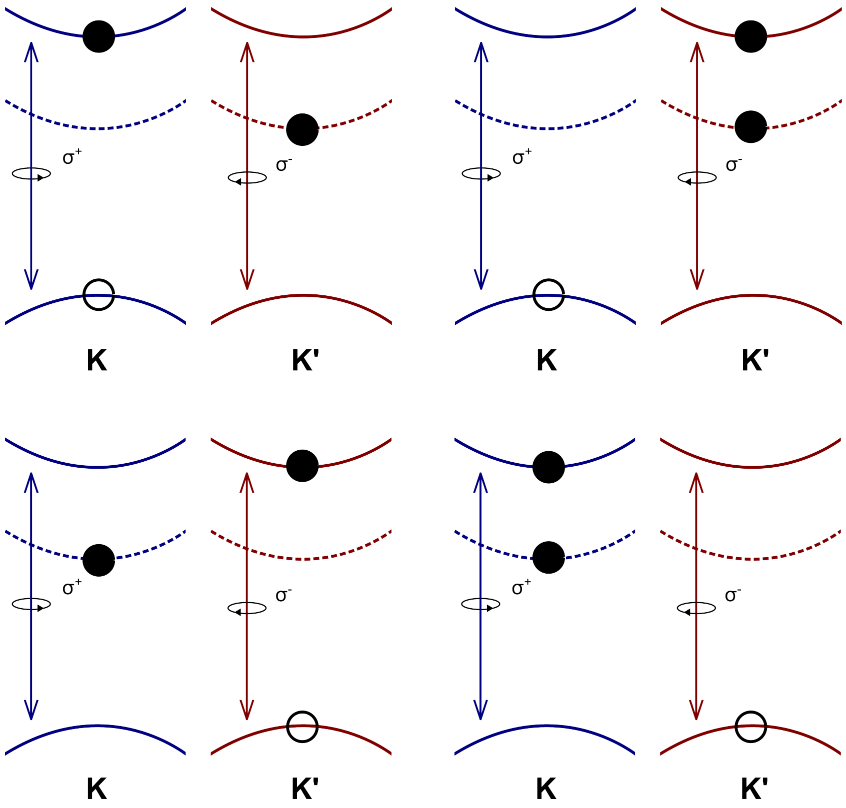

Figure 8.2: Schematic of the formation of a negatively charged trion. There are four configurations to form a negatively charged trion. If the additional electron is not in the same valley, inter-valley scattering processes occur only when an exchange energy is overcome.

8.2.1 Electrically pumped lasing devices

A key factor towards opto-electronic devices in any novel material is the development of reliable detectors and reliable sources. In order to produce photonic circuits a coherent light source is required. A typical way to produce such a source is to fabricate a laser based on stimulated emission. While PL stems from a stochastic process, the spontaneous emission, a stimulated emission produces photons which are indistinguishable in frequency, phase, polarization and direction and as such a coherent source. The concept of lasers has been introduced in 1917 [171] and in 1928 the existence of stimulated emission and negative absorption has been demonstrated [172] but the first functioning laser was demonstrated in 1960 [173]. Nowadays many principles and techniques are used to produce lasing devices. Recently the first optically pumped lasing devices based on 2D materials have been demonstrated. One based on a WSe_2 monolayer sheet, placed on a photonic crystal nano-cavity [66], the other one relies on whispering gallery modes in micro-disk resonators [68, 69]. While both approaches show signatures of photonic lasing, so far no electrically pumped lasing device has been demonstrated. A vertically stacked heterostructure embedded in a microcavity structure, as demonstrated in this work, is a promising candidate for the observation of electrically pumped lasing. So far the losses in the sample exceed the gain so that the lasing threshold could not be reached in this work.

8.2.2 Bose-Einstein condensation

The observation of strong exciton-photon coupling with resolved polariton branches allows the study of non-linear effects of the polariton system. Polaritons are bosonic quasi-particles and, therefore, obey Bose-Einstein statistics. In integer-spin bosons the symmetric wavefunction leads to constructive interference of the probability that particles are located in the same state. This so-called bosonic stimulation is possible for polaritons leading to macroscopic occupation of the ground LPB state at $k = 0$. This effect is known as polariton condensation. Bose-Einstein condensation has been proposed in 1925 [175], after initial studies on massless Bose particles in 1924 [174]. The Bose-Einstein condensation arises from the quantum statistics of Bose particles and leads to the occupation of the lowest quantum state. The first experimental demonstration of Bose-Einstein condensation was on dilute gases in 1995 [176, 177]. Subsequently it was proposed that exciton-polaritons

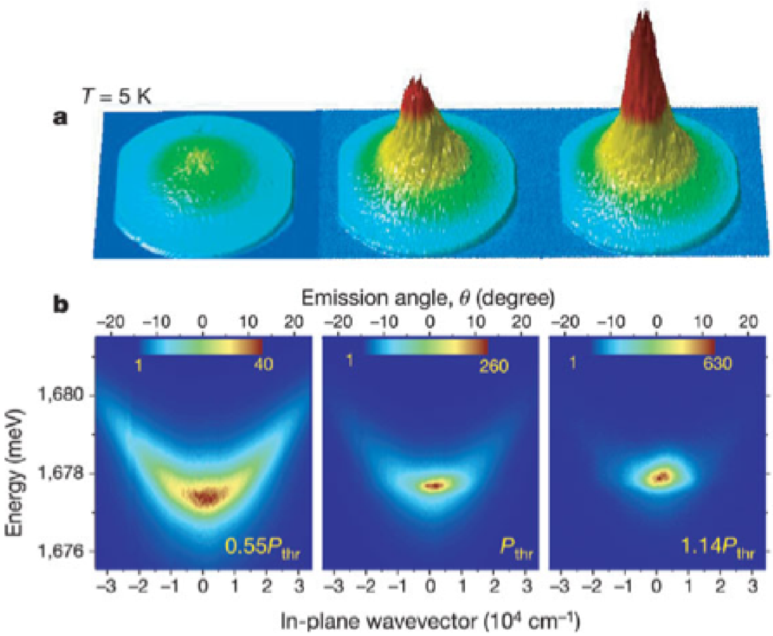

Figure 8.3: Demonstration of polariton condensation. The far-field emission for three excitations, 0.55P$_{thr}$, P$_{thr}$ and 1.14P$_{thr}$, is shownin (a) a 3D emission pattern and (b) resolved in energy to display the dispersion of the cavity. Above the threshold power the lowest energy, around $k = 0$, is populated. Figure taken from [58].

offer a great platform for the observation of Bose-Einstein condensation. First, the very low effective mass from their photonic contribution allows the observation of condensation at easier accessible temperatures. Secondly, due to the spacial extended wavefunctions the condensation is expected to be more robust against localization and inhomogeneous broadening. The first experimental demonstration of polariton condensation is shown in the famous plot in Figure 8.3 [58]. Above the threshold power the emission is confined around $k = 0$ and long range spatial coherence was observed above the threshold power. Polariton condensation has also been observed at room temperature in wide bandgap materials, ZnO and GaN, and organics [148, 178–181]. Due to the inherited long spatial coherence, polariton condensation offers the opportunity to observe polariton lasing. TMDCs appear to be a promising candidate to observe room temperature polariton condensation, also for easier accessible wavelengths, where ultra-low threshold lasing devices may lead to a new, promising opto-electronic application.

8.2.3 Charged polaritons

The PL spectrum of $MoSe_2$ showed the clean emission of a neutral and charged exciton. Electrostatic tunability of the exciton charging has been demonstrated using a back-gated field-effect transistor [152]. The electric control allows a conversion of the neutral exciton with addition of an electron (hole) in the form of: $e(h) + X^0 \rightarrow X^- \ (X^+)$. It has been shown that, at reasonable gate voltages, the intensity of the neutral exciton can be neglected compared to the intensity of the charged exciton. With respect to the observation of strong light-matter interaction in this work, this is very interesting. In previous systems polariton in charged states have been demonstrated, but always accompanied with neutral excitons, whereas in TMDCs the possibility of purely trion-polariton states are possible. The Rabi splitting in this work was 20 meV for the neutral exciton and only a few meV for the charged exciton. However, due to the preservation of the oscillator strength, it is expected that the Rabi splitting is transferred from the neutral to the charged exciton when the sample is gated. This would allow the observation of a clear Rabi splitting for positively or negatively charged trion states, depending on the gate voltage. When the vacuum Rabi splitting is larger than the trion binding energy an incident photon results in the formation of a polariton with an additional electron cloud, much bigger than the Bohr radius. This may lead to enhanced polariton-polariton interaction which allows easier access to the non-linear regime [182].

Bibliography

[1] Novoselov K. S., *et al.*, Electric Field Effect in Atomically Thin Carbon Films, *Science* **5**, Vol. 306, no. 5696, 666-669 (2004)

[2] Novoselov, K. S. *et al.* Two-dimensional atomic crystals, *PNAS* **102** 10451-10453 (2005)

[3] Wallace P. R., The Band Theory of Graphite, *Phys. Rev. Lett.* **71**, 662 (1947)

[4] Novoselov K. S., *et al.*, Room-Temperature Quantum Hall Effect in Graphene, *Science* **9**, Vol. 315, no. 5817, 1379 (2007)

[5] Geim A. K. & Novoselov K. S., The rise of graphene, *Nat. Mat.* **6**, 183-191 (2007)

[6] Elias D. C., *et al.*, Dirac cones reshaped by interaction effects in suspended graphene, *Nat. Phys.* **7**, 701-704 (2011)

[7] Bolotin K. I., *et al.*, Ultrahigh electron mobility in suspended graphene, *Solid State Comm.* **146**, 351-355 (2008)

[8] Canali C., *et al.*, Electron drift velocity in silicon, *Phys. Rev. B* **12**, 2265-2284 (1975)

[9] Schwierz F., Graphene transistors, *Nat. Nano.* **4**, 487-496 (2010)

[10] Yi M., & Shen Z., Review on mechanical exfoliation for the scalable production of graphene, *J. Mater. Chem. A* **3**, 11700-11715 (2015)

[11] Geim A. K., & Grigorieva I. V., Van der Waals heterostructures, *Nature* **499** 419-425 (2013)

[12] Watanabe K., *et al.*, Direct-bandgap properties and evidence for ultraviolet lasing of hexagonal boron nitride single crystal, *Nat. Mat.* **3** 404-409 (2004)

[13] Song L., *et al.*, Large Scale Growth and Characterization of Atomic Hexagonal Boron Nitride Layers, *Nano Lett.* **10** 3209-3215 (2010)

[14] Arnaud B., *et al.*, Huge Excitonic Effects in Layered Hexagonal Boron Nitride, *Phys. Rev. Lett.* **96** 026402 (2006)

[15] Dean C. R., *et al.* Boron nitride substrates for high-quality graphene electronics, *Nature Nanotech.* **5** 722-726 (2010)

[16] Britnell L., *et al.*, Electron Tunneling through Ultrathin Boron Nitride Cyrstalline Barriers, *Nano Lett.* **12(3)** 1707-1710 (2012)

[17] Britnell L., *et al.*, Field-Effect Tunneling Transistor Based on Vertical Graphene Heterostructures, *Science* **24** Vol. 335, no. 6071, 947-950 (2012)

[18] Yankowitz M., *et al.*, Emergence of superlattice Dirac points in graphene on hexagonal boron nitride, *Nat. Phys.* **8** 382-386 (2012)

[19] Woods C. R., *et al.*, Commensurate-incommensurate transition in graphene on hexagonal boron nitride, *Nat. Phys.* **10** 451-456 (2014)

[20] Del Pozo-Zamudio O., *et al.*, Photoluminescence and Raman investigation of stability of InSe and GaSe thin films, *arXiv:*1506.05619 (2015)

[21] Cao Y., *et al.*, Quality heterostructures from two dimensional crystals unstable in air by their assembly in inert atmosphere, *Nano Lett.* **15(8)** 4914-4921 (2015)

[22] Kim J.-S., *et al.*, Toward air-stable multilayer phosphorene thin-films and transistors, *Scient. Rep.* **5** 8989 (2015)

[23] Brudnyi A. I., *et al.*, Structure of molybdenum disulphide lubricant film, *Wear* **33(2)** 243-249 (1975)

[24] Mak K. F., *et al.*, Atomically Thin MoS_2: A New Direct-Gap Semiconductor, *Phys. Rev. Lett.* **105** 2-5 (2010)

[25] Splendiani A., *et al.*, Emerging photoluminescence in monolayer MoS_2, *Nano Lett.* **105** 101901 (2014)

[26] Tonndorf P., *et al.*, Photoluminescence emission and Raman response on monolayer MoS_2, $MoSe_2$ and WSe_2, *Opt. Exp.* **21(4)** 4908-4916 (2013)

[27] Guitérrez H. R., *et al.*, Extraordinary Room-Temperature Photoluminescence in Triangular WS_2 Monolayers, *Nano Lett.* **13(8)** 3447-3454 (2013)

[28] Yan T., *et al.*, Photoluminescence properties and exciton dynamics on WSe_2, *Appl. Phys. Lett.* **10(4)** 1271 (2010)

[29] Wang Q. H., *et al.*, Electronics and optoelectronics of two-dimensional transition metal dichalcogenides, *Nat. Nano.* **7(11)**, 699-712 (2012)

[30] Radislavjevic B., *et al.*, Single-layer MoS_2 transistors, *Nat. Nano.* **6(3)**, 147-150 (2011)

[31] Kormánoys A., *et al.*, Spin-Orbit Coupling, Quantum Dots, and Qubits in Monolayer Transition Metal Dichalcogenides, *Phys. Rev. X* **4**, 011034 (2014)

[32] Wang Q. H., *et al.*, Electronics and optoelectronics of two-dimensional transition metal dichalcogenides, *Nature Nanotech.* **7** 699-712 (2012)

[33] Chernikov A., *et al.*, Exciton Binding Energy and Nonhydrogenic Rydberg Series in Monolayer WS_2, *Phys. Rev. Lett.* **113** 076802 (2014)

[34] Hanbickl A. T., *et al.*, Measurement of high exciton binding energy in the monolayer transition-metal dichalcogenides WS_2 and WSe_2, *Sol. State. Comm.* **203** 16-20 (2015)

[35] Hill H. M., *et al.*, Observation of Excitonic Rydberg States in Monolayer MoS_2 and WS_2 by Photoluminescence Excitation Spectroscopy, *Nano Lett.* **15(5)** 2992-2997 (2015)

[36] Mak K. F., *et al.*, Tightly bound trions in monolayer MoS_2, *Nat. Mat.* **12**, 207-211 (2013)

[37] Xiao D., *et al.*, Coupled spin and valley physics in monolayer of MoS_2 and other group-VI dichalcogenides, *Phys. Rev. Lett.* **108**, 196802 (2012)

[38] Zeng H., *et al.*, Valley polarization in MoS_2 monolayer by optical pumping, *Nat. Nano.* **7**, 490-493 (2012)

[39] Mak K. F., *et al.*, Control of valley polarization in monolayer MoS_2 by optical helicity, *Nat. Nano.* **7**, 494-498 (2012)

[40] Srivastava A., *et al.*, Optically active quantum dots in monolayer WSe_2, *Nat. Nano.* **10(6)**, 491-496 (2015)

[41] Chakraborty C., *et al.*, Single quantum emitters in monolayer semiconductors, *Nat. Nano.* **10(6)**, 507-511 (2015)

[42] Koperski M., *et al.*, Single photon emitters in exfoliated WSe_2 structures, *Nat. Nano.* **10(6)**, 503-506 (2015)

[43] Srivastava A., *et al.*, Voltage-controlled quantum light from an atomically thin semiconductor, *Nat. Nano.* **10(6)**, 491-496 (2015)

[44] Mudd G. W., *et al.*, Tuning the Bandgap of Exfoliated InSe Nanosheets by Quantum Confinement, *Adv. Mat.* **25(40)**, 5714-5718 (2013)

[45] Rodriguez R. D., *et al.*, Selective Raman modes and strong photoluminescence of gallium selenide flakes on sp^2 carbon, *J. Vac. Sci, Techn. B* **32**, 04E106 (2014)

[46] Del Pozo-Zamudio O., *et al.*, Optical properties of two-dimensional gallium chalcogenide films, *arXiv*:1501.02214 (2015)

[47] Catalano I. M., *et al.*, Luminescence and photocurrent of gallium sulphide, *Phys. Stat. Sol.* **20(2)** K135-K138 (1973)

[48] Liu H., *et al.*, Phosphorene: An Unexplored 2D Semiconductor with a High Hole Mobility, *ACS Nano* **8(4)** 4033-4041 (2014)

[49] Abdullaev G. B., *et al.*, Spontaneous and stimulated emission from electron-beam-excited gallium selenide, *Sov. J. of Quantum Elect.* **4** 80 (1974)

[50] Yao S. S., *et al.*, Photoluminescence spectra of the layered semiconductor gallium selenide under intense picosecond laser-pulse excitation, *Phys. Rev. B* **27** 2439 (1983)

[51] Xi X., *et al.*, Strongly enhanced charge-density-wave order in monolayer $NbSe_2$, *Nat. Nano.* **10** 143 (2015)

[52] Teweldebrhan D., *et al.*, Exfoliation and Characterization of Bismuth Telluride Atomic Quintuples and Quati-Two-Dimensional Crystals, *Nano Lett.* **10** 1209-1218 (2010)

[53] Lee S.-K., *et al.*, All Graphene-Based Thin Film Transistors on Flexible Plastic Substrates, *Nano Lett.* **12(7)** 3472-3476 (2012)

[54] Dufferwiel S., *et al.*, Exciton-polaritons in van der Waals heterostructures embedded in tunable microcavities, *arXiv*:1505.04438 (2015)

[55] Withers F., *et al.*, Light-emitting diodes by band-structure engineering in van der Waals heterostructures, *Nat. Mat.* **14** 301-306 (2015)

[56] Luxmoore I. J., *et al.*, Control of spontaneous emission from InP single quantum dots in GaInP photonic crystal microcavities, *Appl. Phys. Lett.* **97** 181104 (2010)

[57] Weisbuch C., *et al.*, Observation of the coupled exciton-polariton mode splitting in a semiconductor quantum microcavity, *Phys. Rev. Lett.* **69** 3314 (1992)

[58] Kasprzak J., *et al.*, Bose-Einstein condensation of exciton polaritons, *Nature* **443** 409-414 (2006)

[59] Imamoglu A., *et al.*, Nonequilibrium condensates and lasers without inversion: Exciton-polariton lasers, *Phys. Rev. A* **53** 4250 (1996)

[60] Deng H., *et al.*, Polariton lasing vs. photon lasing in a semiconductor microcavity, *PNAS* **100(26)** 15318-15323 (2003)

[61] Schneider C., *et al.*, An electrically pumped polariton laser, *Nature* **497** 348-352 (2013)

[62] Sich M., *et al.*, Observation of bright polariton solitons in a semiconductor microcavity, *Nat. Phot.* **6** 50-55 (2012)

[63] Amo A., *et al.*, Superfluidity of polaritons in semiconductor microcavities, *Nat. Phys.* **5** 805-810 (2009)

[64] Amo A., *et al.*, Exciton-polariton spin switch, *Nat. Phys.* **4** 361-366 (2010)

[65] Furchi M., *et al.*, Microcavity-Integrated Graphene Photodetector, *Nano Lett.* **12(6)** 2773-2777 (2012)

[66] Wu S., *et al.*, Control of two-dimensional excitonic light emission via photonic crystals, *2D Materials* **1** 011001 (2014)

[67] Wu S., *et al.*, Monolayer semiconductor nanocavity lasers with ultralow threshold, *Nature* **520** 69-72 (2015)

[68] Salehzadeh O., *et al.*, Optically Pumped Two-Dimensional MoS_2 Lasers Operating at Room-Temperature, *Nano Lett.* **15(8)** 5302-5306 (2015)

[69] Ye Y., *et al.*, Monolayer excitonic laser, *arXiv*:1503.06141 (2015)

[70] Liu X., *et al.*, Strong light-matter coupling in two-dimensional atomic crystals, *Nat. Phot.* **9** 30-34 (2015)

[71] Lebégue S., *et al.*, Electronic structure of two-dimensional crystals from ab initio theory, *Phys. Rev. B* **79** 115409 (2009)

[72] Cheiwchanchamnagij T., *et al.*, Quasiparticle band structure calculation of monolayer, bilayer, and bulk MoS_2, *Phys. Rev. B* **85** 205302 (2012)

[73] Arora A., *et al.*, Excitonic resonances in thin films of WSe_2: from monolayer to bulk material, *Nanoscale* **7(23)** 10421-10429 (2015)

[74] Xiao D., *et al.*, Berry phase effects on electronic properties, *Rev. Mod. Phys.* **82** 1959-2007 (2010)

[75] Berry M. V., Quantal Phase Factors Accompanying Adiabatic Changes, *Proc. of the Roy. Soc. A* **392 (1802)** 45-57 (1984)

[76] Resta R., Manifestations of Berry's phase in molecules and in condensed matter, *J. Phys.: Cond. Matter* **12** R107 (2000)

[77] Xu X., *et al.*, Spin and pseudospins in layered transition metal dichalcogenides, *Nat. Phys.* **10** 343-350 (2014)

[78] Yu H., *et al.*, Dirac cones and Dirac saddle points of bright excitons in monolayer transition metal dichalcogenides, *Nat. Phys.* **10** 343-350 (2014)

[79] Wang G., *et al.*, Valley dynamics probed through charged and neutral exciton emission in monolayer WSe_2, *Phys. Rev. B* **90** 075413 (2014)

[80] Jones A. M., *et al.*, Optical generation of excitonic valley coherence in monolayer WSe_2, *Nat. Nano.* **8** 634-638 (2013)

[81] Wang G., *et al.*, Polarization and time-resolved photoluminescence spectroscopy of excitons in $MoSe_2$ monolayers, *Appl. Phys. Lett.* **106** 112101 (2015)

[82] Zhang A., *et al.*, Anomalous valley polarization in monolayer $MoSe_2$, *arXiv*:1503.08631 (2015)

[83] Singh J., Electronic and Optoelectronic Properties of Semiconductor Structures, *Cambridge University Press* (2003)

[84] Cai Y., *et al.*, Lattice vibrational modes and phonon thermal conductivity of monolayer MoS_2, *Phys. Rev. B* **89** 035438 (2014)

[85] Reed M. A., *et al.*, Observation of discrete electronic states in a zero-dimensional semiconductor nanostructure, *Phys. Rev. Lett.* **60** 535-537 (1988)

[86] Michler P., *et al.*, A Quantum Dot Single-Photon Turnstile Device, *Science* **290** 2282 (2000)

[87] Zhou W., *et al.*, Intrinsic Structural Defects in Monolayer Molybdenum Disulfide, *Nano Lett.* **13**(6) 2615-2622 (2013)

[88] Erementchouk M., *et al.*, Optical signatures of states bound to vacancy defects in monolayer MoS_2, *Phys. Rev. B* **92** 121401 (2015)

[89] Komsa H., *et al.*, Native defects in bulk and monolayer MoS_2 from first principles, *Phys. Rev. B* **91** 125304 (2015)

[90] Liu H.-L., *et al.*, Anomalous lattice vibrations of monolayer MoS_2 probed by ultraviolet Raman scattering, *Phys. Chem. Chem. Phys.* **17** 14561 (2015)

[91] Molina-Sanchez A., *et al.*, Phonons in single and few-layer MoS_2 and WS_2, *Phys. Rev. B* **84** 155413 (2011)

[92] Kolesnikov N. N., *et al.*, Influence of growth conditions on microstructure and properties of GaSe crystlas, *J. of Cryst. Growth* **300** 294 (2007)

[93] Mooser E., *et al.*, The Band-Gap Excitons in Gallium Selenide, *Il Nuovo Cimento* **18** 164 (1973)

[94] Zolyomi V., *et al.*, Band Structure and Optical Transitions in Atomic Layers of Hexagonal Gallium Chalcogenides, *Phys. Rev. B* **87** 195403 (2013)

[95] Nahory R. E., *et al.*, Stimulated emission and the type of bandgap in GaSe, *Sol. State Comm.* **9(13)** 1107-1111 (1971)

[96] Hu P., *et al.*, Synthesis of Few-Layer GaSe Nanosheets for High Performance Photodetectors, *ACS Nano* **6** 5988 (2012)

[97] Hopfield J. J., *et al.*, Resonant Scattering of Polaritons as Composite Particles, *Phys. Rev.* **182** 945 (1969)

[98] Savona V., *et al.*, Quantum well excitons in semiconductor microcavities: Unified treatment of weak and strong coupling regimes, *Sol. State Comm.* **92(9)** 733-739 (1995)

[99] Dumcenco D., *et al.*, Large-Area Epitaxial Monolayer MoS_2, *ACS Nano* **9(4)** 4611-4620 (2015)

[100] Zhang Y., *et al.*, Direct observation of the transition from indirect to direct bandgap in atomically thin epitaxial $MoSe_2$, *Nat. Nano.* **9** 111-115 (2014)

[101] Allen M. J., *et al.*, Honeycomb Carbon: A Review of Graphene, *Chem. Rev.* **110** 132-145 (2010)

[102] Suk J. W., *et al.*, Transfer of CVD-grown monolayer graphene onto arbitrary substrates, *ACS Nano* **5(9)** 6916-6925 (2011)

[103] Dean C., *et al.*, Graphene based heterostructures, *Sol. State Comm.* **152** 1275-1282 (2012)

[104] Castellanos-Gomez A., *et al.*, Deterministic transfer of two-dimensional materials by all-dry viscoelastic stamping, *2D Materials* **1** 011002 (2014)

[105] O'Brien M., *et al.*, Transition Metal Dichalcogenide Growth via Close Proximity Precursor Supply, *Sci. Rep.* **4** 7374 (2014)

[106] Van der Zande A. M., *et al.*, Grains and grain boundaries in highly crystalline monolayer molybdenum disulphide, *Nat. Mat.* **12** 554-561 (2013)

[107] Lauritsen J. V., *et al.*, Size-dependent structure of MoS_2 nanocrystals, *Nat. Nano.* **2** 53-58 (2007)

[108] Byskov L. S., *et al.*, Edge termination of MoS_2 and CoMoS catalyst particles, *Cat. Lett.* **64** 95-99 (2000)

[109] Trichet A. A. P., *et al.*, Topographic control of open-access microcavities at the nanometer scale, *Opt. Exp.* **23(13)** 17205-17216 (2015)

[110] Dolan P. R., *et al.*, Femtoliter tunable optical cavity arrays, *Nature Communications* **35** 3556-3558 (2010)

[111] *http://www.phys.keio.ac.jp/guidance/labs/sasada/research/orbangmom-en.html*

[112] Dufferwiel S., *et al.*, Strong exciton-photon coupling in open semiconductor microcavities, *App. Phys. Lett.* **104** 192107 (2014)

[113] Schwarz S., *et al.*, Two-Dimensional Metal-Chalcogenide Films in Tunable Optical Microcavities, *Nano Lett.* **14** 7003-7008 (2014)

[114] Siegman A. E., Lasers, *University Science Books* (1986)

[115] Besga B., *et al.*, Polariton Boxes in a Tunable Fiber Cavity, *Phys. Rev. Appl.* **3** 014008 (2015)

[116] Dufferwiel S., *et al.*, Spin Textures of Polariton Condensates in a Tunable Microcavity with Strong Spin-Orbit Interaction, *arXiv:*1504.02341 (2015)

[117] Albrecht R., *et al.*, Coupling of a Single Nitrogen-Vacancy Center in Diamond to a Fiber-Based Microcavity, *Phys. Rev. Lett.* **110** 243602 (2013)

[118] Johnson S., *et al.*, Tunable cavity coupling of the zero phonon line of a nitrogen-vacancy defect in diamond, *arXiv:*1506.05161 (2015)

[119] Sercombe D., *et al.*, Optical investigation of the natural electron doping in thin MoS_2 films deposited on dielectric substrates, *Sci. Rep.* **3** 3489 (2013)

[120] Capozzi V., *et al.*, Thermalization of photoexcited localized excitons in GaSe samples with stacking disorder, *Phys. Rev. B* **34** 3924 (1986)

[121] Oskooi A. F., *et al.*, Meep: A flexible free-software package for electromagnetic simulations by the FDTD method, *Comp. Phys. Comm.* **181** 687-702 (2010)

[122] Taylor R. A., *et al.*, Time-resolved exciton photoluminescence in GaSe and GaTe, *J. Phys. C* **20** 6175 (1987)

[123] Raymond S., *et al.*, Excited-state radiative lifetimes in self-assembled quantum dots obtained from state-filling spectroscopy, *Phys. Rev. B* **59** 7624 (1999)

[124] Britnell L., *et al.*, Strong Light-Matter Interactions Thin Films, *Science* **340** 1311-1314 (2013)

[125] Rivera P., *et al.*, Observation of long-lived interlayer excitons in monolayer MoSe2–WSe2 heterostructures, *Nature Commun.* **6** 6242 (2015)

[126] Ugeda M. M., *et al.*, Giant bandgap renormalization and excitonic effects in a monolayer transition metal dichalcogenide semiconductor, *Nature Mater.* **13** 1091-1095 (2014)

[127] Bhattacharya P., *et al.*, Room Temperature Electrically Injected Polariton Laser, *Phys. Rev. Lett.* **112** 236802 (2014)

[128] Bhattacharya P., *et al.*, Room temperature polariton lasing vs. photon lasing in a ZnO-based hybrid microcavity, *Opt. Express* **20** 5530-5537 (2012)

[129] Feng L., *et al.*, From Excitonic to Photonic Polariton Condensate in a ZnO-Based Microcavity, *Phys. Rev. Lett.* **110** 196406 (2013)

[130] Kena-Cohen S., *et al.*, Room-temperature polariton lasing in an organic single-crystal microcavity, *Phys. Rev. Lett.* **4** 371-375 (2010)

[131] Daskalakis K. S., *et al.*, Nonlinear interactions in an organic polariton condensate, *Nature Mater.* **13** 271-278 (2014)

[132] Plumhof J. D., *et al.*, Room-temperature Bose-Einstein condensation of cavity exciton-polaritons in a polymer, *Nature Mater.* **13** 247-252 (2014)

[133] Kavokin A. V., Baumberg J. J., Malpuech, G. & Laussy F. P., Microcavities, *Oxford University Press* Series on Semiconductor Science and Technology (2007)

[134] Ivchenko E. L., *et al.*, Optical spectroscopy of semiconductor nanostructures, *Alpha Science International Ltd* (2005)

[135] Nalitov A. V., *et al.*, Spin-Orbit Coupling and the Optical Spin Hall Effect in Photonic Graphene, *Phys. Rev. Lett.* **114** 026803 (2015)

[136] Whittaker D. M., What Determines Inhomogeneous Linewidths in Semiconductor Microcavities?, *Phys. Rev. Lett.* **80** 4791-4794 (1998)

[137] Kavokin A. V., Motional narrowing of inhomogeneously broadened excitons in a semiconductor microcavity: Semiclassical treatment, *Phys. Rev. B* **57** 3757-3760 (1998)

[138] Savona V., et al., Microcavity Polaritons: Homogeneous and Inhomogeneous Broadening in the Strong Coupling Regime, *Physica Status Solidi (a)* **164** 45-51 (1997)

[139] Moody, G. *et al.* Intrinsic Exciton Linewidth in Monolayer Transition Metal Dichalcogenides Intrinsic Exciton Linewidth in Monolayer Transition Metal Dichalcogenides, *arXiv:1410.3143* (2014)

[140] Atanasov R., *et al.*, Exciton properties and optical response in In$_x$Ga$_{1?x}$As/GaAs strained quantum wells, *Physica Status Solidi (a)* **164** 45-51 (1997)

[141] Yu P. Y., *et al.*, Fundamentals of Semiconductors: Physics and Materials Properties, *Spinger* (2005)

[142] Wertz E., *et al.*, Spontaneous formation and optical manipulation of extended polariton condensates, *Nat. Phys.* **6** 860-864 (2010)

[143] André R., *et al.*, Spectroscopy of polaritons in CdTe-based microcavities, *J. of Cryst. Growth* **184** 758-762 (1998)

[144] Kornitzer K., *et al.*, Photoluminescence and reflectance spectroscopy of excitonic transitions in high-quality homoepitaxial GaN films, *Phys. Rev. B* **60** 1471 (1999)

[145] Christmas G., *et al.*, Large vacuum Rabi splitting in a multiple quantum well GaN-based microcavity in the strong-coupling regime, *Phys. Rev. B* **77** 085310 (2008)

[146] Christmas G., *et al.*, Room temperature polariton lasing in a GaN?AlGaN multiple quantum well microcavity, *Appl. Phys. Lett.* **93** 051102 (2008)

[147] Klingshirn C. F., *et al.*, Zinc oxide: from fundamental properties towards novel applications, *Springer* (2010)

[148] Lidzey D. G., *et al.*, Strong exciton-photon coupling in an organic semiconductor microcavity, *Nature* **395** 53-55 (1998)

[149] Berkelbach T. C., *et al.*, Theory of neutral and charged excitons in monolayer transition metal dichalcogenides, *Phys. Rev. B* **88** 045318 (2013)

[150] Savona V., *et al.*, A. Quantum well excitons in semiconductor microcavities: Unified treatment of weak and strong coupling regimes, *Solid State Communications* **93** 733-739 (1995)

[151] Rapaport R., *et al.*, Negatively charged polaritons in a semiconductor microcavity, *Phys. Rev. B* **63** 235310 (2001)

[152] Ross J. S., *et al.* Electrical control of neutral and charged excitons in a monolayer semiconductor, *Nat. Comm.* **4** 1474 (2012)

[153] Stanley R. P., *et al.*, Cavity-polariton photoluminescence in semiconductor microcavities: Experimental evidence, *Phys. Rev. B* **53** 10995 (1996)

[154] Demirchyan S. S., *et al.*, Qubits Based on Polariton Rabi Oscillators, *Phys. Rev. Lett.* **112** 196403 (2014)

[155] Glazov M. M., *et al.*, Exciton fine structure and spin decoherence in monolayers of transition metal dichalcogenides, *Phys. Rev. B* **89** 201302 (2014)

[156] Leyder, C., *et al.*, Observation of the optical spin Hall effect, *Nature Physics* **3** 628-631 (2007)

[157] Sala V. G., *et al.*, Spin-Orbit Coupling for Photons and Polaritons in Microstructures, *Phys. Rev. X* **5** 011034 (2015)

[158] Tercas H., *et al.*, Non-Abelian Gauge Fields in Photonic Cavities and Photonic Superfluids, *Phys. Rev. Lett.* **112** 066402 (2014)

[159] Flatten L. C., *et al.*, Spectral engineering of coupled open-access microcavities, *arXiv:1503.07687* (2014)

[160] Nalitov A. V., *et al.*, Polariton Z Topological Insulator, *Phys. Rev. Lett.* **114** 116401 (2015)

[161] Kretinin A. V., *et al,* Electronic Properties of Graphene Encapsulated with Different Two-Dimensional Atomic Crystals, *Nano Lett.* **14** 3270-3276 (2014)

[162] Pospischil A., *et al.*, Solar-energy conversion and light emission in an atomic monolayer p-n diode, *Nat. Nano.* **9** 257-261 (2014)

[163] Ross J. S., *et al.*, Electrically tunable excitonic light-emitting diodes based on monolayer WSe_2 p-n junctions, *Nat. Nano.* **9** 268-272 (2014)

[164] You Y., *et al.*, Observation of biexcitons in monolayer WSe_2, *Nat. Phys.* **11** 477-481 (2015)

[165] Gammon D., *et al.*, Fine Structure Splitting in the Optical Spectra of Single GaAs Quantum Dots, *Phys. Rev. Lett.* **76** 3005 (1996)

[166] Aivazian G., *et al.*, Magnetic control of valley pseudospin in monolayer WSe_2, *Nat. Phys.* **11** 148-152 (2015)

[167] Srivastava A., *et al.*, Valley Zeeman effect in elementary optical excitations of monolayer WSe_2, *Nat. Phys.* **11** 141-147 (2015)

[168] Empedocles S. A., *et al.*, Quantum-confined stark effect in single CdSe nanocrystallite quantum dots, *Science* **278** 2114-2117 (1997)

[169] Finley J. J., *et al.*, Quantum-confined Stark shifts of charged exciton complexes in quantum dots, *Phys. Rev. B* **70** 201308(R) (2004)

[170] Gutbrod, T. *et al.* Angle dependence of the spontaneous emission from confined optical modes in photonic dots, *Phys. Rev. B* **59** 2223-2229 (1999)

[171] Einstein A., *et al.*, Zur Quantentheorie der Strahlung, *Phys. Z.* 121-128 (1917)

[172] Kopfermann H., *et al.*, Experimental Proof of 'Negative Dispersion', *Phys. Z.* **122** 438-439 (1928)

[173] Maiman T. H., *et al.*, Stimulated optical radiation in ruby, *Nature* **187** 493-494 (1960)

[174] Bose S. N., *et al.*, Plancks law and light quantum hypothesis, *Phys. Z* 26-178 (1924)

[175] Einstein A., *et al.*, Quantum theory of ideal monoatomic gases, *Sitzber. Preuss. Akad. Wiss.* **23(3)** (1925)

[176] Anderson M. H., *et al.*, Observation of bose-einstein condensation in dilute atomic vapor, *Science* **269** 198-201 (1995)

[177] Davis K. B., *et al.*, Bose-einstein condensation in a gas of sodium atoms, *Phys. Rev. Lett.* **75** 3969-3973 (1995)

[178] Lidzey D. G., *et al.*, Room temperature polariton emission from strongly coupled organic semiconductor microcavities, *Phys. Rev. Lett.* **82** 3316 (1999)

[179] Guillet T., *et al.*, Polariton lasing in a hybrid bulk ZnO microcavity, *Phys. Rev. Lett.* **99** 161104 (2011)

[180] Christopoulos S., *et al.*, Room-temperature polariton lasing in semiconductor microcavities, *Phys. Rev. Lett.* **98** 126405 (2007)

[181] Plumhof J. D., *et al.*, Room-temperature Bose-Einstein condensation of cavity excitonÐpolaritons in a polymer, *Nat. Mat.* **13** 247-252 (2014)

[182] Grenier, C. *et al.* Trion-polaritons: How strong coupling to a cavity changes the orbital and spin properties of trions, *arXiv:*1507.02480 (2015)